Local Structure of Molecular Materials via Neutron Total Scattering and Reverse Monte Carlo

Edward O R Beake

A thesis submitted for the degree of Doctor of Philosophy

School of Physics and Astronomy

September, 2015

Statement of originality

I, Edward Beake, confirm that the research included within this thesis is my own work or that where it has been carried out in collaboration with, or supported by others, that this is duly acknowledged below and my contribution indicated. Previously published material is also acknowledged below.

I attest that I have exercised reasonable care to ensure that the work is original, and does not to the best of my knowledge break any UK law, infringe any third party's copyright or other Intellectual Property Right, or contain any confidential material.

I accept that the College has the right to use plagiarism detection software to check the electronic version of the thesis.

I confirm that this thesis has not been previously submitted for the award of a degree by this or any other university.

The copyright of this thesis rests with the author and no quotation from it or information derived from it may be published without the prior written consent of the author.

Signature: EBeake

Date: 01/10/2015

Details of collaboration and publications:

- E. O. R. Beake, M. T. Dove, A. E. Phillips, D. A. Keen, M. G. Tucker, A. L. Goodwin, T. D. Bennett and A. K. Cheetham (2013) Flexibility of zeolitic imidazolate framework structures studied by neutron total scattering and the Reverse Monte Carlo method. *J. Phys.: Condens. Matter*, **25**, 395403

Abstract

In this thesis the results of neutron total scattering experiments on a series of molecular materials are presented. Local fluctuations in a material's structure may not be apparent from Bragg crystallography, but are captured within, and may emerge from refinement against, a pair distribution function. In molecular materials, the pair distribution function is dominated by intense low-r peaks corresponding to intramolecular correlations, making it more difficult to refine the low-intensity high-r features corresponding to intermolecular correlations.

Using reverse Monte Carlo refinement the local structure in three families of molecular materials have been studied. To reduce the problem posed by intramolecular correlations prior chemical knowledge of the molecular structure is incorporated into the refinement using empirical intramolecular potentials. One of the material families consists of three phases of ZIF-4, a metal-organic framework consisting of tetrahedrally coordinated Zn^{2+} ions connected by imidazolate rings. In this material, the molecular motion responsible for the greater flexibility shown by the amorphous phase compared to the two crystalline phases was identified. The other two material families are organic crystals that consist of isolated molecules, the isomeric molecules *para*- and *ortho*-terphenyl and the other adamantane and its carboxylic acid derivative. *Ortho*-terphenyl is a paradigmatic glass-former, with a glass transition temperature of approximately 246 K and a critical cooling rate of less than 0.1 K min^{-1}. An experimentally refined structural model of the glass phase of this material was shown to be in good agreement with the primary structural predictions of glass theory. *Para*-terphenyl, on the other hand, is a crystalline material that undergoes a phase transition at 178 K. The presented results suggest that this phase transition is not as definitively order-disorder as previously suggested but that there is in fact a very flat energy surface between an order-disorder and a displace phase transition. Adamantane and adamantanecarboxylic acid are crystalline materials that undergo order-disorder phase transitions. The refined structural models of both materials are consistent with a previously proposed structure for the high-temperature phases involving a disordered arrangement of molecules in two different orientations.

Acknowledgements

I am indebted to the following people and I wish to thank them:

- My supervisors, Martin Dove and Anthony Phillips, for their help, advice and support on the long and often winding road of a PhD.
- David Keen and Matt Tucker for their assistance in performing all neutron scattering experiments at ISIS and in the use of Gudrun and RMC.
- Andrew Goodwin for his encouragement in getting me to start a PhD.
- All my colleagues and fellow PhD students in the physics department for their support.

Lastly a huge thanks to my whole family who have put up with often incomprehensible mutterings about my work and for the invaluable support and love of my parents.

This work was supported by the Engineering and Physical Sciences Research Council (EPSRC); the Queen Mary, University of London Postgraduate Research Fund (QMPGRF) and utilised Queen Mary's MidPlus computational facilities, supported by QMUL Research-IT and funded by EPSRC grant EP/K000128/1.

Abbreviations

CRN	Continus Random Network
DMF	Dimethylformamide
EXAFS	Extended X-ray Absorption Fine Structure
GSAS	General Structure Analysis System
MD	Molecular Dynamics
NMR	Nuclear Magnetic Resonance
OTP	*Ortho*-terphenyl
PDF	Pair Distribution Function
PTP	*Para*-terphenyl
RMC	Reverse Monte Carlo
SAV	Solvent Accessible Volume
ZIF	Zeolitic Imidazolate Framework

Contents

Chapter 1

Introduction

1.1 Atomic Structure

Many of society's current problems could be alleviated by the easy availability and implementation of materials with specifically desired properties. High-temperature superconductors could revolutionise energy transmission and infrastructure [1–4], materials with novel magnetic properties are changing the electronics industry and gas absorption and storage materials could help solve the world's climate crisis. Although all these novel properties have been observed experimentally, not all have yet been fully understood and shown in a commercially viable material.

These properties must somehow arise from the atomic structure of a material. Therefore, one key problem in the effort to develop commercially viable materials with one of these novel properties is that of fully understanding a material's atomic structure. With the development of the science of crystallography over the past hundred years, it is now possible to solve the atomic structure of complex crystalline materials. That is to say that through traditional crystallographic techniques the temporal and spatial average coordinates of all atoms, and an associated error, can be calculated. However traditional crystallographic techniques and analysis cannot give a comprehensive view of all materials' atomic structure; in addition to only providing average atomic coordinates, such techniques can only be applied to crystalline materials, materials that consist of a periodic arrangement of atoms. It is not always possible to explain these novel properties by analysis of the average atomic structure of a material and many, particularly gas absorption and storage, are shown by amorphous materials; materials that do not have a periodic arrangement of atoms. Therefore it is important to analyse the local, non-average, atomic structure of a material in a way that is equally applicable to both crystalline and amorphous materials.

Through a range of new techniques, such as diffuse scattering, extended X-ray absorption fine structure (EXAFS) and nuclear magnetic resonance (NMR), it has become possible to investigate the local atomic structure of a material through direct experiment. The local structure of a material is the instantaneous position of an atom with respect to its immediate environment, not the time averaged position of an atom with respect to the bulk and global symmetry of the material, as given by traditional crystallographic techniques. Indeed it has become increasingly clear that the local structure of many materials deviates significantly from the average structure and in many cases it is believed that it is these deviations that give rise to some of the important novel properties described above.

In this thesis the structural analysis of a range of both crystalline and amorphous materials will be presented, and the subsequent development in the analysis of diffuse scattering using computational refinement techniques. These studies have been carried out as part of the continuing development of these techniques for the refinement of a material's local atomic structure, particularly with respect to the local fluctuations in the atomic structure of molecular materials.

1.2 Scattering

The science of crystallography is the process of analysing a beam of radiation, either X-rays, neutrons or electrons, after it has been scattered by a sample; a diffraction pattern. For convenience the key scattering equations are outlined below, as presented by M. T. Dove *et al.* [5]. The scattering from an ensemble of atoms (labelled j or k) is given by the squared modulus of the Fourier transform of the set of instantaneous atomic positions, $\mathbf{r}_j$ and $\mathbf{r}_k$, respectively [6]

$$F(\mathbf{Q}) = \frac{1}{N}\sum_j f_j \exp(i\mathbf{Q}\cdot\mathbf{r}_j) \tag{1.1}$$

$$\begin{aligned} S(\mathbf{Q}) &= N\left\langle |F(\mathbf{Q})|^2 \right\rangle \\ &= \frac{1}{N}\sum_{jk} f_j f_k \left\langle \exp(i\mathbf{Q}\cdot(\mathbf{r}_j - \mathbf{r}_k))\right\rangle \end{aligned} \tag{1.2}$$

where f_j and f_k are the scattering factors of the two atoms, N is the total number of atoms and $\mathbf{Q}$ is the scattering vector, the change in the wave vector of the beam of radiation through the scattering process, the angle brackets in equation 1.2 are averages over all instances in time. $S(\mathbf{Q})$ is measured experimentally, and reflects the average of the instantaneous distance between the positions of all atoms. The experimentally measured total scattering function $S(\mathbf{Q})$ can be separated into two parts, the Bragg and diffuse scattering [7].

$$S(\mathbf{Q}) = S_{\text{Bragg}}(\mathbf{Q}) + S_{\text{Diffuse}}(\mathbf{Q}) \tag{1.3}$$

Analysis of the Bragg or diffuse features within a materials diffraction pattern can give information on either its average or local structure respectively.

1.2.1 Bragg Scattering

Traditional crystallographic techniques for structural determination rely on the analysis of the Bragg scattering within a diffraction pattern, such as the peaks in the low-Q region of figure 1.1.

$$S_{\text{Bragg}}(\mathbf{Q}) = N \left\langle |F(\mathbf{Q})| \right\rangle^2 = \frac{1}{N} \left\langle \left| \sum_j f_j \exp(i\mathbf{Q} \cdot \mathbf{r}_j) \right| \right\rangle^2 \tag{1.4}$$

Bragg scattering, $S_{\text{Bragg}}(\mathbf{Q})$ in equation 1.4, gives information about the distribution function of individual atoms. Bragg scattering exists as δ-functions within the total scattering function $S(\mathbf{Q})$ at values of $\mathbf{Q}$ corresponding to reciprocal lattice vectors of the crystal. The physical origin of these δ-functions in a diffraction pattern, and their analysis, is described in detail in many standard texts [8], the salient points relevant to this thesis are given below.

As these δ-functions, called Bragg peaks, only occur for values of $\mathbf{Q}$ that correspond to the reciprocal lattice vectors, they offer a direct reciprocal space view of the periodicity in the atomic structure. They can therefore be analysed to give the atomic positions and other structural parameters of the sample. However any local break from this periodicity, local-scale fluctuations giving rise to local disorder in the atomic structure of a sample, results in scattering that does not correspond to an allowed value of $\mathbf{Q}$ and so do not

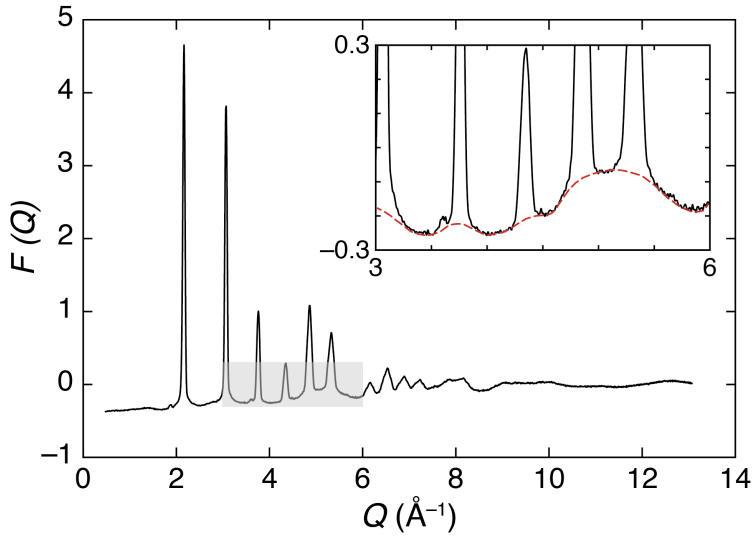

Figure 1.1: Example of a diffraction pattern from AgBr, with Bragg peaks above and background scattering below the red line in the insert, taken from A. L. Goodwin *et al.* [9] with data from D. A. Keen *et al.* [10].

result in Bragg peaks. Therefore from traditional crystallographic techniques an average atomic structure is given.

1.2.2 Diffuse Scattering

Information about these local-scale fluctuations is contained within a material's diffraction pattern, in the diffuse scattering.

$$S_{\text{Diffuse}}(\mathbf{Q}) = N\left\langle |F(\mathbf{Q})|^2 \right\rangle - N\left\langle |F(\mathbf{Q})| \right\rangle^2 \tag{1.5}$$

This diffuse scattering, $\mathrm{S}_{\text{Diffuse}}(\mathbf{Q})$ in equation 1.5, represents the variance in the total scattering function associated with the local fluctuations in the structure and exists as a smooth function for all values of $\mathbf{Q}$. Diffuse scattering is therefore contained within the background of a diffraction pattern, the area below the red line in the insert of figure 1.1. However, not only diffuse scattering is contained in the background of a material's diffraction pattern, it also contains elements from instrument scattering and from the scattering of any sample environment, therefore before any diffuse scattering analysis can take place care must be taken to remove these secondary contributions to the background. The development of techniques for doing this, and the experimental minimisation of these

secondary contributions to the background, has been one of the issues in the development and further use of diffuse scattering. In traditional crystallographic techniques this background is empirically fit and ignored, hence these problems do not arise, but any diffuse scattering is discarded so no local structural information may be obtained.

As information about local fluctuations in a material's atomic structure are contained within its diffuse scattering, through diffuse scattering analysis local structural information can be obtained. The diffuse scattering analysis presented in this thesis investigates the local structure of several materials using the pair distribution function (PDF).

1.2.2.1 Pair Distribution Function

The PDF is a one-dimensional function produced from the analysis of a material's diffuse scattering, averaged over all orientations. It is sensitive to both the short- and long-range structural correlations in a sample, meaning that it can give a structure consistent with all correlations over many length scales. This makes it ideally suited to studying the local structure of disordered solids.

The PDF is calculated by taking the reverse Fourier transform of the total scattering function $S(\mathbf{Q})$, shown in figure 1.2. The exact mathematical definition of the PDF will be given in section 2.2.1 but is not required for this introductory discussion. A PDF is essentially a histogram of interatomic separations, a graph representing the probability of a pair of atoms having that interatomic separation, weighted by the scattering lengths of the atoms involved. The real space relationship of a PDF is shown in figure 1.2, with the low-r peaks corresponding directly to the nearest neighbour interatomic correlations.

The simplest type of local structure analysis that can be done on a PDF is bond length determination. As described above the positions of the peaks in a PDF correspond to the interatomic separations in a compound and so if a peak-fitting procedure is carried out, typically using a Gaussian, the bond lengths can be readily determined. The distances determined from a PDF represent the average distance between a pair of atoms unlike the distances determined from traditional crystallographic analysis that represents the distance between the average positions of a pair of atoms in the unit cell. Sometimes

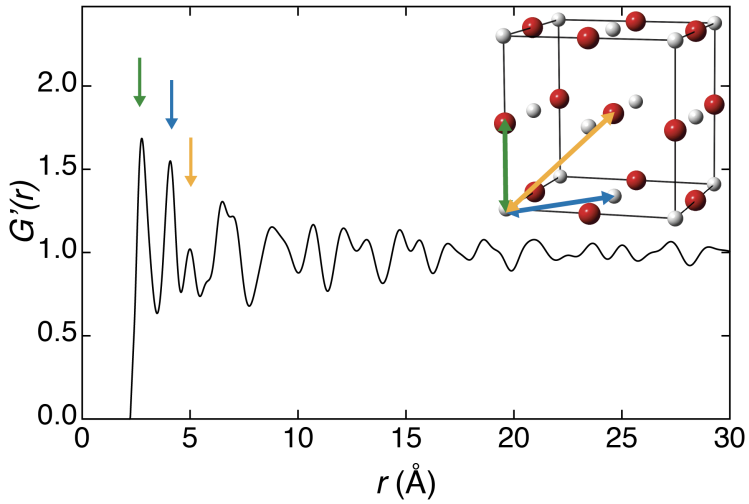

Figure 1.2: Example PDF of AgBr, the atomic correlation's represented by the low-r peaks in the PDF are shown in the insert, taken from A. L. Goodwin *et al.* [9] with data from D. A. Keen *et al.* [10].

these two quantities are not the same,

$$\langle r_1 - r_2 \rangle \neq \langle r_1 \rangle - \langle r_2 \rangle \tag{1.6}$$

where r_1 and r_2 are the positions of two atoms and the angle brackets are spatial averages. This subtle difference can actually have very important ramifications for systems with high levels of local disorder or large amplitude vibrational motion, such as the interpretation of the Si–O bond in silica [11–13].

A peak-fitting procedure also gives two other pieces of information. As the peaks in a PDF represent a weighted probability of an atom at that interatomic separation, so the integral of a peak can give the coordination number. This will typically be the same as the coordination numbers given in the average structure but may be a useful test for materials in which there is compositional disorder as the weighting is related to the atomic scattering power of the relevant atoms. The other piece of information is related to the width of the PDF peaks. The peak width is dictated by the degree of static or dynamic variation in the corresponding bond length and so is related to the vibrational energy of the material [14]. Essentially a small peak width corresponds to a strongly conserved bond length, hence high vibrational frequencies, and a large peak width corresponds to a

weakly conserved bond length, hence low vibrational frequencies.

Due to its unique utility as a function that gives local structural information but that also gives a coherent structure over many length scales, the PDF has been used to study many functional materials over the last decades. A comprehensive overview of these studies is given by A. L. Goodwin *et al.* [9]. The areas in which PDFs are currently being used include research into negative thermal expansion [15, 16], zeolites, metal-organic frameworks [17], spin glasses [18, 19] and nanoparticles [20].

1.3 Computational Refinements

The simple peak-fitting analysis procedure described above can give structural information about the local environment around an atom, as this structural information corresponds directly to an individually defined peak in the low-r region of a PDF. However the material's longer range order, structure on length scales of greater than approximately 5 Å, does not correspond directly to an individually defined peak in the PDF and so can not be analysed by a peak-fitting procedure. Instead a material's longer range order corresponds to the higher-r region of a PDF, which is made up of many overlapping peaks. Therefore, to investigate longer range order a more complicated computational refinement procedure must be followed, this may be done following one of two methods; small- or big-box refinements.

Small-box refinement, as implemented in PDFfit [21, 22], can be thought of as 'real-space Rietveld' refinement. Small-box PDF refinements refine the same parameters as in a standard Rietveld refinement - atomic coordinates, atomic displacement parameters and lattice parameters - within the unit cell of a crystalline material. However as refinements are done against a PDF the refined parameters will reflect the local structure of a material allowing the local fluctuations in the structure of crystalline materials to be studied. For example PDFfit has been used to study the Jahn-Teller distortion across the phase transitions in the perovskite $LaMnO_3$ [23].

However small-box refinements clearly can not be applied to non-crystalline materials nor, using only the unit cell of a material, can it be used to study the arrangement or

orientation of molecules within a crystal. Studies of this nature, therefore, require the use of big-box refinement, as implemented in reverse Monte Carlo (RMC).

1.3.1 Reverse Monte Carlo

RMC is a computational refinement technique that produces an atomistic model of a section of a material [24–26]. It does this by calculating the scattering data of the model and randomly moving the atoms within the model to achieve better agreement between the experimental and calculated scattering data. The decision whether to accept or reject an atomic move is made via the Metropolis algorithm [27].

The model, representing a section of the material under investigation, whose atomic configuration is refined by RMC, is called a supercell. The RMC algorithm starts by moving a random atom in the supercell by a random amount and in a random direction. The scattering data given by the supercell is then calculated and compared to the experimental data. If there is an improvement in the agreement between the experimental and calculated scattering data then the move is accepted unconditionally. If however there is a decrease in agreement then the move is accepted subject to a probability condition. This probability is related to the amount that the move decreases the fit between the calculated and experimental scattering data. A new atomic move is then made and the procedure starts again. This algorithm is summarised in a flow chart, figure 1.3.

The decision as to whether a move decreases or increases the agreement between the calculated and experimental data, and therefore whether it is accepted or not, is made by defining a cost function, χ^2_{RMC}

$$\chi^2_{\mathrm{RMC}} = \chi^2_{i(Q)} + \chi^2_{\mathrm{PDF}} \tag{1.7}$$

where $\chi^2_{i(Q)}$ and χ^2_{PDF} correspond to the agreement between the experimental and calculated data of two diffuse scattering functions, the total scattering function and PDF respectively.

If a proposed move lowers the value of χ^2_{RMC} it is accepted, but if it raises the value of χ^2_{RMC} it is accepted with probability $\exp(-\Delta\chi^2/2)$. This seemingly counterintuitive acceptance of moves that decreases the agreement between the calculated and experi-

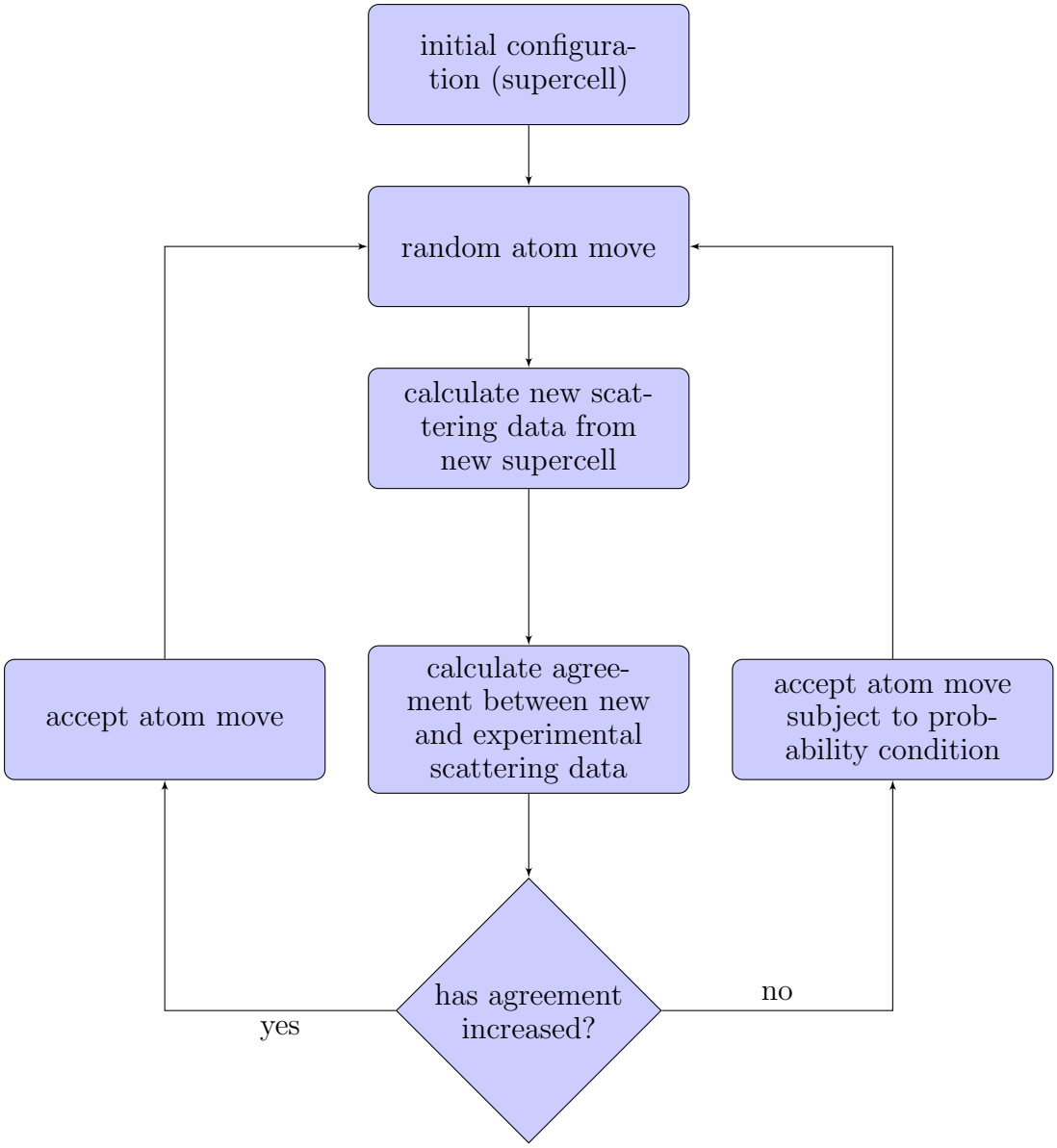

Figure 1.3: Flow chart of the RMC refinement algorithm.

mental total scattering data is done to prevent the algorithm from getting stuck in a local minimum within the energy landscape of the refinement, and never proceeding to the refinements global energy minimum. In RMC χ^2_{RMC} is analogous to the free energy in energy minimisation refinement techniques, such as molecular dynamics (MD), so an RMC refinement actually proceeds along a χ^2_{RMC} landscape. However by using the term energy in this discussion a comparison is more easily drawn between the way in which RMC addresses this issue and how it is addressed by other refinement techniques. A simple one-dimensional graphical representation of an energy landscape with a local and

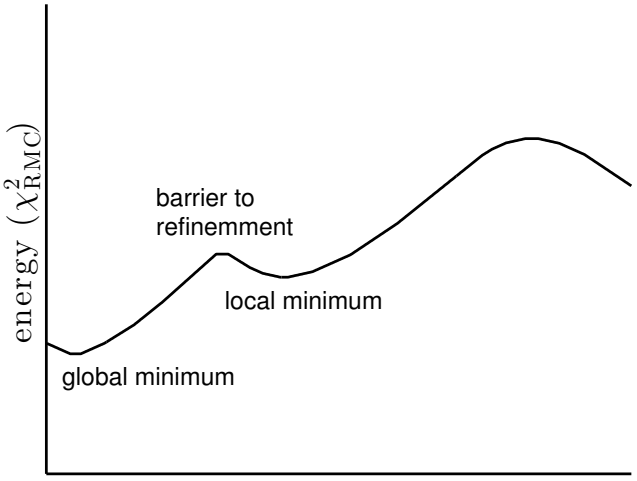

Figure 1.4: A simplified one-dimensional graphical representation of the energy landscape for an energy minimisation refinement, analogous to the χ^2_{RMC} landscape of an RMC refinement. Showing an example local and global minimum separated by a barrier to the refinement, an area of higher energy that the refinement must pass through in order to reach a global minimum.

global minimum within it is given in figure 1.4.

A local minimum is a point in the energy landscape in which the energy of the system will be raised regardless of the direction of travel. For an RMC refinement it is a point where the value of χ^2_{RMC} will be raised regardless of the atomic move made. Therefore, to refine the structure any further requires the algorithm to accept 'bad' moves, increasing the value of χ^2_{RMC}, in order for the structure to get over a 'hump' in the energy landscape or 'barrier to refinement'. Thus allowing the value of χ^2_{RMC} to then further decrease to the global minimum, and for the refinement to therefore achieve an atomic configuration that more closely resembles that suggested by experiment.

After running an RMC refinement for a suitable period of time, typically about a week, allowing several million iterations of the algorithm shown above, such that each atom has on average been moved several thousand times, the configuration of atoms in the supercell will have found the global energy minimum of the energy landscape shown in figure 1.4. This is the area of the energy landscape where the difference between the experimental and calculated data is at a minimum, where the value of χ^2_{RMC} is at a minimum. However this is not a unique point in the energy landscape, rather a region in which an infinite number

of configurations exist all giving an approximate minimum value of χ^2_{RMC}. Therefore there is not a unique 'right' atomic configuration, but a range of atomic configurations that all give an equally valid representation of the material. Whether or not these configurations give an accurate and useful representation of the material under investigation of course depends primarily on the quality of the experimental data available.

1.3.1.1 Initial Configuration

An RMC refinement requires an initial configuration of atoms, from which to start the refinement. This initial configuration may be produced in a number of ways, most typically from a multiplication of the crystallographic unit cell - hence supercell. However, in cases where there is no crystal to start from, such as in the case of a glass or amorphous material, other more innovative solutions must be found. The only requirement of an initial configuration is that it is as close as possible to an accurate representation of the atomic structure of the material under investigation.

An RMC configuration is of course only an infinitesimal section of the material under investigation - typically with dimensions of approximately 50 Å along an edge, containing only several thousand atoms - and has hard unphysical boundaries at its edges. An RMC refinement attempts to refine and thereby reveal the local structure in the bulk of a material. These hard unphysical boundaries mean that the atomic structure at the boundary of an RMC configuration may be very different from that in the bulk, therefore this small RMC configuration must be made to effectively have no boundaries. To do this periodic boundary conditions are applied by RMC, meaning that if an atomic move proposed by RMC would move an atom beyond the boundary, that atom reappears on the opposite site of the configuration. For example if, in a 50 Å cubed initial configuration, there is an atom with an x coordinate of 49.95 Å and an RMC move of 0.1 Å in the x direction is accepted then the new x coordinate of the atom would be 0.05 Å.

The exact details of each initial configuration used in the refinements presented in this thesis are given in their respective chapters.

1.4 Molecular Materials

In this thesis three distinct types of materials are studied, zeolitic imidazolate framework 4 (ZIF-4), two isomers of terphenyl as well as adamantane and its carboxylic acid derivative. The individual structures and specific points of scientific interest for each material will be described in detail in their respective chapters. However, at this point it is worth discussing the common elements within these materials that lead to their selection for study in this thesis. These three materials all contain a large molecular organic component, indeed terphenyl and adamantane are made up entirely of organic molecules while 89% of atoms in ZIF-4 are involved in an organic molecule.

The structure of these organic motifs, planar rings in ZIF-4 and terphenyl and a cluster in adamantane and adamantanecarboxylic acid, are all well understood and give rise to many intramolecular correlations as shown in figure 1.5(a), using ZIF-4 as an example. These intramolecular correlations give rise to many intense peaks that dominate the low-r region of a materials PDF as shown in figure 1.6, using ZIF-4 as an example. However the structures of these organic motifs are well known and understood, so these dominant low-r peaks can be understood and so are of no scientific interest in a PDF study. What is of scientific interest is the intermolecular correlations, the correlations between the molecules within the material as shown in figure 1.5(b), using ZIF-4 as an example. These intermolecular correlations give rise to many weaker overlapping peaks in the high-r region of a materials PDF as shown in figure 1.6, using ZIF-4 as an example. It is the difficulty of properly refining these intermolecular correlations via RMC in the presence of large intramolecular correlations within a molecular motif that is the principal issue investigated in this thesis.

This problem of overlapping intermolecular peaks and the domination of the PDF by intense low-r intramolecular peaks reduces the potential information that may be provided by an RMC refinement with regard to the intermolecular correlations. If this problem, caused by the well understood intramolecular correlations, could be reduced then the PDF would be better able to guide the RMC refinement with regard to the interesting intermolecular correlations, so hopefully producing a more useful refinement.

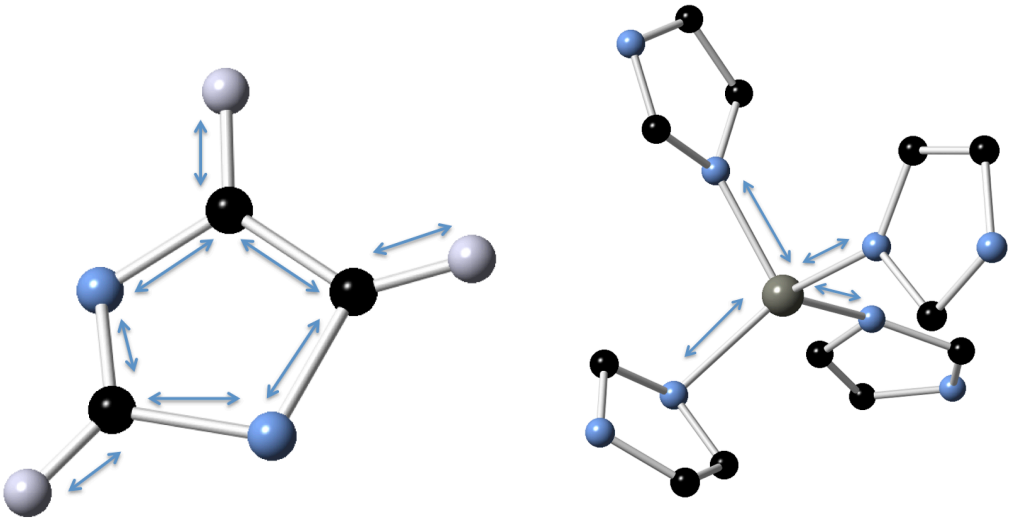

(a) (b)

Figure 1.5: The inter- and intramolecular correlations within ZIF-4, (a) Intramolecular correlations (b) Intermolecular correlations, H: light grey; C: black; N: blue; Zn: dark grey; inter/intramolecular correlations: blue arrows.

To this end the intramolecular correlations within the molecular motifs in these materials are restrained using molecular potentials. Molecular potentials cause an increase in χ^2_{RMC} if an atomic move proposed by RMC would cause a move away from the known value of a property controlled by a well understood peak in a materials PDF, making such a move less lightly. Molecular potentials have been previously implemented in RMC and are further developed in this thesis.

1.5 Structure of this Thesis

In this thesis the local structure of five molecular materials will be studied. The experimental techniques used in the course of these local structural studies are introduced in chapter 2. This covers the basic theory and important experimental considerations of neutron total scattering, the technique that was used for the majority of the experimental work in this thesis. Chapter 2 also outlines the methodology followed in these studies, giving details on the extraction and production of the total scattering functions used as well as more fully detailing the computational refinement technique used and the

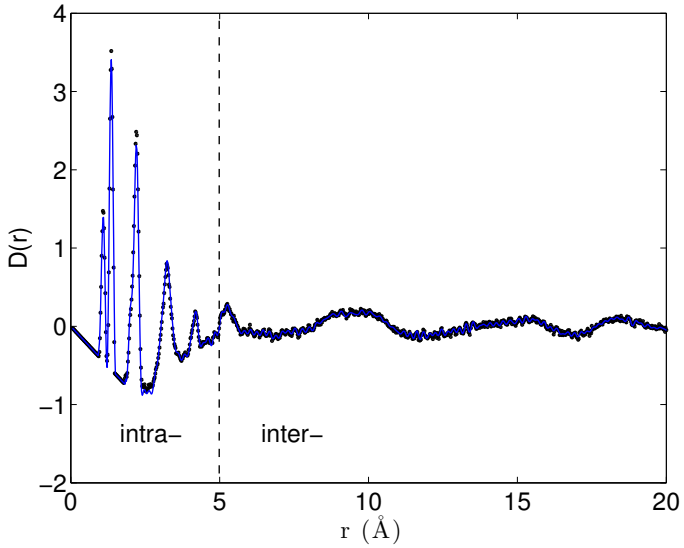

Figure 1.6: The PDF of ZIF-4 showing the presence of intense intramolecular peaks dominating the low-r region of the PDF (to the left of the dashed line) and weaker overlapping intermolecular peaks in the high-r region of the PDF (to the right of the dashed line).

modifications made to it by the author.

Chapters 3-7 each discuss one of the five materials studied, investigating the local structural fluctuations and how they may influence or account for the phase transitions and flexibilities seen in the materials. Finally, in chapter 8, some conclusions on the utility of the refinement method described, as applied to molecular materials, are given, as well as some suggestions of possible areas of further research.

Chapter 2

Methodology

2.1 Outline

This chapter outlines the methodology and techniques applied to the materials studied in the subsequent chapters. The methodology has four principal steps;

Experiment

Perform the total scattering experiment producing raw scattering data.

Data Processing

Process the raw scattering data, using Gudrun to produce the total scattering functions, $i(Q)$ and $D(r)$, and GSAS to extract the Bragg profile and lattice parameters, for use in the refinement process.

Reverse Monte Carlo

Initialise and carry out reverse Monte Carlo refinements driven by the experimental total scattering data produced.

Analysis

Analyse the structural models produced by the refinement process.

2.2 Experiment

Diffraction is a long-known and well-studied method for structural determination, and in this thesis it is used to study the structure of all the presented materials. The diffraction in this thesis uses total scattering, which can be carried out with either neutrons or X-rays.

For the total scattering in this thesis neutrons, rather than X-rays, were used. This is, in part, due to the particular elements in the materials under investigation. X-rays are scattered by interacting with electrons, consequently the strength with which X-

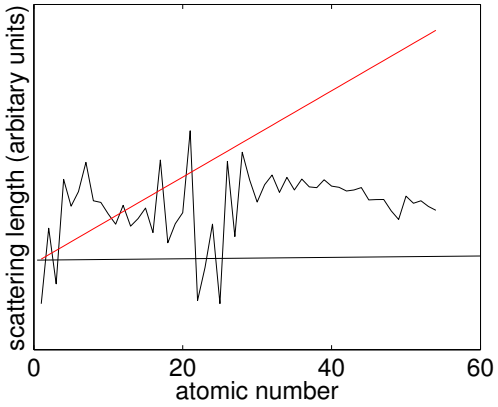

Figure 2.1: Variation in the relative neutron and X-ray scattering lengths of atoms with increasing atomic number [7, 28]. X-ray; red, neutron; black.

rays are scattered by an atom is proportional to the number of electrons around that atom. Neutrons, however, do not have this proportionality as neutrons are scattered by the nucleus of an atom, not the electrons. This difference in the scattering mechanism of neutrons and X-rays results in the emphasis of different structural features in total scattering data produced by neutrons and that produced by X-rays. Therefore, although not done in this thesis, X-ray total scattering can provide useful information when used in conjunction with neutron total scattering. The variation in the relative neutron and X-ray scattering lengths of atoms with increasing atomic number is shown in figure 2.1. A negative neutron scattering length indicates an atom that inverts the phase of the neutron wave in the scattering process.

For example the first material studied in this thesis is ZIF-4 and it contains zinc with 30 electrons, nitrogen with seven electrons, carbon with six electrons, and hydrogen with one electron. Carbon and nitrogen, having very similar numbers of electrons, have very similar X-ray scattering powers and so would be very difficult to distinguish between using X-ray total scattering, hence the use of neutron total scattering. Hydrogen, having only one electron, has a very low X-ray scattering power and so it is very difficult to determine the atomic coordinates of hydrogens using X-ray total scattering, hence the use of neutron total scattering.

The second reason for using neutron total scattering rather than X-ray total scattering is the requirement to have scattering data measured out to a large scattering vector (high-

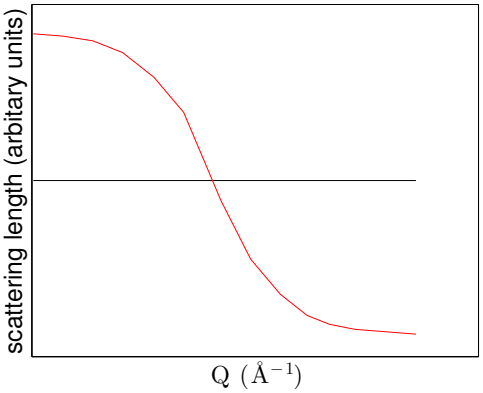

Figure 2.2: Variation in the relative neutron and X-ray scattering lengths of atoms with increasing **Q**. Low-energy X-rays; red, neutrons; black.

Q) to produce an accurate PDF [13]. X-ray atomic scattering factors exhibits a dramatic drop off as the scattering vector increases due to the comparable size of the wavelength of X-rays and the size of what X-rays interact with, the electron cloud around an atom, resulting in not being able to measure the high-**Q** data required to produce a PDF. Recently however, through the use of very high-energy, shorter wavelength, X-rays from a synchrotron source or an advanced silver source X-ray diffractometer, high-**Q** X-ray total scattering data may be produced. Additionally high-energy X-rays do not suffer from the same absorption as low-energy X-rays and so the need for large absorption corrections to the total scattering data is reduced. Neutrons do not have this drop off problem as there are several orders of magnitude difference between the wavelength of a neutron and the size of what it interacts with, the nucleus of an atom. Neutron scattering lengths are therefore independent of **Q**. The variation in the relative neutron and X-ray scattering lengths of atoms with increasing **Q** is shown in figure 2.2.

There are two main types of neutron scattering processes, coherent and incoherent scattering. The coherent scattering cross section is obtained by averaging over nuclear isotopes and spin states whereas the incoherent scattering cross section accounts for the differences in scattering from the same atom type due to differences in isotope or spin state. For most atoms the coherent scattering cross section is larger than the incoherent scattering cross section and so scattering is dominated by the coherent scattering process [28], which is essential for structural studies [7]. Indeed, it is often assumed that the

neutron scattering length for any element is a constant, coherent, scattering length across all atoms in the sample. Many nuclei have a spin of zero, so the spin-dependent contribution to the nuclei-neutron interaction is absent, and even when they are present they are often weak. Moreover, in many important elements, only one isotope exists in significant natural abundance, justifying the constant, coherent, assumption for many elements.

However, there are important exceptions to this, and relevant to this thesis as it occurs in all the studied materials, is that of hydrogen. In hydrogen the spin-dependance of the nucleus-neutron interaction is very important and the ^{1}H isotope has a natural abundance of more than 99.9%. The hydrogen nucleus, an isolated proton, has a spin state of 1/2 which, under the laws of quantum mechanics, can align in four ways with a neutron, also spin state 1/2. Hence there is a large incoherent scattering contribution to the scattering from hydrogen. Deuterium, however, has a zero incoherent scattering cross section and so the problems associated with the scattering from hydrogen can be eliminated if the hydrogen atoms are replaced by deuterium.

2.2.1 Neutron Total Scattering Theory

Different research communities use many different formalisms of total scattering to describe essentially equivalent functions [33], leading to many possible causes of confusion within the total scattering community. Therefore the formalisms followed and functions used in this thesis are described below [7, 13, 34].

$S(\mathbf{Q})$ is the function that is measured experimentally in a neutron powder diffraction experiment, after correction for various experimental factors, described in section 2.3.1, it is defined as

$$S(\mathbf{Q}) = \frac{1}{N} \left\langle \sum_{jk} b_j b_k \exp(i\mathbf{Q} \cdot \mathbf{r}_{jk}) \right\rangle \tag{2.1}$$

where N is the number of atoms, b is the coherent neutron scattering length, and the subscripts j and k denote specific atoms whose instantaneous separation is given as $\mathbf{r}_{jk}$, shown for the general case in section 1.2. The angle brackets denote averages over all orientations of the sample with respect to $\mathbf{Q}$, as obtained in a powder diffraction measurement, and

over all time

$$\langle \exp(i\mathbf{Q}\cdot\mathbf{r}_{jk})\rangle = \frac{1}{4\pi}\int_0^{2\pi} \mathrm{d}\phi \int_0^{\pi} \exp(iQr_{jk}\cos\theta)\sin\theta \mathrm{d}\theta \tag{2.2}$$

where Q is the scattering vector, equal to $|\mathbf{Q}|$, and θ and ϕ are angles in spherical coordinates such that θ is the polar angle between Q and r_{jk}, and ϕ is the azimuthal angle. The first integral over ϕ is trivial, giving us a factor of 2π which cancels with the spherical volume factor of $1/4\pi$ and using the substitution $x = \cos\theta$ so that $-\sin\theta \mathrm{d}\theta = \mathrm{d}x$ to evaluate the second integral, gives

$$\langle \exp(i\mathbf{Q}\cdot\mathbf{r}_{jk})\rangle = \frac{1}{2}\int_{-1}^{+1} \exp(iQr_{jk}x)\mathrm{d}x = \frac{\sin(Qr_{jk})}{Qr_{jk}} \tag{2.3}$$

Hence the total scattering function can be rewritten as

$$S(Q) = \frac{1}{N}\sum_{jk} b_j b_k \frac{\sin(Qr_{jk})}{Qr_{jk}} \tag{2.4}$$

The total scattering function $S(Q)$, equation 2.4, contains "self-scattering" terms where the atoms involved are the same, i.e. $j = k$, such that

$$S(Q) = \frac{1}{N}\sum_{j} b_j^2 + \frac{1}{N}\sum_{j\neq k} b_j b_k \frac{\sin(Qr_{jk})}{Qr_{jk}} \tag{2.5}$$

Defining c_m as the concentration of atoms of type m such that $c_m N$ is the number of atoms of type m, the first term reduces to $\sum_m c_m b_m^2$. The second term is a double sum over all atoms. The first of these can be replaced by a sum over atom types, since we are considering the average behaviour associated with each atom type. The second sum is the sum over all neighbours, which can be replaced by scanning distances between atoms and using the probability of finding the next atom. We write this probability in terms of a function $g_{m,n}(r)$. If the overall density of atoms of type n is $c_n\rho$, where ρ is the overall number of atoms per volume, we can write the number of atoms of type n lying within a spherical shell of thickness $\mathrm{d}r$ at a distance r from an atom of type m as

$4\pi r^2 \mathrm{d}r \times c_n \times g_{m,n}(r)$. Therefore the double sum can be replaced by

$$\frac{1}{N}\sum_{j,k} b_j b_k \frac{\sin(Qr_{jk})}{Qr_{jk}} = 4\pi\rho \int \sum_{m,n} c_m c_n b_m b_n r^2 g_{m,n}(r) \frac{\sin(Qr)}{Qr} \mathrm{d}r \tag{2.6}$$

In the limit that $r \to \infty$, $g_{m,n}(r) \to 1$, reflecting the fact that a shell of large radius will contain a more uniform sample of atoms. This does no more than add a constant at this limit and in a Fourier transform this gives a delta function at $Q = 0$, therefore it would be best to subtract this

$$S_0 = 4\pi\rho \int \sum_{m,n} c_m c_n b_m b_n r^2 \frac{\sin(Qr)}{Qr} \mathrm{d}r \tag{2.7}$$

$i(Q)$, the total scattering function used in RMC is given by subtracting the "self-scattering" term and S_0 from $S(Q)$

$$\begin{aligned} i(Q) &= S(Q) - \sum_m c_m b_m^2 - S_0 & (2.8)\\ &= 4\pi\rho \int \sum_{m,n} c_m c_n b_m b_n r^2 (g_{m,n}(r) - 1) \frac{\sin(Qr)}{Qr} \mathrm{d}r & (2.9) \end{aligned}$$

This total scattering function is then transformed to a real space PDF via a Fourier transform. In this thesis the function $D(r)$ is used, it is defined as

$$D(r) = 4\pi\rho r \sum_{m,n} c_m c_n b_m b_n \left(g_{m,n}(r) - 1\right) \tag{2.10}$$

This function is obtained from the total scattering function $i(Q)$, and *vice versa*, via two transformation equations, as can be seen by a combination and rearrangement of equation 2.10 and 2.9:

$$D(r) = \int_0^\infty Q i(Q) \sin(Qr) \mathrm{d}Q \tag{2.11}$$

$$Qi(Q) = \int_0^\infty D(r) \sin(Qr) \mathrm{d}r \tag{2.12}$$

The third data type extracted from a total scattering experiment is the three-dimensional Bragg structure factor:

$$F_{hk\ell}(\mathbf{Q}_{hk\ell}) = \frac{1}{N_{\text{cell}}} \left\langle \sum_j b_j \exp(i\mathbf{Q}_{hk\ell} \cdot \mathbf{r}_j) \right\rangle \tag{2.13}$$

where $hk\ell$ are the Miller indices, and $\mathbf{Q}_{hk\ell}$ is the corresponding reciprocal lattice vector. The angle brackets denote an average over time, and the sum represents an average over the N_{cell} unit cells.

The Bragg profile function is defined as

$$I(t) = \sum_{hk\ell} |F_{hk\ell}(\mathbf{Q}_{hk\ell})|^2 M_{hk\ell} L_{hk\ell} R_{hk\ell}(t) \tag{2.14}$$

where t is the time taken for neutrons scattered into reciprocal lattice vector $\mathbf{Q}_{hk\ell}$ to travel from the source to the detector, the time-of-flight. Note that in a spallation neutron source, t is proportional to the plane spacing $d_{hk\ell} = 2\pi/Q_{hk\ell}$, where $Q_{hk\ell} = |\mathbf{Q}_{hk\ell}|$. $M_{hk\ell}$ is the multiplicity of a Bragg reflection of type $hk\ell$, $L_{hk\ell}$ is the Lorentz geometric factor, and $R_{hk\ell}(t)$ is the experimental resolution function for the reflection $hk\ell$ and is a function of t. Experimentally the detailed resolution function is determined by a prior Rietveld refinement, as also is the scale factor s, the lattice parameters that determine the value of $Q_{hk\ell}$ and the background function.

2.2.2 Neutron Sources

There are two types of neutron source available for neutron scattering experiments, reactor and spallation sources. The first neutron experiments were conducted using a reactor source, indeed it was only shortly after the first nuclear reactors that research reactors were constructed for this purpose. A reactor source produces a high-flux of neutrons at a steady rate through nuclear fission of Uranium-235. More neutrons than are needed to maintain the chain reaction are produced so there are excess neutrons that can then be used for the scattering experiments.

$$^{235}\text{U} + \text{n} \rightarrow 2.5\text{n} + 200\text{MeV} + \text{nuclei} \tag{2.15}$$

The other, more modern and environmentally neutral, method of producing neutrons is spallation. In this method neutrons are produced by the collision and interaction of a high-energy proton with a heavy metal target. The proton interacts with the nuclei in the heavy metal target; it binds briefly to the nuclei and is then ejected to bind to another nucleus in a cascade reaction. After the proton is ejected the nucleus is left in a high-energy state and to return to its ground state it undergoes neutron evaporation, where neutrons leave the nucleus. Each proton produces 20–40 neutrons [8].

Many different methods of spallation are used, both in terms of the method of producing high-energy protons and the heavy metal target used. All the experiments described in this thesis were conducted at the ISIS facility at the Rutherford-Appleton Laboratory in Oxfordshire. At ISIS an ion source produces H^- ions that are accelerated in a 70 MeV linear accelerator to 37% of the speed of light ($0.37c$). These ions then pass through a thin aluminium foil where they are stripped of their two electrons, leaving a proton. These protons are then directed into a 800 MeV synchrotron, a ring of powerful magnets 163 m in circumference, where they are accelerated to $0.84c$ after 10000 revolutions. 50 Hz pulses of these high-energy protons are then fired at a tungsten target, about the size of a house brick, where the spallation cascade reaction takes place producing neutrons that are then directed towards the instruments [29]. The layout of ISIS and the path followed by the high-energy particles involved in the spallation and neutron scattering process, from H^- ions to neutrons, are shown in figure 2.3.

Neutrons from all sources, both reactor and spallation, tend to have energies that are much too high for use in scattering experiments and so a reduction in neutron energy is required. To achieve this a moderator is used, a material that is maintained at a constant temperature allowing the neutrons to reach thermal equilibrium as they pass through it. A moderator is typically maintained at room temperature, about 300 K. However, depending on the experiment being performed, access to higher wavelength neutrons may be required and so a cold moderator can be used or if access to shorter wavelength neutrons is required a hot moderator can be used.

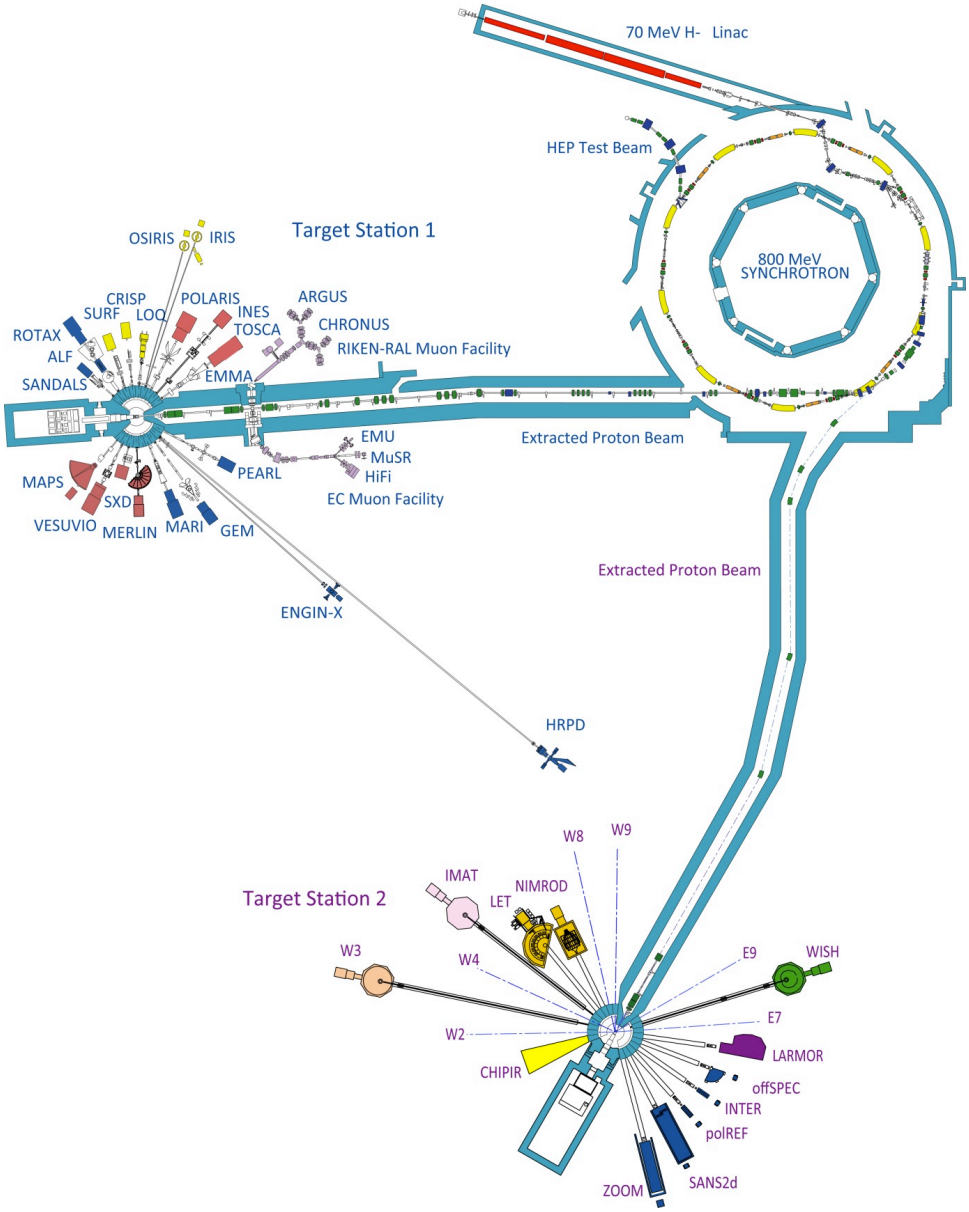

Figure 2.3: Schematic of the ISIS neutron spallation facility [29].

2.2.3 Neutron Scattering Instruments and Experiments

Two neutron scattering instruments were used in the studies presented in this thesis, GEM and POLARIS. Both of these are time-of-flight neutron diffractometers. This means that the diffraction pattern of a sample is measured by recording the time it takes the neutrons to arrive at the detectors, as well as the angle of diffraction, after they have been produced by the spallation source, their time-of-flight. At a spallation source neutrons with a range of wavelengths (and therefore energies) are produced in a single pulse and then travel to

the sample, where they are diffracted according to Bragg's law.

$$\lambda = 2d_{hkl} \sin\theta \tag{2.16}$$

where λ is the neutron wavelength, d_{hkl} is the spacing between planes of diffracting atoms (d-spacing) and 2θ is the scattering angle.

The wavelength of the neutrons can be obtained by measuring their time-of-flight and applying the de Broglie relationship given in equation 2.17. This is due to the fact that the higher energy, shorter wavelength, neutrons are faster and so will have a shorter time-of-flight than the lower energy, longer wavelength, neutrons.

$$\frac{h}{\lambda} = \frac{m_n L}{t} \tag{2.17}$$

where h is Planck's constant, m_n is the mass of a neutron, L is the total flight path and t is the time-of-flight.

Combining and rearranging equations 2.16 and 2.17 yields a relation between the time-of-flight and the d-spacing.

$$t = KLd \sin\theta \tag{2.18}$$

where $K = 505.56$ ms m^{-1} Å^{-1}.

GEM

The general materials powder diffractometer (GEM), figure 2.4, is located at target station one of the ISIS neutron spallation facility. It has an incident path length of 17 m with a scattered path length of 1–2.9 m to detectors covering a scattering angle of 1.1° - 169.3° and uses a room temperature methane moderator [31].

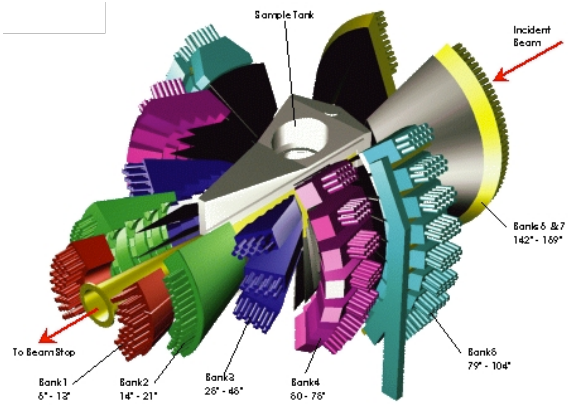

Figure 2.4: Schematic of GEM [31].

POLARIS

The POLARIS diffractometer, figure 2.5, is located at target station one of the ISIS neutron spallation facility. It has an incident path length of 14 m with a scattered path length of 0.6 - 2.65 m to detectors covering a scattering angle of 13° - 160° and uses a room temperature water moderator [32].

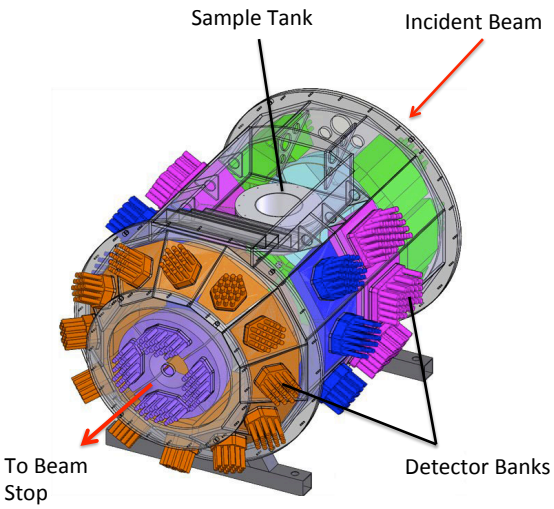

Figure 2.5: Schematic of POLARIS [32].

Both of these instruments collect data from a number of banks of detectors set at different scattering angles and thereby provides coverage to a wide range of the scattering

vector Q up to a value of 50 Å^{-1}. This large range of Q makes GEM and POLARIS both ideally suited to PDF studies, hence their use in all the presented studies.

In all cases, apart from ZIF-4 whose synthesis is detailed in section 3.2, the materials studied are commercially available in perdeuterated form, from which a powder was produced. This powdered sample was contained within a thin-walled vanadium can of diameter 8 mm, which was held in a static He exchange gas cryostat for low-temperature measurements or a low-temperature furnace for above room temperature measurements, if required. Measurements were also performed on the backgrounds from the empty instrument and the empty can within the cryostat and furnace, if applicable, and of a vanadium rod for normalisation.

2.3 Data Processing

2.3.1 Gudrun

Gudrun was written and is developed by Alan Soper [35] at the ISIS neutron facility. It is a program for the conversion of raw neutron or X-ray total scattering data to the differential cross section and hence the total scattering function, $i(Q)$. The total scattering function, $i(Q)$, is then transformed to form the PDF (the transformation equations for this are shown in section 2.2.1). The main problem in this procedure is to minimise effects due to the use of a finite range of Q and noise in the $i(Q)$ data that is particularly prevalent at higher values of Q which result in the generation of ripples in the PDF. Therefore care is taken in the choice of parameters within Gudrun (for example, maximum Q values and settings on noise filtering functions) to minimise the size of spurious effects through the Fourier transform, but inevitably some degree of noise (including higher-frequency oscillations in the data) is generated.

The workflow followed by GudrunN, Gudrun for neutrons, is summarised in a flow chart, figure 2.6, with the key parameters expanded upon below. The values of these key parameters, as used in the processing of each material's total scattering data, is given in their respective chapters.

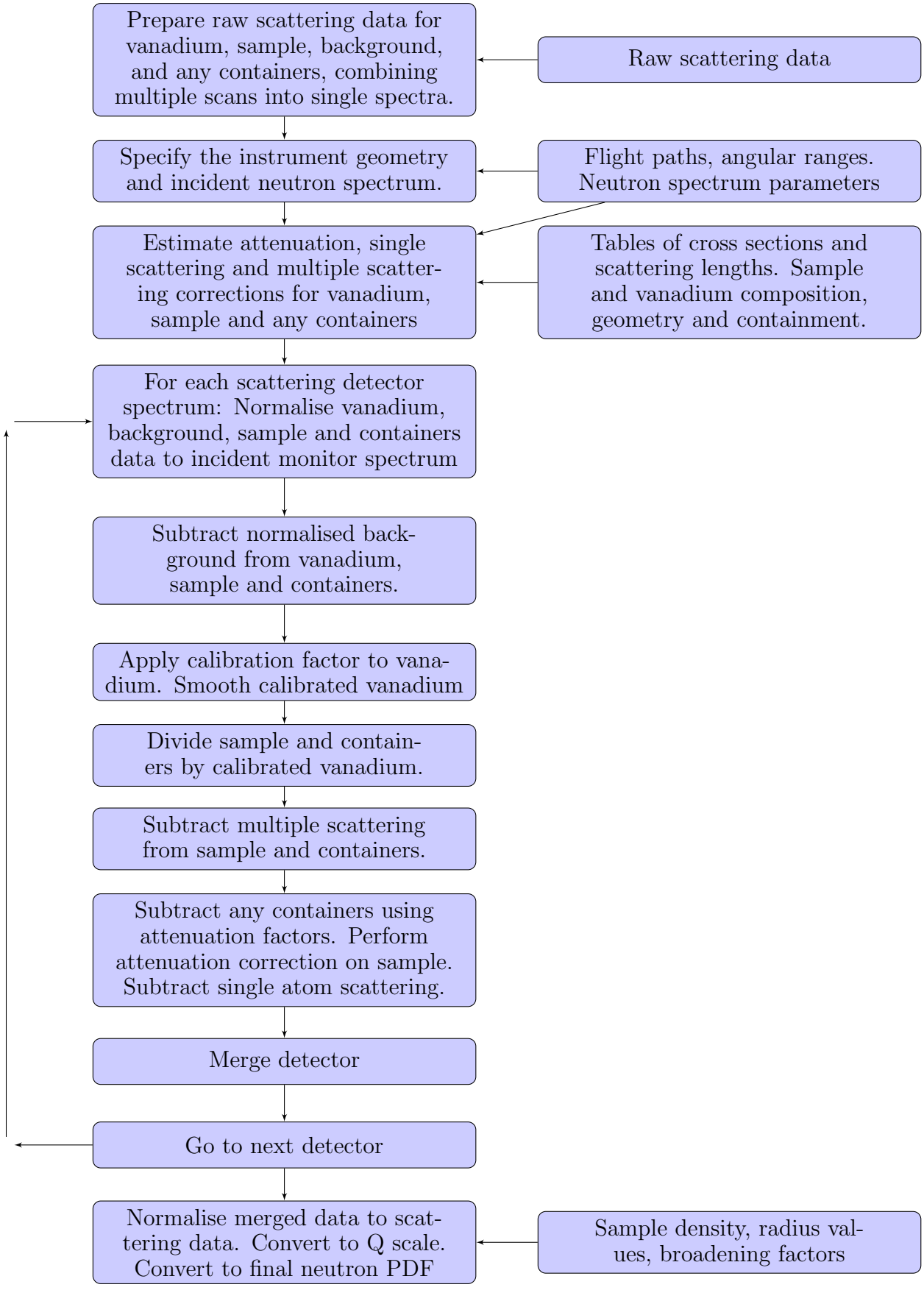

Figure 2.6: Flow chart of the workflow followed by GudrunN, adapted from the Gudrun manual [35].

Tweak factor

A powder sample will never be 'fully' packed in the sample container; a powder sample can not be packed so as there are no voids, the ratio of sample to voids is given by the packing fraction. Calculation of the attenuation and multiple scattering factors require the sample density and so are affected by this packing fraction. Therefore it is specified by the user in the form of the 'tweak factor', which is the inverse of the packing fraction.

In practice the sample's packing fraction is not measured exactly, though it is estimated by a consideration of the sample's mass and 'as packed' volume combined with the 'given' density. Hence the tweak factor is used as an adjustment factor in Gudrun and varies in a non-uniform manner according to experimental errors.

Top Hat function

The method for the production of a PDF from the total scattering function, $i(Q)$, followed by GudrunN is that of the top hat convolution method described by A. K. Soper [36]. This assumes that due to the fact that the data extraction process may not have proceeded perfectly, the total scattering function, $i(Q)$, is on some form of Q dependent background. This background needs to be removed prior to Fourier transform; it is estimated by convolution of the data with the top hat function, $T(\mathbf{Q})$

$$i'(Q) = \int i(|\mathbf{Q} - \mathbf{Q}'|)T(\mathbf{Q}')\mathrm{d}\mathbf{Q}' \tag{2.19}$$

where the integral is over all of reciprocal space for which there is data and the top hat function, $T(\mathbf{Q})$, is given by

$$T(\mathbf{Q}) = \begin{cases} \frac{3}{4\pi Q_{\mathrm{T}}^3} & |\mathbf{Q}| \leq Q_{\mathrm{T}} \\ 0 & |\mathbf{Q}| > Q_{\mathrm{T}} \end{cases} \tag{2.20}$$

The effect of the convolution in equation 2.19 is therefore to 'smear' $i(Q)$ equally by an amount that increases with Q_{T}. Hence, Gudrun takes the Fourier transform of the difference between $i(Q)$ and the background $i'(Q)$ such that the contributions to the total scattering function from self scattering and other sources are removed

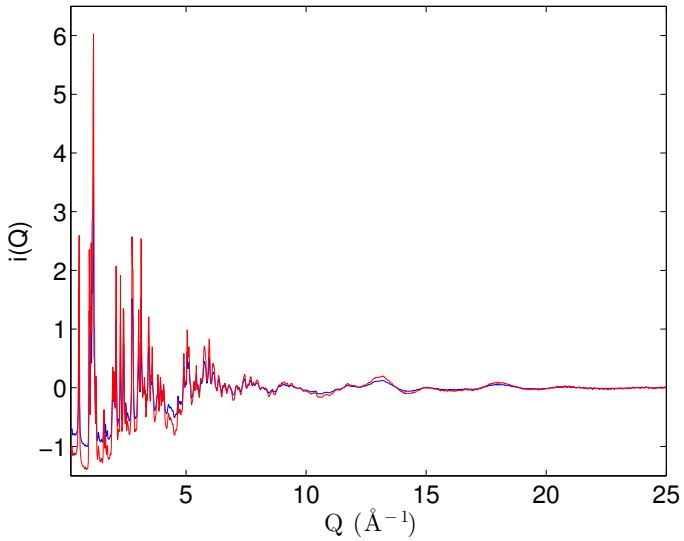

Figure 2.7: Examples of the total scattering data, $i(Q)$, in adamantanecarboxylic acid processed using different values of the top hat function. Blue: $Q_{\mathrm{T}} = 3$ Å^{-1}; red: $Q_{\mathrm{T}} = 5$ Å^{-1}.

prior to Fourier transform. The effect different values of the top hat function have on the total scattering data, $i(Q)$, is shown in figure 2.7.

Maximum Q

The Fourier transform used to obtain a material's PDF, $D(r)$, from its total scattering function, $i(Q)$, is performed over a range of Q. In equation 2.11 this range is 0 to ∞ but in reality the range is Q_{min} to Q_{max}. The greater this range, the larger Q_{max}, the greater the range of the materials total scattering function that is used in the production of its PDF, and so, theoretically, the more accurate the PDF obtained, as shown in figure 2.8. However, at larger values of Q there is a higher degree of 'noise' in the data so, as shown in figure 2.8, a Fourier transform performed using a larger Q_{max} results in a greater degree of ripples in the obtained PDF. Therefore the value of Q_{max} specified by the user must be an intermediate value that gives all the required detail while minimising the production of high-frequency ripples in the resulting PDF.

The use of a finite range of Q results in termination ripples in the obtained PDF, due to the truncation of a theoretically infinite data set. As the experimentally measured $i(Q)$ will always have a finite range these termination ripples are unavoidable. To

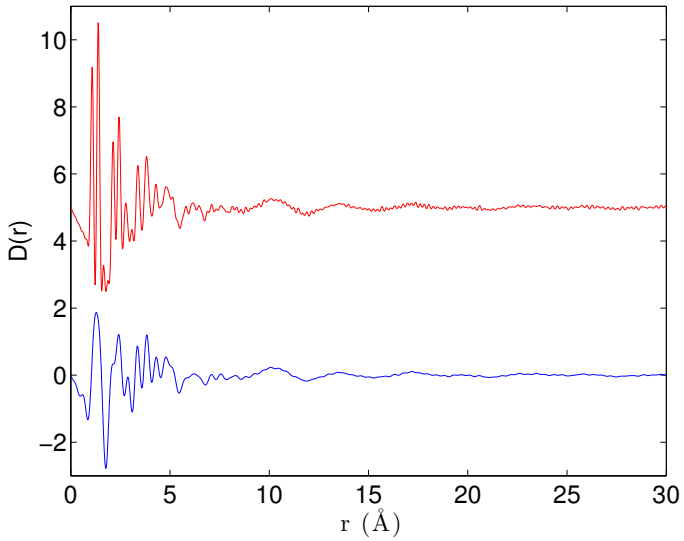

Figure 2.8: Example PDF, $D(r)$, of *ortho*-terphenyl glass showing the effect of the value of $Q_{\max}$. Blue: $Q_{\max} = 15\,\text{Å}^{-1}$; red: $Q_{\max} = 50\,\text{Å}^{-1}$.

reduce the impact of these termination ripples on the obtained PDF, and those ripples produced by the poor signal to noise ratio of $i(Q)$ at high-Q, Gudrun uses a modified Lorch broadening function.

Modified Lorch function

Lorch [37] attempted to derive a function which would suppress the truncation ripples that result from the use of a finite range of Q in a direct Fourier transform of the total scattering function, $i(Q)$. To achieve this $i(Q)$ must smoothly fall to 0 at $Q_{\max}$, so $i(Q)$ is multiplied by a function that does this; the Lorch function, $\sin Q\Delta/Q\Delta$ where $\Delta = \pi/Q_{\max}$. The PDF obtained is therefore the Fourier transform of $i(Q)$ convolved by the Fourier transform of the Lorch function. As the Lorch function is a single peak function that smoothly falls to 0 at $Q_{\max}$ its Fourier transform is a narrow single peak with an approximate width of $2\pi/Q_{\max}$, hence once it is convolved with the Fourier transform of $i(Q)$ it results in broadening of $\Delta = \pi/Q_{\max}$.

A modified form of the Lorch function is used in Gudrun, $\frac{3}{(Q\Delta)^3}(\sin Q\Delta - Q\Delta\cos Q\Delta)$, in which the degree of broadening, Δ, is a width in Å, specified by the user, and that width is a function of r, i.e. $\Delta = \Delta_{(r)}$, with Δ allowed to vary with the form

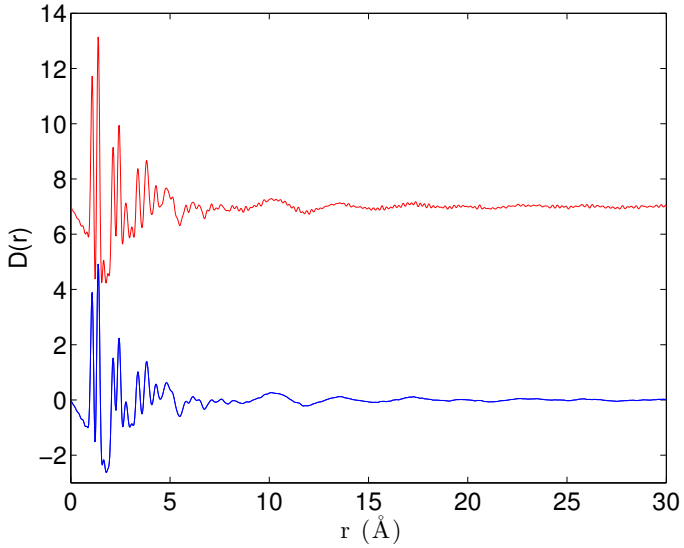

Figure 2.9: Example PDF, $D(r)$, of *ortho*-terphenyl glass showing the effect of a Lorch broadening function. Red: no Lorch; blue: $\Delta_0 = 0.004\,\text{Å}$, $\beta = 0.5$.

$\Delta_{(r)} = \Delta_0(1 + r^\beta)$. β is specified by the user, so the degree of broadening applied to the peaks in a material's PDF can vary with r. The effect of this broadening function can be seen in figure 2.9.

2.3.2 General Structure Analysis System

The general structure analysis system (GSAS) [38] is a program for the structural refinement of materials based on their neutron or X-ray, single crystal or powder, diffraction data and stereochemical restraint data that describes the restraints and constraints on the movement of atoms in the refinement. The refinement technique used by GSAS is the method of least squares in which the square of the difference between a set of observed and calculated points are reduced in an iterative process. The minimisation function, M, of a refinement is made up of several components and is given by equation 2.21

$$M = \sum_h f_h M_h \tag{2.21}$$

where each component of the minimisation function, M_h, can be made up of single crystal diffraction data (M_s), powder diffraction data (M_p) or stereochemical restraint data

(M_r). Each component has an adjustable weighting factor, f_h, that is used to balance the contributions from each data set.

The χ^2 or 'goodness of fit' is defined by the minimisation function as

$$\chi^2 = \frac{M}{N_{\text{obs}} - N_{\text{var}}} \tag{2.22}$$

where N_{obs} is the total number of observations in all data sets and N_{var} is the number of variables in the least squares refinement.

The majority of crystal structure refinements presented in this thesis use the standard Rietveld refinement method [40]. In these refinements powder diffraction data (M_p) and stereochemical restraint data (M_r) are used. In each case the stereochemical restraints used are given in the respective chapters, with full structural details, refinement residuals, and fitted Bragg profiles, in Appendix A. However in two cases, the high-temperature phases of adamantane and its carboxylic acid derivative, due to their disordered structures, a Rietveld refinement without partial occupancies was not possible. The justification for performing a full Rietveld refinement is that it produces a crystal structure that may be trivially transformed into the initial configuration for RMC as well as the Bragg profile, lattice parameters, peak shape, background and scale parameters required. If however, there are partial occupancies in the refined crystal structure, the structure is of limited value in the production of the initial configuration for RMC. Therefore, Le Bail refinements, that still extract the Bragg profile and the other required parameters but do not refine a crystal structure, and so require fewer user inputs, were used in these two cases.

2.4 Reverse Monte Carlo

The RMC refinements in this thesis were performed using the program RMCProfile [41]. RMCProfile is a significant advancement on the original RMC program, RMCA [24, 25], that was designed to refine liquid and amorphous materials, in that it is designed to refine disordered crystalline materials. This advancement comes about due to the explicit use of the information contained within the Bragg data, that tells you about the average

structure, by adding a χ^2_{Bragg} term to the basic RMC cost function given in equation 1.7. Recently, and further developed by the author as described in this thesis, a new potentials term that helps restrain the planar portions of molecular materials has also been added to the cost function.

2.4.1 Equations and Functions

RMCProfile refines against three data types, the total scattering function, the PDF and the Bragg scattering as well as an energy restraint term, hence the cost function is defined as

$$\chi^2_{\text{RMC}} = \chi^2_{i(Q)} + \chi^2_{\text{PDF}} + \chi^2_{\text{Bragg}} + \Delta E/k_{\text{B}}T \tag{2.23}$$

where each of the first three terms corresponds to a particular quantity extracted from the experimental data and the last term corresponds to the energy potentials used to restrain the molecular portion of the material (T is the temperature of the experiment, and k_{B} is the Boltzmann constant).

The relative weightings of the four terms in equation 2.23 that contribute to the overall χ^2_{RMC} are empirically determined factors and are expanded upon below. These weighting factors, and so the relative contribution of each term to χ^2_{RMC}, is checked though test RMC runs to ensure that the difference between experimental and calculated functions is consistent with the noise in the data.

The first component in the total cost function is that arising from the comparison of the total scattering function, $i(Q)$, calculated from the RMC configuration and that extracted from the total scattering data. The $i(Q)$ cost function is thus defined as

$$\chi^2_{i(Q)} = \sum_j \frac{\left[i_{\text{calc}}(Q_j) - i_{\text{expt}}(Q_j)\right]^2}{\sigma_j^2} \tag{2.24}$$

where the subscripts 'calc' and 'expt' correspond to the functions calculated from the RMC configuration and the experimental values respectively. Q_j is the value of the scattering vector Q for any point j in the experimental data. σ_j is a weighting factor, which could in principle be given per point, but in practice we use a constant value for all j that is chosen to reflect the average per-point experimental error.

However, the $i(Q)$ data calculated from the configuration, $i_{\mathrm{calc}}(Q)$ in equation 2.24, are obtained by taking the Fourier transform of the $D(r)$ calculated from the configuration. The consequence of this limited r range, due to the limited size of the configuration, is that the peaks in the calculated $i(Q)$ are broadened. Hence, the calculated $i(Q)$ cannot be compared to the experimental $i(Q)$ until the experimental $i(Q)$ has undergone peak broadening by convolution with a box function defined by the dimensions of the configuration. This convolution is given by

$$i_{\mathrm{convol}}(Q) = \frac{1}{\pi}\int_{-\infty}^{\infty} i_{\mathrm{expt}}(Q')\frac{\sin L(Q-Q')/2}{Q-Q'}dQ' \tag{2.25}$$

where L is the smallest dimension of the configuration and so defines the upper limit of the calculated $D(r)$ and $i_{\mathrm{expt}}(\mathrm{Q}')$ is the raw experimental $i(Q)$. It is the convoluted $i_{\mathrm{convol}}(Q)$, not $i_{\mathrm{expt}}(Q')$ that is compared to the calculated $i(Q)$. Therefore convolution would suggest it is better to have a larger configuration, the larger the configuration the less broadening to the $i_{\mathrm{expt}}(Q')$ data due to convolution, and the less degradation necessary the more potentially accurate the RMC refinement. However, the computational costs of an RMC refinement scale as a function of r^3 where r is the configuration side length. Therefore the size of the initial configuration is a compromise between these two factors, achieving the minimum necessary convolution while incurring a reasonable computational cost.

The second component of the total cost function is that arising from the comparison of the PDF calculated from the RMC configuration and that extracted from the total scattering data. The PDF cost function is thus defined as

$$\chi^2_{\mathrm{PDF}} = \sum_j \frac{[D_{\mathrm{calc}}(r_j) - D_{\mathrm{expt}}(r_j)]^2}{\sigma_j^2} \tag{2.26}$$

where r_j is the distance corresponding to point j in the experimental PDF. As for $\chi^2_{i(Q)}$, we use a constant weighting factor σ_j; in this case it is not possible to obtain a per-point value from the experimental data as it could be in principle for $i(Q)$, and so a constant value of σ_j for all j, which is chosen based on the apparent noise in the $D(r)$ function at high-r, is the only possible choice.

As $i(Q)$ and $D(r)$ are transformations of each other it may seem computationally

wasteful to use them both in an RMC refinement. However, whilst it is true that $i(Q)$ and $D(r)$ are derived from the same structural information, $D(r)$ is actually the transform of the function $Qi(Q)$ rather than $i(Q)$, and thus $D(r)$ reflects a different weighting of the scattering data. In particular, $D(r)$ places more weight on the local structure than would be obtained directly from $i(Q)$. Given that we use uniform rather than by-point values of the weighting parameters σ in the cost functions $\chi^2_{i(Q)}$ and χ^2_{PDF}, use of $i(Q)$ and $D(r)$ also represent different weightings on the data. Thus inclusion of cost functions associated with both $i(Q)$ and $D(r)$ reflect different weightings of the experimental data and so reflect different parts of the information contained within the data. Therefore, despite their close relationship using both in an RMC refinement provides additional data for the refinement.

The third component of the total cost function is that arising from the comparison of the calculated and experiment Bragg profile function. The Bragg cost function is thus defined as

$$\chi^2_{\mathrm{Bragg}} = \sum_j \frac{[I_{\mathrm{calc}}(t_j) - sI_{\mathrm{expt}}(t_j)]^2}{\sigma_j^2} \tag{2.27}$$

where t_j is the time-of-flight of the neutrons for a given value of d-spacing in the time-of-flight diffractometer, s is a scale factor, σ_j is a weighting factor that represents the experimental error on the function $I(t_j)$. The function $I(t_j)$ is the intensity of the Bragg profile determined by the crystallographic structure factor, peak shape parameters and the instrument resolution function, handled as in a conventional Rietveld refinement. RMC does not refine the peak shape parameters or instrument resolution function once they have been set by a prior refinement.

Unlike in equation 2.27 neither equations 2.24 or 2.26 involve a scale factor. This is due to the fact that both the total scattering function, $i(Q)$, and the PDF, $D(r)$, are put on an absolute scale by comparison with the incoherent scattering from a vanadium standard sample, see section 2.3.1. However the Bragg profile function, $I(t)$, is not on an absolute scale and so a scale factor must be applied to the experimental function before it can be compared to the calculated function.

The fourth component of the total cost function is that arising from the comparison of the energy of the atomic configuration before and after the proposed atomic move. The

energy potentials function is thus defined as

$$\Delta E = E_{\text{unmoved}} - E_{\text{moved}} \tag{2.28}$$

where E_{unmoved} is the energy of the unmoved state and E_{moved} is the energy of the moved state. The energy potentials that give rise to these terms are fully described in section 2.4.3.

Before this thesis the structural parameters that could have an energy potential applied to them in RMCProfile are bond lengths and bond angles, two and three body potentials. The range of possible parameters that can be restrained in this manner has subsequently been expanded by the author (see section 2.4.4).

2.4.2 Parameters

To perform an RMCProfile refinement a set of parameters relating to the material being investigated are specified. Along with the post-processing experimental data; the PDF, the total scattering function and the Bragg data, these parameters give RMCProfile all the information required to perform a refinement.

Maximum Move

The maximum move parameter specifies the maximum magnitude of an atomic move that can be made during an RMC refinement. The magnitude of an atomic move in RMC is given by $\alpha_j \eta$, where α_j is the maximum move of atom type j and η is a random number between -1 and +1. The arbitrary value of 0.1 Å is assigned to the lightest atom type, deuterium in all the materials presented (α_{D}), and then values are calculated for the other atom types in the material, based on this value of 0.1 Å. These calculations are done based on a comparison of the square roots of the masses of the constituent atoms, reflecting the approximate thermal motion of the constituent atoms.

Neutron Scattering Lengths and Coefficients

Neutron scattering lengths are tabulated and freely available for all atoms [28], they are an intrinsic property of a nucleus and so do not change due to any external factor.

Hence, a single neutron coefficient can be calculated for each atom pair that is valid for all materials and phases, assuming a known distribution of isotopes. Neutron coefficients are calculated using the formula $c_i b_i c_j b_j$, where c_i is the concentration of atom i within the material and b_i is the neutron scattering length of atom i, for example in $Zn(Im)_2$ c_{Zn} is 1/17 and b_{Zn} is 5.680 fm. Their utility is in the calculating of scattering data from the refinement cell, see section 2.2.1.

Number Density

The number density is the number of atoms per unit volume. The exact value is calculated for each temperature and material based on the number of atoms in the unit cell and the volume of the unit cell as determined by GSAS. As neither the number of atoms within it nor the volume of the unit cell are refined during RMC, the number density does not change either. Its utility is in the calculating of scattering data from the refinement cell, see section 2.2.1.

Configuration

A number of parameters are given that fully describe the initial configuration. First the configuration's size (in Å) is given; this is specified by the three lengths a, b and c and the three angles α, β and γ. Next the number and fractional coordinates of all the atoms in the initial configuration are given.

A summary of the configuration parameters used in the presented RMC refinements are given in their respective chapters, with full configurational details and all other parameters given in Appendix B.

2.4.3 Constraints and Restraints

Total scattering data does not always provide RMCProfile with enough information to perform a refinement that is consistent with prior chemical knowledge. For example an atomic move may be accepted by the RMC algorithm that will bring two atoms too close together, as shown by the unphysical distance between deuterium atoms in the RMC configuration of *ortho*-terphenyl in figure 2.10. Therefore a number of constraints, hard restrictions that can not be broken by the refinement, and restraints, soft restrictions

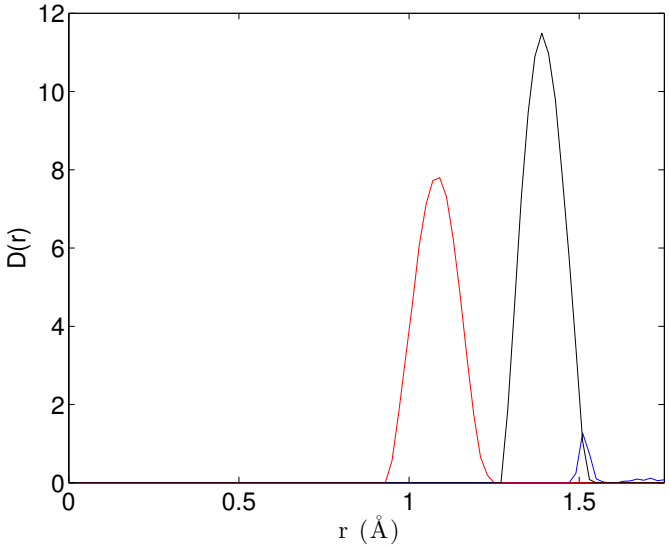

Figure 2.10: Low r region ($r \leq 1.75\,\text{Å}$) of the PDF partials, $g_{m,n}(r)$, for *ortho*-terphenyl showing the unphysical short D–D distance generated by RMC without the use of appropriate constraints. C–C: black; C–D: red; D–D: blue.

that may be broken by the refinement, are applied that help to guide the refinement, preventing unphysical configurations.

One of the principles of an RMC refinement is that it is a data-driven refinement; that the atomic structure it produces is entirely based on experimental data, not what is suggested by theory. In principle the experimental total scattering data should be sufficient to perform an RMC refinement and the use of constraints and restraints, which move RMC away from a purely data-driven refinement technique, should be unnecessary. However, to overcome the issue of the possible production of unphysical configurations and the problems poised by molecular materials, they may play an important role.

In molecular materials the size and shape of individual molecules are often well defined by prior chemical knowledge. However RMC refinements do not have this chemical knowledge and so will move atoms without regard for maintaining the size and shape of these molecules as long as the fit to data is improved, χ^2_{RMC} is lowered. The application of constraints and restraints prevents RMC from making moves, that although they may lower χ^2_{RMC}, go against prior chemical knowledge. As long as appropriate weighting factors and values are used, constraints and restraints do not control the overall refinement, rather they guide it by preventing RMC from 'breaking' well understood molecular structures.

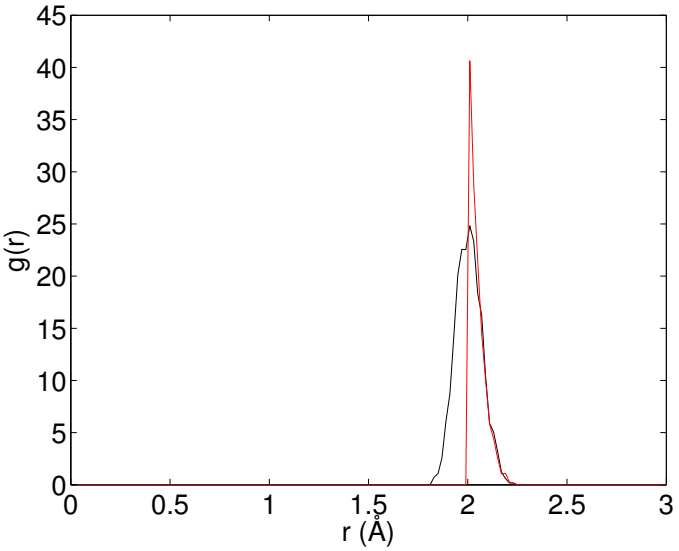

Figure 2.11: Low r region ($r \leq 3\,\text{Å}$) of the PDF partial of Zn–N, $g_{Zn,N}(r)$, in ZIF-4 showing an unphysical cut-off if a minimum distance of $2\,\text{Å}$ is applied to the Zn–N distance. Red: Zn–N minimum distance $= 2\,\text{Å}$; black: Zn–N minimum distance $= 1.8\,\text{Å}$.

Minimum Distance of Approach

The minimum distance of approach between two atoms is a constraint; it can not be broken. If a proposed atomic move would break it then the proposed move is rejected. It is initially set by a consideration of the structure of the material under investigation and the minimum physically acceptable value that this suggests. These distances are then refined by analysing the PDF partials, the PDF of a specific pair of atoms, after test RMC runs, such that any unphysical cut-offs or intensities, an example of which is shown by the red line in figure 2.11, are minimised. These unphysical cut-offs or intensities represent areas in the refinement where χ^2_{RMC} can be lowered by breaking a minimum distance constraint. As these moves are not accepted, atoms 'bunch' at these distances - resulting in the unphysical cut-offs or intensities.

Distance Windows

Distance windows are a range of distances that are allowed between an atom pair. Like minimum distances of approach, distance windows are a constraint; they can not be broken. If a proposed atomic move would break it then the proposed move is

rejected. It is initially set by a consideration of the material under investigation and the physically acceptable range that this suggests. These distance ranges are then refined by analysing the PDF partials in a procedure analogous to that described above for the refinement of minimum distances.

Potentials

Potentials are energy restraints that can be applied to two or three atom interactions; a bond or angle, giving an energy cost to the refinement if one of these bonds or angles move away from the theoretical ideal. Unlike the minimum distance of approach and distance window constraints described above, potentials are a restraint. If a proposed atomic move would increase the energy given by a potential, the atomic move is not immediately rejected, the probability of the move being accepted is just lowered.

Potentials are applied by defining the energy of the bond, or angle, and the ideal bond length, or angle, for each atom set concerned. A Morse potential, equation 2.29, or simple harmonic cosine potential, equation 2.30, is then applied giving the energy of the change in the bond distance or angle resulting from a proposed atomic move.

$$E = D[(1 - \exp(-\alpha(r_{ij} - r_0)))^2] \tag{2.29}$$

where D is the energy of the bond (in eV), r_{ij} and r_0 are the instantaneous and ideal bond lengths between atoms i and j respectively (in Å) and α specifies the curvature of the potential energy surface near the minimum (following the MM3 molecular mechanics force field model it is set to $2.55\,\text{Å}^{-1}$ for all atom pairs [42]).

$$E = \frac{K}{2}(\cos\theta_{ijk} - \cos\theta_0)^2 \tag{2.30}$$

where K is the energy of the angle (in eV), θ and θ_0 are the instantaneous and ideal bond angles between atoms i, j and k respectively (in degrees).

The summation of all the energy terms of all the potentials applied to a refinement gives rise to the fourth term in the total cost function χ^2_{RMC}, given in equation 2.23.

Therefore if a proposed atomic move would increase this energy, the probability of the proposed atomic move being rejected under the RMC algorithm is increased.

The degree to which a potential affects an RMC refinement, the contribution to χ^2_{RMC} it makes, is dependant on the energy value of the potential and the temperature of the refinement, equation 2.23. The higher the energy the greater the cost to refinement given if a proposed atomic move would alter the value of a bond length or bond angle away from the ideal value. For bond and angle potentials the energy values, D in equation 2.29 and K in equation 2.30, are taken from the standard MM3 [42] potentials.

The lower the temperature of the refinement the higher the weighting of the energy change term in equation 2.23 and so the greater the cost to refinement that would result if a proposed atomic move would alter the value of a bond length or bond angle away from the ideal value. Theoretically the experimental temperature of the data used in the refinement should give the correct weighting and cost to the refinement if a potential's energy value is changed. However it was found that at low temperatures the use of the experimental temperature 'over constrained' the refinement. The weighting of the potentials were too high relative to the weighting of the experimental data, resulting in the refinement being controlled rather than guided by the potentials. This was seen empirically in the poor fit of the low-r peaks of the PDF, shown in figure 2.12, therefore the temperature used in equation 2.23 was raised such that the PDF fit was improved.

2.4.4 Development of Planarity Potentials

Molecules of both *para*- and *ortho*-terphenyl (PTP and OTP) consist of six membered carbon rings for which, due to the π conjugation between the carbon electrons, it is energetically favourable for the carbon atoms to stay planar. If all the carbons stay in the same plane then their p orbitals can overlap more strongly resulting in a lower energy structure, a conjugation stabilisation energy. However, RMC refinements do not have this chemical knowledge and so will move atoms without regard for maintaining the planarity of these rings as long as the fit to data is improved, the χ^2_{RMC} is lowered. Therefore, to

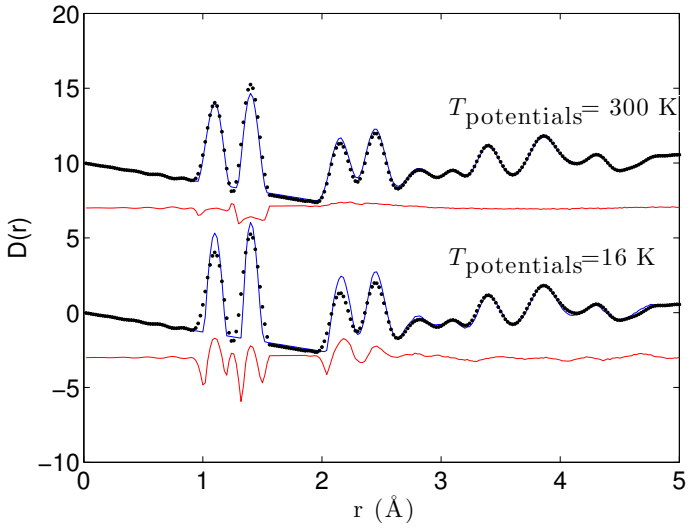

Figure 2.12: Low r region ($r \leq 5$ Å) of the PDF fits for *ortho*-terphenyl showing the poor fit given if the experimental temperature of 16 K is used as T in equation 2.23 ($T_{\text{potentials}}$) and how the fit is improved by using $T_{\text{potentials}} = 300$ K. Experimental data: black dots; RMC fits: blue line; difference: red line.

represent this conjugation stabilisation energy in the refinement of molecular structures with conjugated rings code for a new planarity potential in RMCProfile has been written and implemented by the author. Like bond and angle potentials, planarity potentials are a restraint; they increase the value of χ^2_{RMC} if a proposed atomic move would reduce planarity, they do not reject the move.

Planarity potentials were implemented in the same way as bond length and angle potentials. First a planarity file that lists all the planes of atoms to be restrained, analogous to the bond or triplet files for bond or angle potentials [43], is produced. Example planarity files with a description of their format and the code, written by the author, to produce them are given in Appendix C.

Secondly the planarity energy, the energy due to the energetic preference for a group of atoms to stay in a plane, is calculated for the initial configuration. This energy is calculated by producing a value of the deviation from planarity for each group of atoms specified in the planarity file and then multiplying this quantity by an energy term, known as the plane energy, equation 2.31. This plane energy is analogous to the bond energy, D

in equation 2.29, or the angle energy, K in equation 2.30.

$$E = P\omega \tag{2.31}$$

where P is the plane energy and ω is the instantaneous deviation from planarity (in Å^2), the procedure used to calculate ω is described below. This is done for all the planar groups of atoms specified and summed over all planes to give a total initial planarity energy.

Thirdly for each iteration of the RMC algorithm, each proposed atomic move, an energy change term is calculated; the difference in the planarity energy of the configuration before the proposed atomic move and that of the configuration after the proposed atomic move. The planarity energy of the moved configuration is subtracted from the planarity energy of the unmoved configuration to give the energy change term. If a negative energy change term is given then the deviation from planarity would be increased by the proposed move. Thus a negative energy change term represents a 'cost to refinement', a term that contributes to a raising in χ^2_{RMC}, making such a proposed move less likely to be accepted.

The deviation from planarity, ω, is calculated via a plane fitting of observed points using orthogonal regression, the key equations for this regression are presented in section four of [44] and outlined below. This is a least squares fitting procedure in which the error between the proposed plane and the observed points, six points in the case of PTP or OTP; the coordinates of the six carbons, are measured orthogonally to the proposed plane rather than vertically. Let the plane be $\mathbf{N} \cdot (\mathbf{X} - \mathbf{A}) = 0$ where $\mathbf{N}$ is a unit length normal to the plane and $\mathbf{A}$ is a point on the plane. Define $\mathbf{X}_i$ to be the sample points; then

$$\mathbf{X}_i = \mathbf{A} + \lambda_i \mathbf{N} + p_i \mathbf{N}_i^{\perp} \tag{2.32}$$

where $\lambda_i = \mathbf{N} \cdot (\mathbf{X}_i - \mathbf{A})$ and $\mathbf{N}_i^{\perp}$ is some unit length vector perpendicular to $\mathbf{N}$ (parallel to the plane) with appropriate coefficient p_i. Define $\mathbf{Y}_i = \mathbf{X}_i - \mathbf{A}$. The vector from $\mathbf{X}_i$ to its projection onto the plane is $\lambda_i \mathbf{N}$, the error used in the least square fitting procedure is the squared length of this vector, $\lambda_i^2 = (\mathbf{N} \cdot \mathrm{Y}_i)^2$. The energy function for the least squares

minimisation is therefore $E(\mathbf{A},\mathbf{N}) = \sum_{i=1}^{m} \lambda_i^2$. Two alternate forms of this function are

$$E(\mathbf{A},\mathbf{N}) = \sum_{i=1}^{m} (\mathbf{Y}_i^{\mathrm{T}} [\mathbf{N} \cdot \mathbf{N}^{\mathrm{T}}] \mathbf{Y}_i) \tag{2.33}$$

and

$$E(\mathbf{A},\mathbf{N}) = \mathbf{N}^{\mathrm{T}} (\sum_{i=1}^{m} \mathbf{Y}_i \mathbf{Y}_i^{\mathrm{T}}) \mathbf{N} = \mathbf{N}^{\mathrm{T}} M(A) \cdot \mathbf{N} \tag{2.34}$$

Using the form of E in equation 2.33, take the derivative with respect to A to get

$$\frac{dE}{dA} = -2[\mathbf{N} \cdot \mathbf{N}^{\mathrm{T}}] \sum_{i=1}^{m} \mathbf{Y}_i \tag{2.35}$$

This partial derivative is zero whenever $\sum_{i=1}^{m} \mathbf{Y}_i = 0$ in which case $\mathbf{A} = (1/m) \sum_{i=1}^{m} \mathbf{X}_i$ (the average of the sample points).

Given $\mathbf{A}$, the matrix $M(A)$ is determined in the second form of the energy function. The quantity $\mathbf{N}^{\mathrm{T}} M(A) \mathbf{N}$ is a quadratic form whose minimum is the smallest eigenvalue of $M(A)$. This is the value of the deviation from planarity, ω. If $\mathbf{A} = (a, b, c)$, then matrix $M(A)$ is given by

$$M(A) = \begin{bmatrix} \sum_{i=1}^{m} (x_i - a)^2 & \sum_{i=1}^{m} (x_i - a)(y_i - b) & \sum_{i=1}^{m} (x_i - a)(z_i - c) \\ \sum_{i=1}^{m} (x_i - a)(y_i - b) & \sum_{i=1}^{m} (y_i - b)^2 & \sum_{i=1}^{m} (y_i - b)(z_i - c) \\ \sum_{i=1}^{m} (x_i - a)(z_i - c) & \sum_{i=1}^{m} (y_i - b)(z_i - c) & \sum_{i=1}^{m} (z_i - c)^2 \end{bmatrix} \tag{2.36}$$

Code to calculate the deviation from planarity following the method described above is given in Appendix C.

To test the effectiveness of planarity potentials on an RMC refinement a number of short test refinements of PTP were run with a plane energy of either zero, 500 or 1000, keeping all other parameters equal. The configurations given by these three refinements were then analysed to give a histogram of the deviation from planarity for each individual ring, shown in figure 2.13. This shows that, as expected, a higher value of the plane energy results in a lower deviation from planarity.

Unlike the bond and angles energies, D in equation 2.29 and K in equation 2.30, whose value is taken from the standard MM3 [42] potentials, there are no established

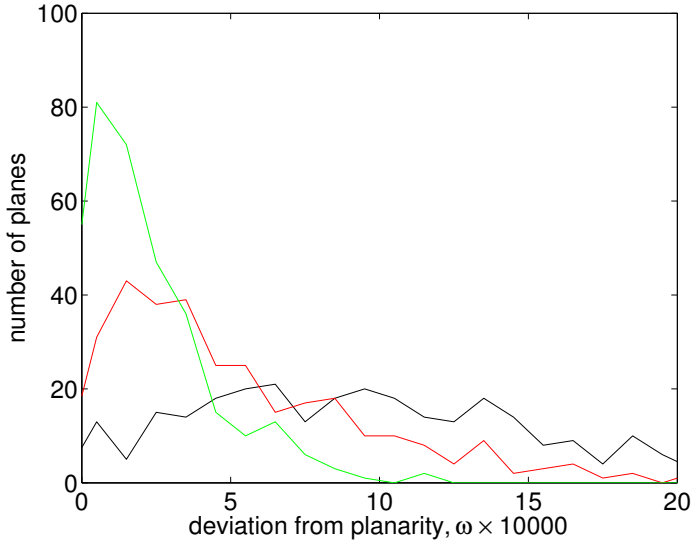

Figure 2.13: A histogram of the deviation from planarity of the 6 membered carbon rings in PTP as the plane energy is increased. Black: planarity potential with a plane energy of 0; red: planarity potential with a plane energy of 500; green: planarity potential with a plane energy of 1000.

values for the plane energy, P in equation 2.31. Hence a suitable value for this energy had to be established. A value that gives results consistent with prior chemical knowledge, configurations with planar rings for all refinement temperatures where the thermal energy is insufficient to result in ring buckling, but not too high that it starts to over-constrain the refinement. Therefore test RMC refinements of PTP were run with a plane energy of 1000, 5000 and 10000, keeping all other parameters equal, with the average deviation from planarity given in figure 2.14. Based on these results and a visual inspection of the rings produced by these refinements, ensuring no rings have buckled in an unphysical manner, the values of 5000 or 10000 were considered for P.

A planarity constraint, applied to a phenyl ring with too high a plane energy, would have the effect of reducing the movement of the carbon atoms in the refinement with respect to the movement of the deuterium atoms. This is because the planarity constraint, if using too high a plane energy, would restrict the movement of the atoms that it is applied to such that they move less than they would in a purely data-driven refinement; over-constraining the refinement. Therefore, to establish which value to use for the plane energy, 5000 or 10000, the average atomic move through refinement, grouped by atom type, in the test refinements described above, were calculated and are shown for refine-

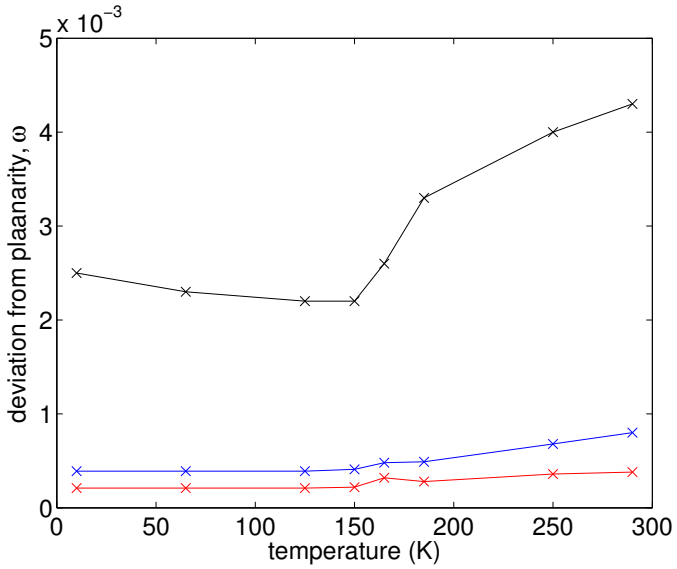

Figure 2.14: Average deviation from planarity of the 6 membered carbon rings in PTP as the temperature is increased. Black: $P = 1000$; blue: $P = 5000$; red: $P = 10000$.

ments at 150 K in figure 2.15. The average atomic moves are given in figure 2.15(a) with the ratio in figure 2.15(b). These show that there is a small reduction in the average carbon move, with respect to deuterium, using a plane energy of 5000, but that it is a marginal effect compared to that seen when using a plane energy of 10000. Therefore, as both give a similar reduction in the deviation from planarity as shown in figure 2.14, the value of 5000 was selected for P. The code, written by the author, to calculate these atomic moves is given in Appendix C.

2.5 Analysis

Once the value of χ^2_{RMC} has levelled off and is oscillating around a minimum value, the RMC refinement is considered to have equilibrated. That the current configuration of atoms gives the most accurate representation of the material under investigation that is possible given the experimental data used. The theoretical interpretation of this point is given in section 1.3.1. In practice the individual values of χ^2 are output by the RMCProfile program at intervals specified by the user, every 10000 atomic moves for example. These values are then plotted against move number, as illustrated in figure 2.16, and it is

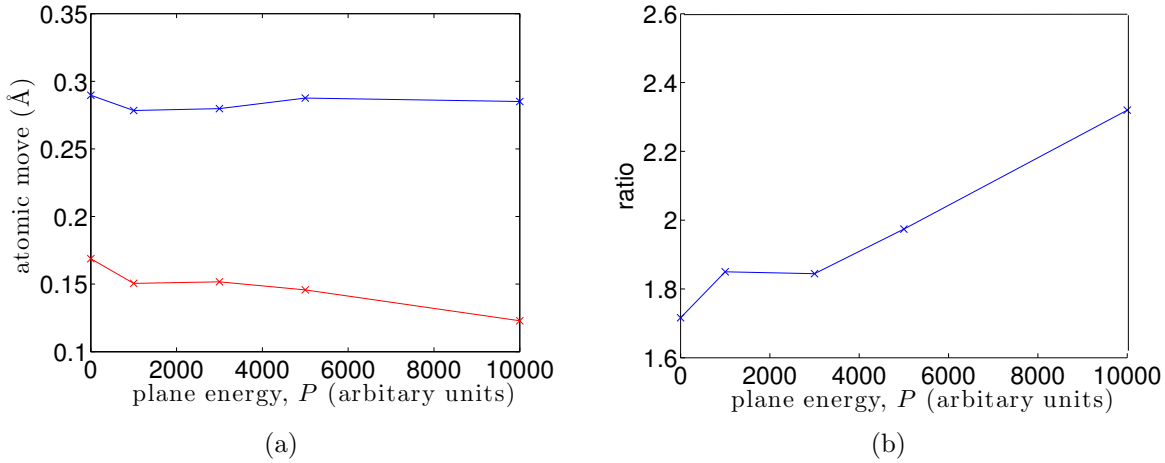

Figure 2.15: Average atom moves in PTP at 150 K as the plane energy is increased. (a) Blue: D; red: C. (b) Ratio of D/C.

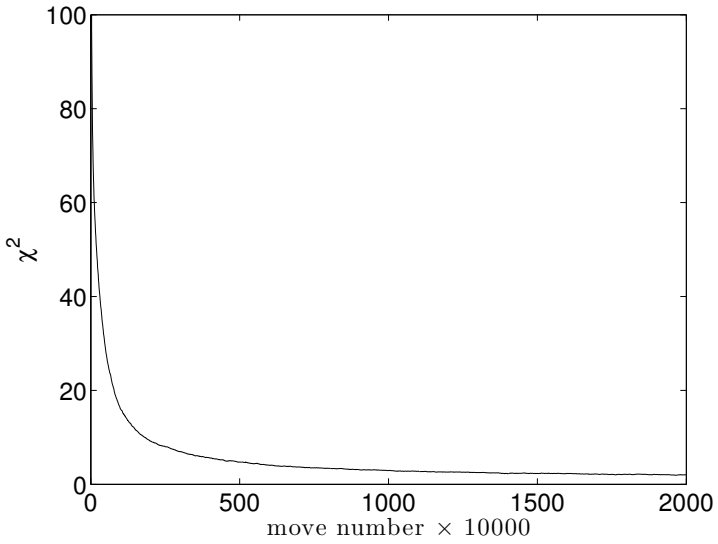

Figure 2.16: The levelling of in the value of χ^2_{RMC} that indicates the RMC refinement has equilibrated.

when these graphs have had an average gradient of 0 for a period of time that the RMC refinement is terminated by the user.

The primary output of RMC is a final configuration, a box of atoms. It has the same size and shape as the initial configuration, the same number of atoms and therefore the same density but with atomic coordinates that have been refined according to the total scattering data. These final configurations are then analysed to give information

concerning a set of parameters that are relevant to the material under investigation. To do this bespoke Fortran codes were designed and written by the author for each material studied, the specific structural parameters that were calculated are described in the relevant chapters.

These analysis codes consist of two parts. First, common core analysis codes that produced histograms, averages and standard deviations of selected bond length and angle distributions from the final RMC configurations, taking the periodic boundary conditions of the configurations into account, were written. To achieve this, this portion of the codes uses both the final configuration, in the form of a list of atomic coordinates - a *.rmc6f* file [43], and the atomic connectivity, in the form of a list of atoms connected by a distance window - a *.neigh* file [43], to produce the vectors between all connected atoms. Periodic boundary conditions are then taken into account such that individual vectors are not distorted by periodic boundaries, the bond lengths and three atom angles of all specified atoms are then calculated from the their respective vectors.

Then the bespoke functionality required to investigate the specific features of each material was built upon this core code. To achieve this, the bespoke portions of each code uses the same configurations and connectivity as used by the core analysis code, using this information to define larger units within the material. These units, rings or molecules in the material, then have periodic boundary conditions taken into account such that individual units are not distorted by periodic boundaries. Once defined any structural property of these units may be calculated - the torsion angle between them, their distribution with respect to each other or their relative rotation. These bespoke codes, for all materials, are given in Appendix C.

Chapter 3

Zeolitic Imidazolate Framework Materials

3.1 Introduction

Over the past two decades, metal-organic framework materials (MOFs) [45–47] have been intensively studied by the materials science community. These materials consist of networks of metal ions linked in a 3D framework by organic ligands. Due to the wide range of possibilities, and relative ease with which the metal or organic components of these materials can be substituted, MOFs have a remarkable chemical and structural versatility [48]. Therefore MOFs have a wide range of potential applications, including gas sorption [49–51] and separation [52, 53], catalysis [54, 55], magnetism [56] and photoluminescence [57, 58].

Zeolitic imidazolate framework materials (ZIFs) are a class of MOF that consist of a network of $\mathbf{M}N_4$ ($\mathbf{M} = 2^+$ transition metal ion) tetrahedra connected by substituted or unsubstituted imidazolate rings (Im = $C_3N_2H_3^+$), as illustrated for the unsubstituted case in figure 3.1 [59]. They were designed specifically to mimic silicate framework structures, which are composed of corner-sharing SiO_4 and AlO_4 tetrahedra. In most silicates the Si–O–Si bond subtends an angle of around 145°, which corresponds to the angle subtended by the two Zn–N bonds in the Zn–Im–Zn linkage, as illustrated in figure 3.2. And indeed, ZIFs form a range of phases that are direct and indirect analogues of silica zeolite structures, which are low-density structures with open channels and cages. This porous structure combined with comparatively high chemical and thermal stability [60] makes ZIFs an interesting set of compounds with respect to applications of gas storage and separation [61].

The pores in each different ZIF are a different volume, assessed by the solvent accessible volume (SAV) shown in figure 3.3, and depending on the ZIF account for approximately

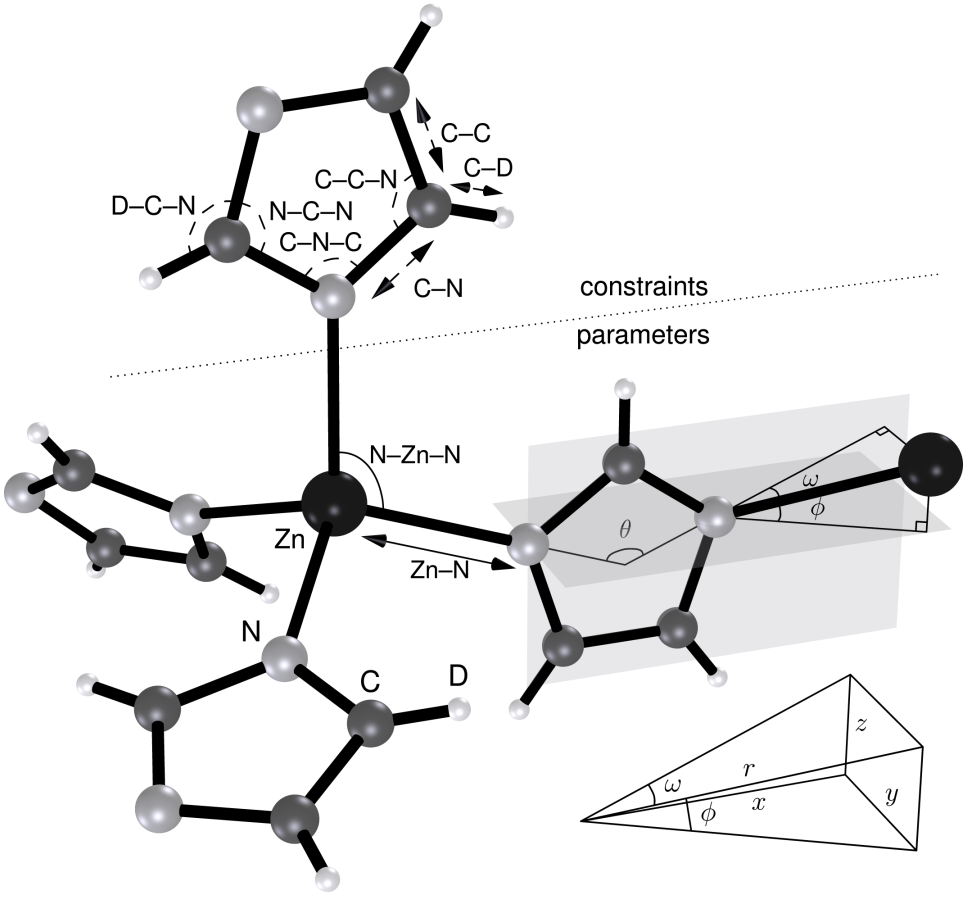

Figure 3.1: Schematic diagram of the structure of $Zn(im)_2$, showing the ZnN_4 tetrahedra linked by imidazole rings. The potentials applied to constrain the structural refinement are shown by dashed lines in the top section of the figure. The parameters that characterise the system's structural flexibility are indicated by solid lines in the middle section. The inset, bottom right, demonstrates the geometric relationship between the angles ω and ϕ: $\sin^2\omega+\sin^2\phi = y^2/r^2+z^2/r^2 = 1-x^2/r^2 \leq 1$.

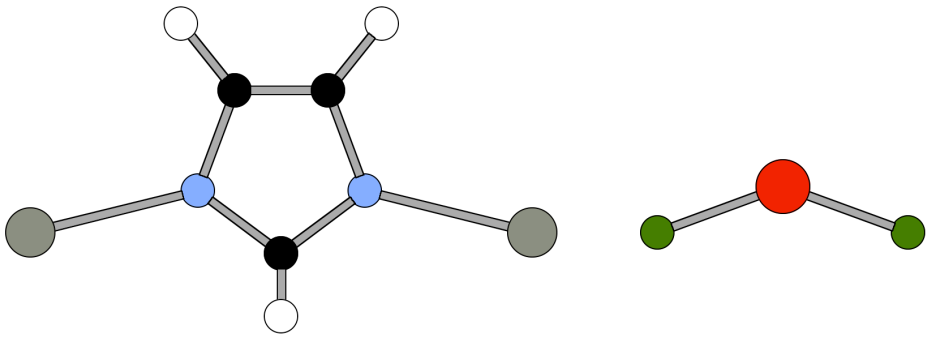

Figure 3.2: The structural analogy between ZIFs and SiO_2, particularly the analogous 145° Si–O–Si and Zn–Im–Zn angles. H: white; C: black; N: blue; Zn; grey; Si: green and O: red.

30–40% of the unit cell volume. These pores are typically of the correct volume to accept a small guest molecule, such as CO_2 [61]. The chemical and thermal stability of ZIFs mean that the pores in their framework structures do not collapse when guest molecules are removed, they remain open to reaccept other guest molecules. This gives ZIFs the potential property of recyclability, being able to be used through many cycles of adsorption and reabsorption, a key property required for any industrially useful gas storage or separation material.

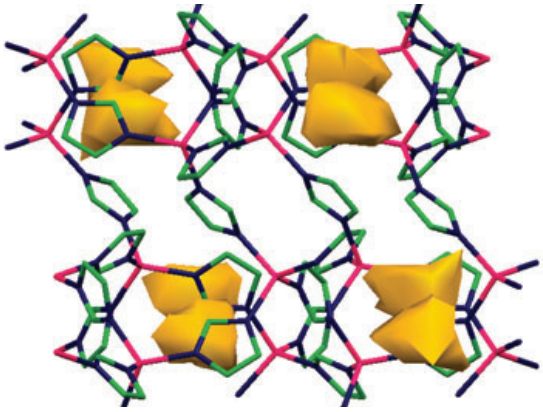

Figure 3.3: The solvent accessible volume in ZIF-4, represented by yellow isosurfaces, viewed along the c axis. Zn: pink; C: green; N: blue, hydrogen atoms omitted for clarity [62].

The specific ZIF investigated in this study is ZIF-4, which has the formula $Zn(Im)_2$ and consists of tetrahedral Zn^{2+} ions linked in a 3D array with 'cag' topology by unsubstituted imidazole rings [65]. At 573 K, ZIF-4 goes through an amorphization transition, shown by the loss of Bragg peaks, to give an amorphous phase, termed aZIF. This amorphous phase is recoverable to lower temperatures, but on further heating to 673 K, ZIF-zni, the densest and lowest-energy of the crystalline ZIFs [68], evolves from the amorphous phase [67]. ZIF-zni is then stable to about 800 K, at which temperature it decomposes [66]. The existence of these three phases, all with the same chemical composition, gives the opportunity to directly compare the flexibility of these three different phases. Therefore in this chapter the results of a neutron total scattering experiment and the subsequent RMC refinements of the three phases of $Zn(Im)_2$, ZIF-4, aZIF and ZIF-zni are presented.

3.2 Experimental

Bulk samples of fully-deuterated ZIF-4 were prepared via solvothermal reaction of deuterated zinc(II) nitrate hexahydrate and imidazole in deuterated dimethylformamide (DMF) [65]. The sample as prepared contained DMF molecules within its pore structure, but thermogravimetric analysis and variable-temperature X-ray and neutron diffraction data show that the DMF molecules are lost on heating above 473 K, giving a solvent-free nanoporous phase of composition $Zn(Im)_2$ while maintaining the ZIF-4 topology [66]. In this experiment, the solvent was removed *in situ* on the neutron total scattering instrument and monitored in time through measurements of the lattice parameters.

Neutron total scattering data were collected at various temperatures on the GEM diffractometer, as described in section 2.2.3. Data suitable for RMC refinements were obtained at temperatures of 478 K for ZIF-4, 298 and 573 K for aZIF, and 298, 406, 540 and 673 K for ZIF-zni.

3.3 Data Processing

The background was subtracted and the data normalised using the program Gudrun [35] as described in section 2.3.1. During this process it became clear that the incoherent scattering contribution was greater than expected for a fully deuterated sample, causing substantial differences between the high-Q limits of $i(Q)$ for different detector banks. The most likely cause for this, given the large incoherent scattering length of the proton, is that the sample was not in fact completely deuterated. Therefore the deuteration ratio was refined using the Rietveld method, using fixed atomic coordinates and cell parameters with only the deuteration ratio refined, resulting in an elemental composition of $ZnC_6N_4D_{5.6}H_{0.4}$. Thus this composition was assumed, with random H/D distribution, in the subsequent RMC refinements. This was achieved by replacing the deuteriums in the initial RMC configurations with an artificial atom, labelled Ed, that has the neutron scattering length appropriate to an atom that is 93.3% deuterium and 6.7% hydrogen. A sample of the PDFs produced by Gudrun are shown in figure 3.4.

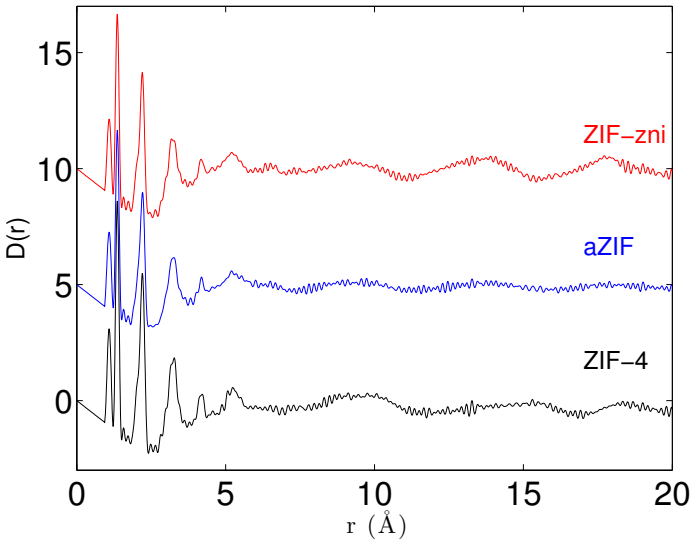

Figure 3.4: PDFs, $D(r)$, for desolvated ZIF-4 478 K, aZIF 298 K, and ZIF-zni 298 K. The three phases have very similar local structure below about 5 Å, but differ in the longer-range correlations above this radius; in particular, aZIF, as expected, has noticeably smaller high-r peaks. ZIF-4: black; aZIF: blue; ZIF-zni: red.

The Bragg diffraction profile was also separately extracted for the crystalline phases, and Rietveld refinement performed using GSAS [38] and EXPGUI [39] in order to extract lattice parameters and to obtain the peak shape, background and scale parameters for use in the RMC refinements. In these Rietveld refinements constraints were placed on the isotropic atomic displacement parameters of all atoms such that all zinc atoms had the same value, all deuterium atoms has the same value and all carbon and nitrogen atoms had the same value. As the within-ring correlations are of no interest in the presented work, the imidazolate rings were treated as rigid bodies during the refinement with only their centre of mass and rotation angles allowed to vary. Additionally the Zn–N bond distance was restrained to 2 Å. Example fits, lattice parameters, cell volumes and the refinement residuals are given in Appendix A.

3.4 Reverse Monte Carlo

3.4.1 Initial Configurations

Initial configurations of ZIF-4 and ZIF-zni were produced for each temperature as 3 × 3 × 3 and 2 × 2 × 4 supercells of their refined crystal structures respectively, obtained by Rietveld refinement, using the program RMCcreate [5]. This procedure resulted in initial configurations of ZIF-4 and ZIF-zni with side length of approximately 50 Å, containing 7344 and 8704 atoms respectively.

Consistent with the previous study of aZIF [66], all attempts to generate an amorphous structure by starting with either of the crystalline phases failed completely. Fits to experimental data were unsatisfactory; an appropriate value of χ^2_{RMC} was not reached, and a consistent amorphous structure did not emerge; the structural parameters calculated from refinements starting from a ZIF-4 initial configuration never agreed with those calculated from refinements starting from a ZIF-zni initial configuration. Thus a new initial configuration for the amorphous phase was produced. A similarity was noted between the PDFs of aZIF and $aSiO_2$, which combined with the structural relationship shown in figure 3.2, lead to the development of the amorphous initial configuration from a well tested SiO_2 continuous random network (CRN) [69]. To achieve this Si was replaced by Zn and O replaced by im, with an approximate doubling of the Si–O distance to match the Zn–im distance [66]. The resulting aZIF configurations were cubic with side length of 53.951 Å and contained 8704 atoms.

Exact structural details and atom numbers of the initial configurations for all three phases of $Zn(Im)_2$ are given in Appendix B

Since the RMC refinement process does not affect the network topology, no bonds are made or broken in an RMC refinement, network topology is entirely determined by the initial configuration. The method used to obtain the original SiO_2 configuration, from which the aZIF configuration was developed, was designed to avoid four-membered rings as they are energetically unfavourable in silica. Given that both the crystalline phases (that is, both the cag and zni topologies) contain four-membered rings, as illustrated

in figure 3.3, such rings appear to be more favourable in the ZIF system than in silica. Thus the initial configuration of aZIF may not reflect the ring size distribution in aZIF in this respect and so, as an RMC refinement can not change network topology, this is a possible cause of error in the refined final configuration of aZIF. Nonetheless, because the overall density of the configuration is correct, and given the quality of the fits between experimental and calculated data produced, the refined final configuration is likely to give an accurate picture of the local distortions within a single Zn–im–Zn linkage.

3.4.2 Constraints and Restraints

A number of constraints, in the form of minimum distances, and restraints, in the form of molecular potentials, were applied to all of the RMC refinements of the three phases of $Zn(Im)_2$ and are given in tables 3.1 and 3.2. One distance window constraint was also applied to these refinements, constraining the Zn–N distance to between 1.8 and 2.5 Å.

atom pair	distance (Å)
Ed Ed	1.80
Ed C	0.94
Ed N	1.80
Ed Zn	1.80
C C	1.00
C N	1.00
C Zn	2.40
N N	1.80
N Zn	1.80
Zn Zn	5.00

Table 3.1: Minimum Distance of Approach

Potentials	Atoms	Values
$E = D[(1 - \exp(-\alpha(r_{ij} - r_0)))^2]$	C–Ed	$D = 2.208$ eV $\alpha = 2.55$ Å^{-1} $r_0 = 1.1$ Å
	N–C C–C	$D = 8.84$ eV $\alpha = 2.55$ Å^{-1} $r_0 = 1.36$ Å
$E = \frac{K}{2}(\cos(\theta_{ijk}) - \cos(\theta_0))^2$	$\widehat{\text{NCN}}$	$K = 39.7$ eV $\theta_0 = 114°$
	$\widehat{\text{NCC}}$	$K = 39.7$ eV $\theta_0 = 109.2°$
	$\widehat{\text{CNC}}$	$K = 39.7$ eV $\theta_0 = 103.7°$
	$\widehat{\text{NCEd}}$	$K = 25.6$ eV $\theta_0 = 124.1°$
	$\widehat{\text{CCEd}}$	$K = 25.6$ eV $\theta_0 = 125.4°$

Table 3.2: Summary of the potentials used in the RMC refinement, adapted from the MM3 potentials [42] as described in the RMCProfile manual [43].

.

3.5 Analysis

In these RMC refinements it was found that the value of the function χ^2_{RMC} decreased towards a converged minimum value after approximately 8 million generated atomic moves, over 1000 moves per atom. At this point the refinements were considered to have reached an equilibrium and so RMC was terminated. For each of the three phases six independent RMC refinements were performed to give improved statistical accuracy to extracted histograms, averages and standard deviations. Examples of the final configurations of all three phases and fits to the $D(r)$, $i(Q)$ functions and, where applicable, Bragg data are shown in figure 3.5.

The basic analysis described in section 2.5 calculates the Zn–N bond distance and

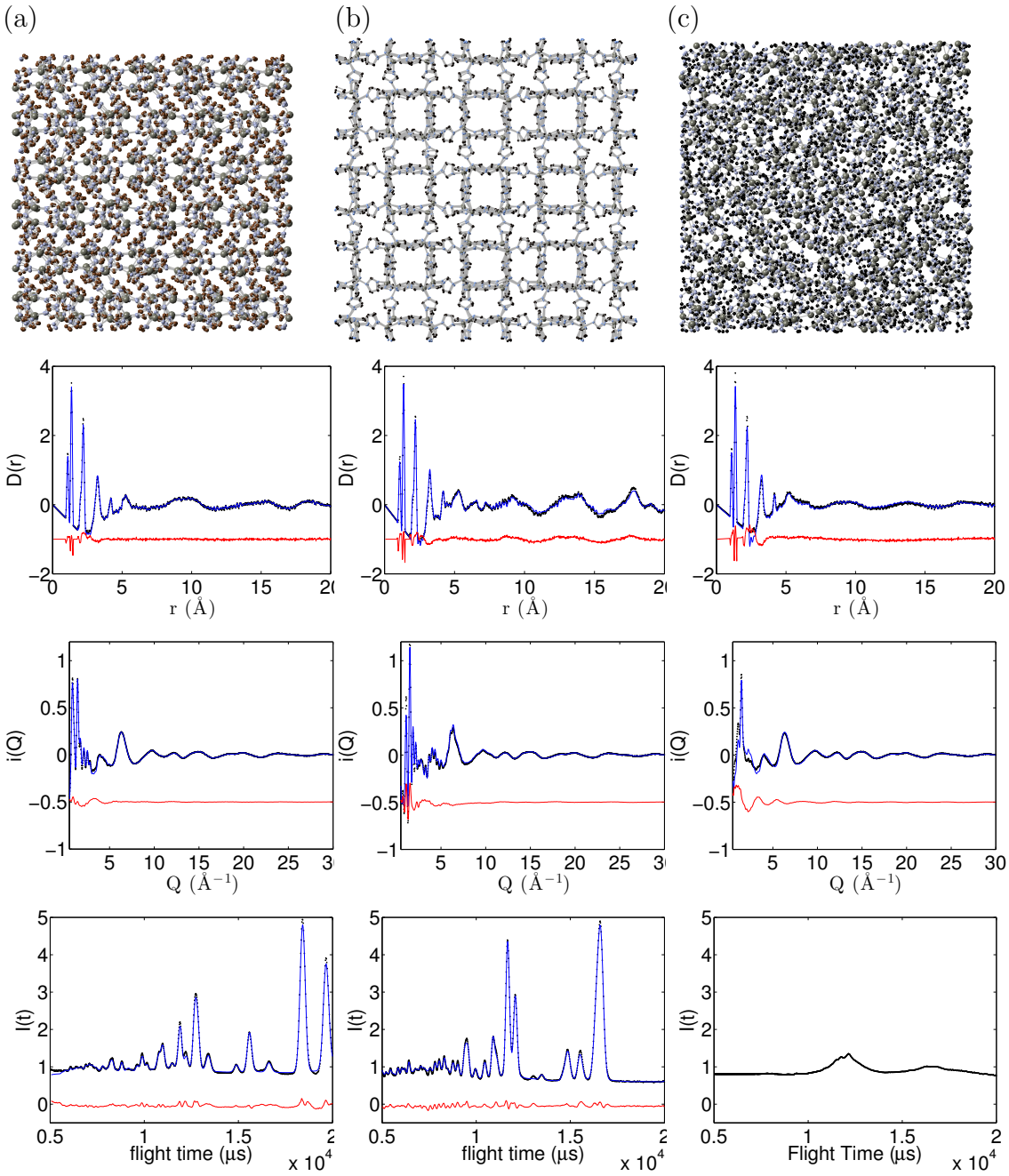

Figure 3.5: Supercells and corresponding converged fits to the $D(r)$ and $i(Q)$ functions and, where applicable, Bragg data $I(t)$ ($2\theta = 50°$), (a) ZIF-4 478 K, (b) ZIF-zni 298 K, (c) aZIF 298 K. Grey: Zn; blue: N; black: C. D atoms are omitted for clarity.Experimental data: black dots; RMC fits: blue line; difference: red line.

the tetrahedral (N–Zn–N) angle. As the stated aim of this study was to investigate the flexibility of ZIF-4 in it's different phases, the inter-tetrahedral (effective Zn–im–Zn) angle, θ in figure 3.1, the angle of the Zn from the imidazole plane (Zn–N–im), assuming the

Phase	T (K)	Zn–N (Å)		tetrahedral (°)		Zn–im–Zn θ (°)		wag ϕ (°)		planarity ω (°)	
		mean	st dev	mean	st dev	mean	st dev	mean	st dev	mean	st dev
ZIF-zni	298	2	0.1	108	12	143	12	12	19	0	23
	406	2	0.1	109	12	148	8	11	14	0	21
	540	2	0.1	109	13	146	10	10	13	0	21
	673	2	0.1	109	12	144	11	11	14	0	23
ZIF-4	478	2	0.2	107	19	132	15	19	14	-1	27
aZIF	298	2	0.1	104	24	119	23	20	16	0	47
	573	2	0.1	104	25	116	24	20	18	1	47

Table 3.3: Mean and standard deviations of the five flexibility parameters for each of the three phases, in each case averaged over six RMC refinements.

imidazole rings to be planar, ϕ in figure 3.1, and the Zn wag angle (Zn–N–N), ω in figure 3.1, were also calculated. The code written by the author to produce these bond lengths and angles is given in Appendix C.

3.6 Results and Discussion

The flexibility of the network was characterised in terms of five parameters representing three distinct types of distortion. First, the rigidity of the ZnN_4 tetrahedra was measured by considering the Zn–N bond length and N–Zn–N bond angle, analogues respectively of the Si–O bond length and O–Si–O angle in silicates. Second, the angle θ between the tetrahedra was considered – that is, between the extended N–Zn bonds associated with a single imidazolate ligand, illustrated in figure 3.1, analogous to the Si–O–Si angle in silicates. Finally, the flexibility of the linkages between the Zn–N bond and the imidazolate ligands was examined; this form of flexibility has no analogue in silicate networks. This form of flexibility can be described by the movement of the Zn^{2+} ion both in and out of the plane of the imidazolate ligand. The first, in plane, 'wag' motion is here denoted by ϕ and the second, out of plane, 'angle from planarity' by ω. Specifically, we define ϕ to be the angle between the Zn–N bond and the plane perpendicular to the ring that contains the intramolecular N$\cdots$N vector, and ω to be the angle of the Zn–N bond from the imidazolate plane, both illustrated in figure 3.1. The mean values and standard deviations of all five of these parameters are presented in table 3.3.

If the ZnN_4 tetrahedra are modelled as rigid units, it might be expected that the three

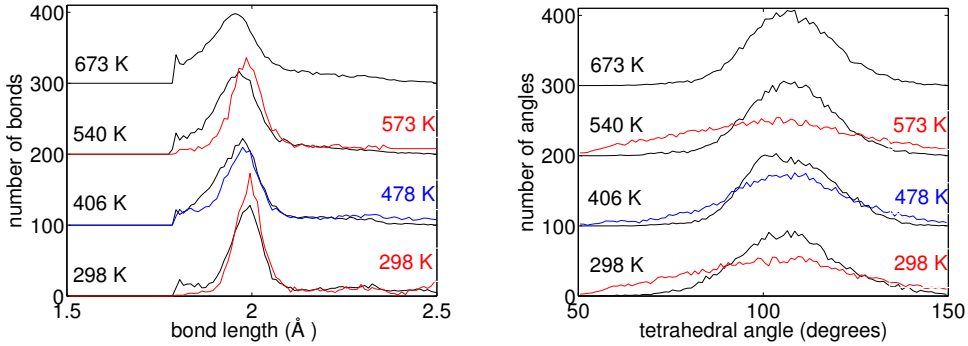

(a) (b)

Figure 3.6: Parameters of the flexibility of the ZnN_4 tetrahedra. (a) Histogram of the Zn–N bond length, (b) Histogram of the N–Zn–N angle. ZIF-zni: black; ZIF-4: blue; aZIF: red.

phases should display similar (identical to within atomic thermal motion) distributions of the Zn–N bond lengths and N–Zn–N bond angles, but differ substantially in their inter-tetrahedral angles θ. This prediction is broadly borne out by the refined parameter distributions. Certainly, the Zn–N distance is more or less constant in both mean and variance for all temperatures and phases, shown in figure 3.6(a), as indeed can be seen from the corresponding peak in the experimental PDFs in figure 3.4.

The N–Zn–N angle distributions, too, are clustered around the ideal tetrahedral angle of 109.47°, shown in figure 3.6(b). However, there is a wider spread of tetrahedral N–Zn–N angles in the amorphous phase than in the crystalline phases. The latter show a spread of around ±15°, compared to a spread of ±23° for the amorphous phase. It is useful to compare these spreads with the distribution of the corresponding O–Si–O angles in amorphous silica, SiO_2, obtained from a previous RMC study of this material [69]; the initial configurations from that study were used as the basis for the development of the initial configuration of aZIF. There it was found that the spread of angles was around ±5°. Thus it is clear that the ZnN_4 tetrahedra retain their structural integrity across the different phases, but that ZnN_4 tetrahedra in any of the ZIF structures are less rigid than the corresponding tetrahedra in amorphous silica.

As anticipated, the distributions of the Zn–im–Zn angle θ in the three phases are distinct in both mean and variance, shown in figure 3.7. aZIF has the lowest mean but a very broad spread of values; ZIF-4 has a larger mean and smaller spread; and ZIF-zni

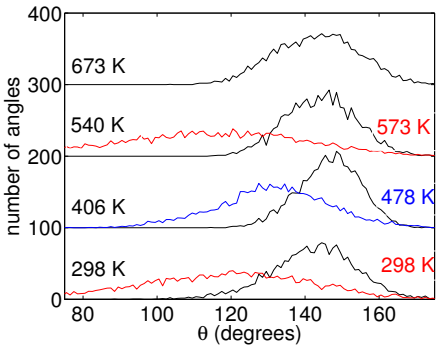

Figure 3.7: Histogram of the inter-tetrahedral Zn–im–Zn angle θ. ZIF-zni: black; ZIF-4: blue; aZIF: red.

has the largest mean angle and the sharpest distribution. Thus it is clear that there is a large increase in the inter-tetrahedral flexibility of the framework within aZIF and ZIF-4. Furthermore, the mean θ in ZIF-zni coincides with the Si-O-Si angle of $145 \pm 14°$ in silica [69], with a similar spread of $9 - 11°$ depending on temperature.

Key to the inter-tetrahedral flexibility of the ZIF structures is the orientational flexibility of the linkage between the Zn–N bond and the imidazolate ligand, which as noted above has no parallel in the silica framework. The distribution of the in-plane wag angles ϕ for the three phases is shown in figure 3.8(a). In ZIF-zni there is an additional shoulder corresponding to a peak at about $\phi = -15°$, indicating that the Zn atom is below the horizontal plane in figure 3.1. This is equivalent to the imidazole ring twisting sideways so that the Zn$\cdots$Zn vector no longer lies in the plane of the ring. This twisted configuration is known from the crystal structure of ZIF-zni; indeed, it is an inevitable consequence of the increased density of this phase compared to the others, without any accompanying decrease in individual bond lengths, as shown in figure 3.6(a).

The distribution of the out-of-plane planarity angles ω for the three phases is shown in figure 3.8(b). The distributions are centred on an average of 0°, with a spread of $\pm 30°$ for the two crystalline phases, but with a much broader distribution in aZIF. The latter distribution spans an angle range of around $\pm 60°$, which suggests that this is a highly activated mode of flexibility in aZIF. Comparing these angle distributions shows clearly that the greatest inter-tetrahedral flexibility is in the planarity angle ω, particularly in aZIF. There is nevertheless a greater degree of flexibility in the wag angle ϕ in both ZIF-4

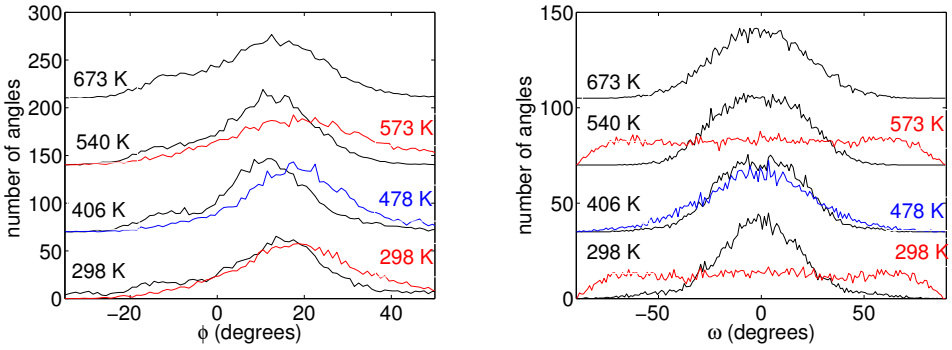

(a) (b)

Figure 3.8: Parameters of the flexibility in the linkage between the Zn–N bond and the imidazolate ligand. (a) Histogram of the 'wag' angle ϕ, (b) Histogram of the 'planarity' angle ω. ZIF-zni: black; ZIF-4: blue; aZIF: red.

and aZIF than there is in ZIF-zni.

The distinction between the orientation of the imidazole rings in the three phases is further apparent in a scatterplot of ϕ against ω, shown in figure 3.9. This shows that the shoulder at $\phi = -15°$ in ZIF-zni, as seen in figure 3.8(a), is centred on $\omega = 0$, indicating that it corresponds roughly to rotation of the imidazole ring within its own plane. More generally, in both ZIF4 and ZIF-zni the orientation of the imidazole ring appears to fluctuate about the known crystallographic average at $\omega = 0$, $\phi \approx 15°$. In aZIF, on the other hand, although the configurations are far more evenly distributed over the ω-ϕ plane, there is a conspicuous gap around $\omega = 0$ at negative ϕ, suggesting that in this phase the dominant mode of flexibility involves the imidazole ring buckling out of its plane.

3.7 Conclusions

The study reported in this chapter has compared the magnitude of the localised structural fluctuations in three phases of zeolitic imidazolate as deduced from RMC analysis of neutron total scattering. Although the ZnN_4 tetrahedra are less rigid than SiO_4 tetrahedra [69], the principal mode of flexibility involves the movement of the zinc atom out of the plane of the imidazole ring or analogously the twisting of the imidazole ring out of its

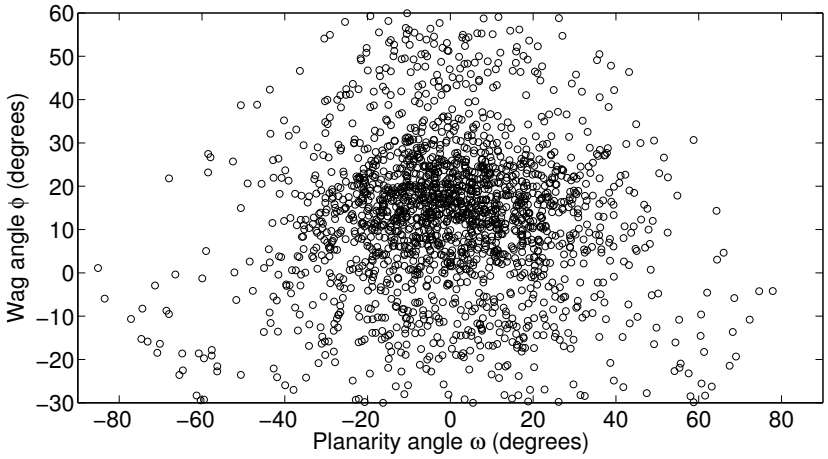

(a)

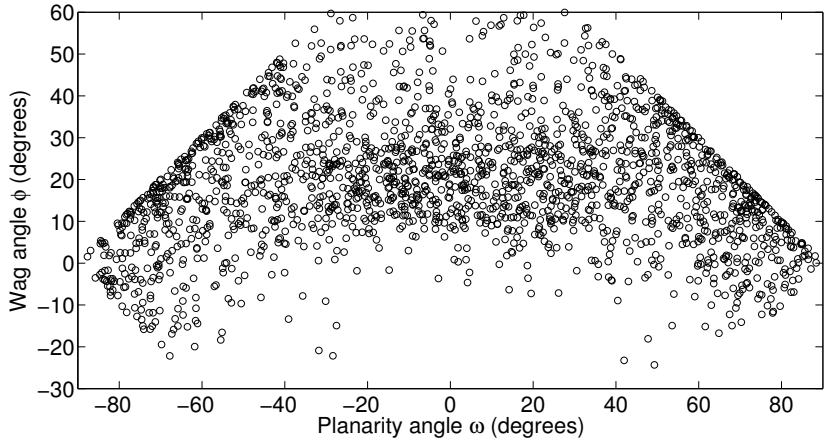

(b)

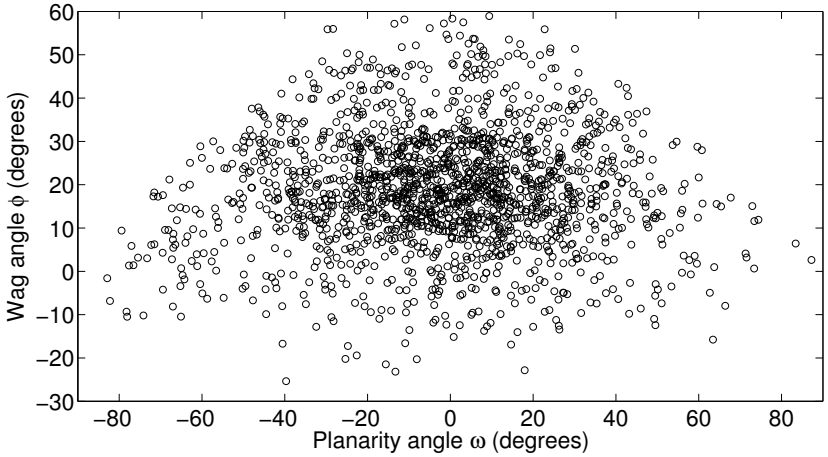

(c)

Figure 3.9: Scatter graph of the wag angle ϕ plotted against the planarity angle ω for (a) ZIF-zni at 298 K, (b) aZIF at 298 K and (c) ZIF-4 at 478 K. Note that the phase space is restricted by the geometric relationship $\sin^2\omega + \sin^2\phi \leq 1$ shown in figure 3.1 so that the corners of each diagram are geometrically inaccessible.

original plane. The molecular motion that gives rise to this mode of flexibility is due to the flexible linkages between the metal and organic structures in this framework.

Chapter 4

Para-Terphenyl

4.1 Introduction

The linear polyphenyls are an interesting class of materials with respect to their solid-solid phase transitions. The individual molecules in these materials consist of linear chains of phenyl rings linked by C–C sigma bonds and it is the torsional flexibility of these inter-ring bonds that result in the phase transitions. Biphenyl, *para*-terphenyl and *para*-quaterphenyl crystals are all monoclinic at room temperature, with two molecules per unit cell [70]. These molecules are on average flat, the phenyl rings coplanar, but show unusually large thermal motion about the long molecular axis corresponding to rotation of the phenyl rings about the mean molecular plane, interpreted as rotational disorder of the phenyl rings. The phase transitions in polyphenyls are associated with the 'freezing' in of these rotations at low-temperatures. These rotations are caused by two competing interactions in a linear polyphenyl molecule; the steric clash of the *ortho*-hydrogens, as illustrated by the dashed line in figure 4.1, which prefers adjacent rings to be non-coplanar, and the conjugation of π orbitals between rings, which prefers a coplanar arrangement. It is a balance between these two competing interactions that gives rise to these ring rotations [71].

Para-terphenyl (PTP), $C_{18}H_{14}$, consists of three *para* substituted phenyl rings as illustrated in figure 4.1, and undergoes a structural phase transition at 178 K. The high-temperature phase is monoclinic ($P2_1/a$, $a = 8.106(4)$ Å, $b = 5.613(2)$ Å, $c = 13.613(6)$ Å and $\beta = 92.04(4)^\circ$), with two seemingly coplanar molecules per unit cell [72, 73]. In the low-temperature phase the central ring of each molecule is twisted with respect to the outer rings, the direction of twist alternating along both a and b, giving a low-temperature structure with a triclinic unit cell doubled along a and b ($P\bar{1}$, $a = 16.01(3)$ Å, $b = 11.09(3)$ Å, $c = 13.53(3)$ Å and $\beta = 92.0(2)^\circ$), with four twisted molecules per unit cell [74], as illustrated in figure 4.2.

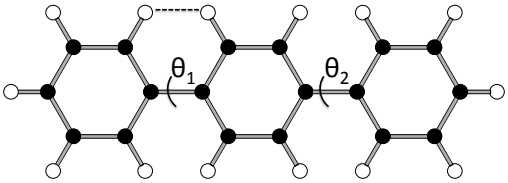

Figure 4.1: Diagram of a PTP molecule showing the steric clash (dashed line) between *ortho*-hydrogens preventing the energetically favourable coplanar, 'flat', configuration and the between ring torsion angles θ_1 and θ_2. C: black; H: white.

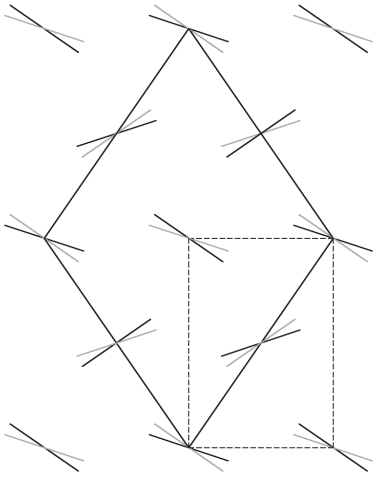

Figure 4.2: The unit cells of the high- and low-temperature phases of PTP, viewed along the c axis. PTP molecules shown schematically as two lines representing the central and outer rings. High-temperature monoclinic unit cell: dashed line; low-temperature triclinic unit cell: solid line.

The local structure of PTP molecules that result in the disordered, seemingly coplanar, structure in the high-temperature phase can be interpreted in two ways. It can be viewed as a 50:50 superposition of an arrangement of PTP molecules with static twists of both directions [75]. Alternately this high-temperature phase may be given by an arrangement of PTP molecules that, instead of existing in a disordered arrangement with either a positive or negative static twist, are free to rotate between the two states of twist in a

dynamically disordered phase. These two possible local structures of PTP in the high-temperate phase would each result in a slightly different nature to the phase transition.

A disordered arrangement of PTP molecules in the high-temperature phase with a static twist between the constituent phenyl rings would result in a phase transition at the order-disorder limit. Whereas an arrangement of PTP molecules whose phenyl rings are dynamically disordered between the two static twists would result in a phase transition at the displacive limit [79]. Phase transitions in real materials will exist somewhere on the continuum between these two limits depending on the relative strength of the different interactions present.

The structure of PTP has been extensively studied, with many attempts to produce structural models that accurately model both the high- and low-temperature phases as well as the nature of the phase transition [76–78]. However previous models have often assumed structural details, such as the bi-modal distribution of torsion angles [75], and have been tuned to meet these conditions. In the presented refinements it is attempted not to impose any structural assumptions, instead, as far as possible, allowing the position of each atom to be refined individually according to a series of experimental data sets. Therefore, in this chapter the results of a neutron total scattering and subsequent RMC refinement of the high- and low-temperature phases of PTP are presented.

4.2 Experimental

Neutron total scattering data were collected at various temperatures on the GEM diffractometer, as described in section 2.2.3. Perdeuterated PTP was purchased from Qmx Laboratories with a deuteration ratio of 98%. Data suitable for RMC analysis were obtained at temperatures of 10, 65, 125, 150, 165, 185, 250 and 290 K.

4.3 Data Processing

The background was subtracted and the data normalised using the program Gudrun [35] as described in section 2.3.1. A sample of the PDFs produced by Gudrun are shown in

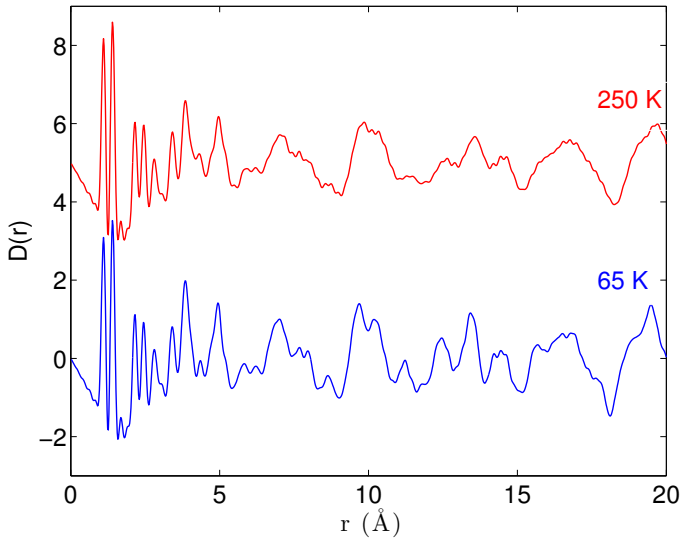

Figure 4.3: PDFs, $D(r)$, of the high- and low-temperature phases of PTP. The two phases have practically identical local structure below about 5 Å, but show some systematic deviations in the longer-range correlations above this radius. 65 K: blue; 250 K: red.

figure 4.3 and the key parameters used in Gudrun to produce them are given in table 4.1.

temperatures (K)	tweak factor	Q_{max} (Å^{-1})	Q_{T} (Å^{-1})	Lorch parameters	
				Δ (Å)	β
10	2.76288	30	3	0	NA
65	2.96659	30	3	0	NA
125	2.88886	30	3	0	NA
150	2.98121	30	3	0	NA
165	2.94822	30	3	0	NA
185	3.04305	30	3	0	NA
250	2.87506	30	3	0	NA
290	3.02695	30	3	0	NA

Table 4.1: Gudrun parameters used to produce diffuse scattering functions, $i(Q)$ and $D(r)$.

The Bragg diffraction profile was also separately extracted, and Rietveld refinement performed using GSAS [38] and EXPGUI [39] in order to extract lattice parameters and to obtain the peak shape, background and scale parameters for use in the RMC refinements. The crystal structure of PTP given in J. L. Baudou *et al.* [74], following substitution of the hydrogens for deuteriums, was used as the starting model for these refinements. In

these Rietveld refinements constraints were placed on the isotropic atomic displacement parameters of all atoms such that all carbon atoms had the same value and all deuterium atoms had the same value. As the within-ring correlations are of no interest in the presented work, the phenyl rings were treated as rigid bodies during the refinement with only their centre of mass and rotation angles allowed to vary. Additionally the inter-ring C–C bond distance was restrained to 1.45 Å. Example fits, lattice parameters, cell volumes and the refinement residuals are given in Appendix A.

4.4 Reverse Monte Carlo

In the experimental PDF of both the high- and low-temperature phases of PTP there is a small peak at approximately 1.6 Å, shown in figure 4.4, between the C–C nearest neighbour peak at approximately 1.4 Å and the C–C second nearest neighbour peak at approximately 2.3 Å. As this peak at 1.6 Å is within the low-r region of the PDF that should not contain any peak overlapping, where each individual peak corresponds directly to a well defined intramolecular distance, and as neither C–C or C–D distances could account for it, it could only be due to a D–D distance. However, in the refined crystal structure of both the high- and low-temperature phases the smallest D–D distance is 2 Å.

During test RMC refinements in which this peak at 1.6 Å was considered to be real, and so left unchanged, it was fit very poorly, as shown in figure 4.4. This fitting was only achieved by distorting the PTP molecule such that some D–D distances in the refinement were reduced to 1.6 Å, which as explained above is considered unphysical. Therefore this small peak at 1.6 Å was not considered to be real and therefore a ripple in the experimental PDF caused by errors in the experimental production of a PDF, whose fitting in an RMC refinement would result in an unphysical configuration.

As described in section 2.3.1 ripples in a materials PDF are produced by the truncation of $i(Q)$ and the noise in the high-Q region of $i(Q)$, and can be reduced by changing $Q_{\max}$ and using a modified Lorch broadening function. These methods were used to reduced the size of the ripple at 1.6 Å but were found to be unable to eliminate it without causing undue degradation to other regions of the PDF. Hence the experimental PDF was set to

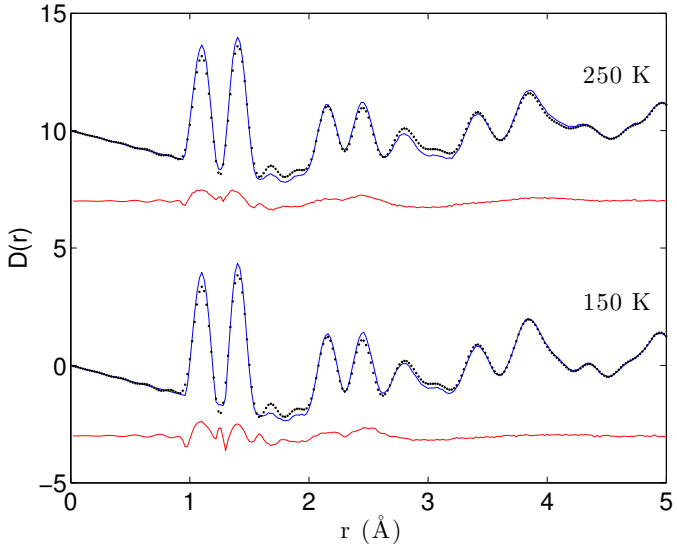

Figure 4.4: Fits to the low-r region ($r \leq 5\,\text{Å}$) of the PDF, $D(r)$, given by test RMC refinements of the high- and low-temperature phases of PTP. Experimental data: black dots; RMC fit: blue line; difference: red line.

zero in the region $1.5\,\text{Å} < r < 1.7\,\text{Å}$.

4.4.1 Initial Configurations

Initial configurations of the high- and low-temperature phases of PTP were produced for each temperature as $6 \times 9 \times 4$ and $3 \times 5 \times 4$ supercells of their refined crystal structures respectively, obtained by Rietveld refinement, using the program RMCcreate [5]. This procedure resulted in initial configurations of the high- and low-temperature phases with side length of approximately 50 Å, containing 13824 and 15360 atoms respectively.

Exact structural details and atom numbers of the initial configurations for both phases of PTP are given in Appendix B

4.4.2 Constraints and Restraints

A number of constraints, in the form of minimum distances, and restraints, in the form of molecular potentials, were applied to all of the RMC refinements of PTP and are given in tables 4.2 and 4.3. Two distance window constraints were also applied to these refinements, constraining the C–C distance to between 1.0 and 2.0 Å and the C–D distance to between 0.5 and 1.5 Å.

atom pair	distance (Å)
C C	1.00
C D	0.94
D D	1.80

Table 4.2: Minimum Distance of Approach

Potentials	Atoms	Values
$E = D[(1 - \exp(-\alpha(r_{ij} - r_0)))^2]$	C–D	$D = 2.472$ eV $\alpha = 2.55$ Å^{-1} $r_0 = 1.1$ Å
	C–C	$D = 3.148$ eV $\alpha = 2.55$ Å^{-1} $r_0 = 1.4$ Å
$E = \frac{K}{2}(\cos(\theta_{ijk}) - \cos(\theta_0))^2$	$\widehat{\text{CCC}}$	$K = 9.478$ eV $\theta_0 = 120.0°$
	$\widehat{\text{CCD}}$	$K = 6.117$ eV $\theta_0 = 120.0°$
$E = P\omega$	CCCCCC	$P = 5000.0$

Table 4.3: Summary of the potentials used in the RMC refinement, bond and angle potentials are adapted from the MM3 potentials [42] as described in the RMCProfile manual [43].

4.5 Analysis

In these RMC refinements it was found that the value of the function χ^2_{RMC} decreased towards a converged minimum value after approximately 20 million generated atomic moves, over 1300 moves per atom. At this point the refinements were considered to have reached an equilibrium and so RMC was terminated. For each of these two phases six independent RMC refinements were performed to give improved statistical accuracy to extracted histograms, averages and standard deviations. Examples of the final fits to the $D(r)$, $i(Q)$ functions and Bragg data are shown in figure 4.5.

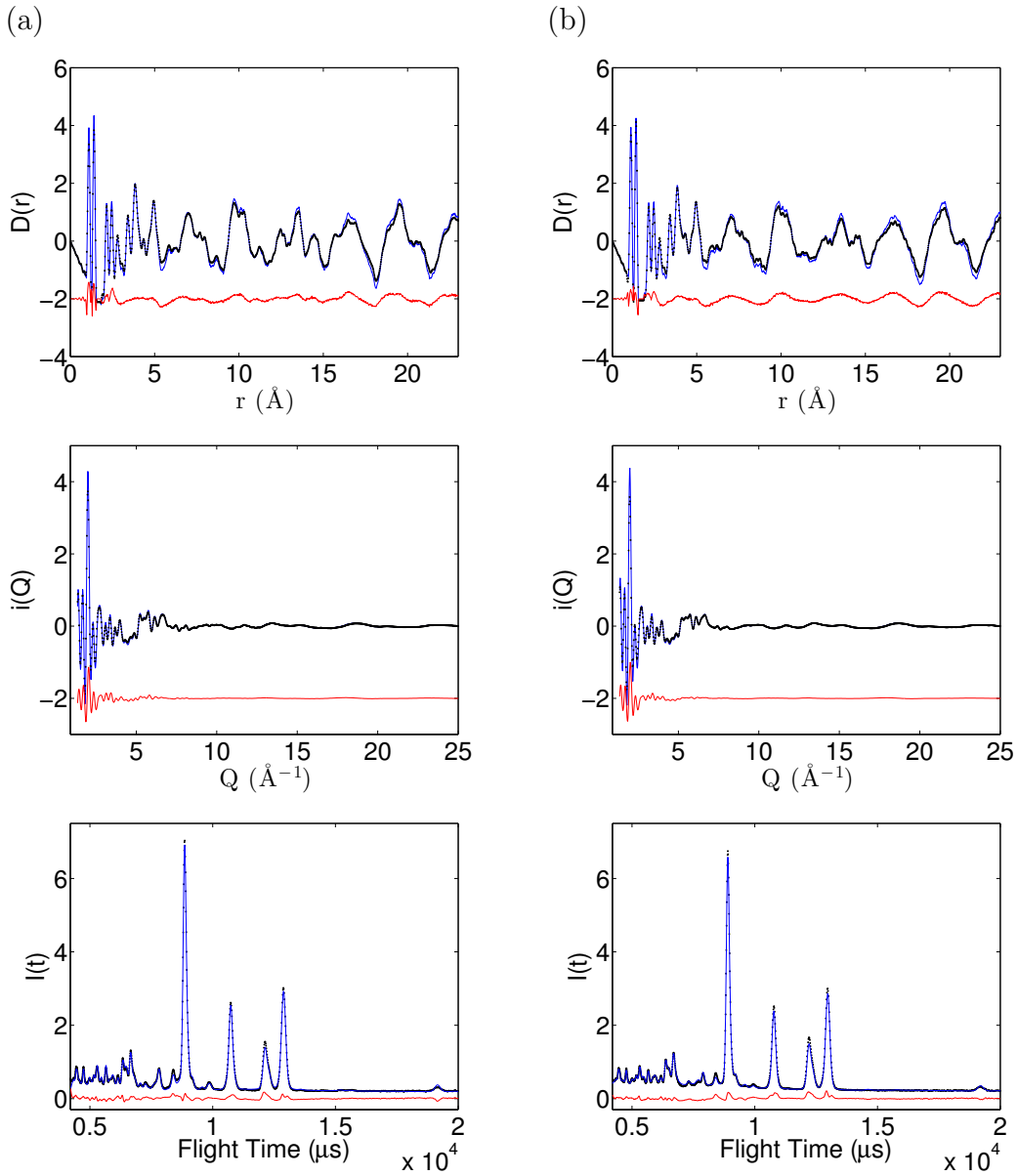

Figure 4.5: Converged fits to the $D(r)$, $i(Q)$ and $I(t)$ ($2\theta = 35°$) functions, (a) PTP 150 K, (b) PTP 250 K. Experimental data: black dots; RMC fits: blue line; difference: red line.

The basic analysis described in section 2.5 calculates all the bond distances and basic three atom angles. As it is the torsional flexibility of the connectivity between the phenyl rings that result in the phase transition, the torsion angles between the rings were calculated, θ_1 and θ_2 in figure 4.1. As well as these raw torsion angles, the crystal structure was given with phenyl rings highlighted according to the sign of their respective torsion angle. The code written by the author to produce these bond lengths, angles and highlighted crystal structures is given in Appendix C.

T (K)	C–D (Å)		$\widehat{\text{CCD}}$(°)		C–C(Å)		$\widehat{\text{CCC}}$(°)		ω (10^{-4}Å^2)	
	mean	st dev	mean	st dev	mean	st dev	mean	st dev	mean	st dev
10	1.1	0.05	119	1.8	1.4	0.04	120	1.5	3.6	2.9
65	1.1	0.05	119	1.8	1.4	0.04	120	1.5	4.6	3.8
125	1.1	0.05	119	1.8	1.4	0.04	120	1.4	3.6	2.8
150	1.1	0.06	119	1.8	1.4	0.05	120	1.4	4.1	3.3
165	1.1	0.06	119	1.8	1.4	0.05	120	1.5	4.6	3.8
185	1.1	0.06	119	2.0	1.4	0.05	120	1.5	5.2	4.2
250	1.1	0.06	119	2.2	1.4	0.05	120	1.7	7.0	5.9
290	1.1	0.06	119	2.2	1.4	0.05	120	1.8	8.1	6.7

Table 4.4: Mean and standard deviations of the five within ring structural parameters for all refined temperatures phases, in each case averaged over six RMC refinements.

4.6 Results and Discussion

The mean values and standard deviations of the five restrained parameters relating to the structure of individual phenyl rings, the C–C and C–D bond lengths, the $\widehat{\text{CCC}}$ and $\widehat{\text{CCD}}$ angles as well as the deviation from planarity, are given in table 4.4. The phenyl rings of a PTP molecule are rigid units, as can be seen from the very similar low-r peaks in the experimental PDFs of both phases, shown in figure 4.3. Therefore both the low- and high-temperature phases should display similar distributions of all bond lengths and angles in the refined structure (identical to within atomic thermal motion). This is broadly borne out in the refined parameter distributions; the bond lengths and angles are more or less constant in both mean and standard deviation across both refined phases. The reproduction of this experimentally observed local structure in the refined structure, with little variation in table 4.4, shows the utility of the potentials applied to the presented refinements.

The histogram of torsion angles given in figure 4.6 shows, in the low-temperature phase, a bimodal distribution of torsion angles peaking at approximately $\pm 20°$ with a low frequency at 0°, both of which are consistent with previous work [73, 75]. This distribution of torsion angles indicates a statically twisted configuration in the low-temperature phase. A phase in which the central phenyl ring in half the PTP molecules are twisted in one direction with respect to the plane containing the two outer phenyl rings and the opposite direction in the other half of the PTP molecules. The direction of this twist between the

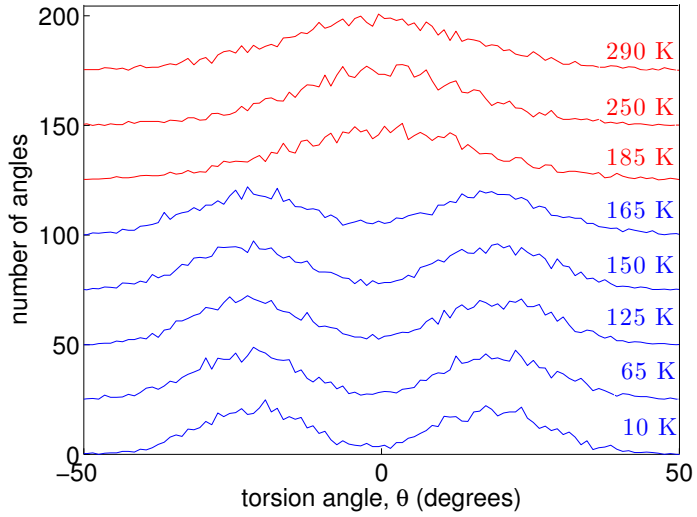

Figure 4.6: Histogram of torsion angles θ_1 and θ_2. Low-temperature phase: blue; high-temperature phase: red.

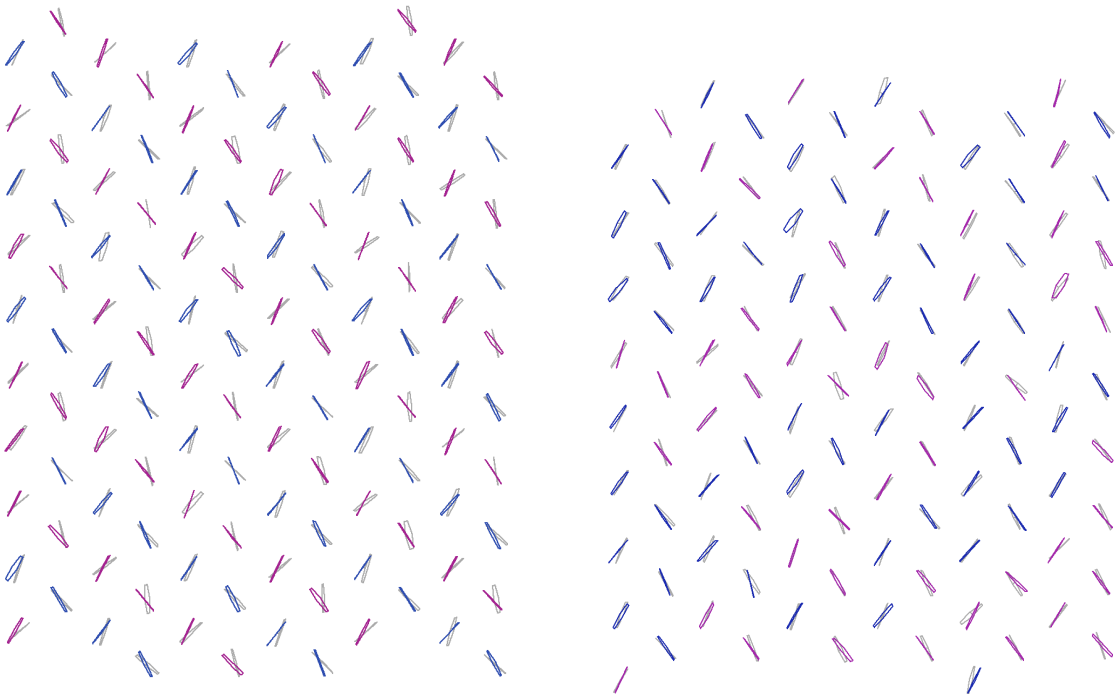

Figure 4.7: Diagrams showing the ordering of torsion angles in a single plane of PTP molecules within a PTP crystal, viewed along the c axis. (a) in the low-temperature phase and (b) in the high-temperature phase. Red ring: negative torsion angle; blue ring: positive torsion angle.

central and two outer rings alternates along the a and b axes as shown in the single plane of PTP molecules shown in figure 4.7(a).

However, in the high-temperature phase a unimodal distribution of torsion angles centred on 0° with a greater standard deviation is given, shown in figure 4.6. This suggests that the central phenyl ring within the PTP molecules is now relatively free to rotate. The central ring is no longer locked in to a twisted configuration with a torsion angle of approximately ±20°, as they are in the low-temperature phase, but are rapidly flipping with no apparent ordering in the direction of twist between neighbouring molecules, shown in figure 4.7(b). Indeed in the high-temperature phase many PTP molecules appear to exist in a 'flat' configuration, shown by the high-frequency at 0° in figure 4.6.

This 'flat' arrangement is energetically favourable with regard to the between ring π conjugation but does not exist due to the steric clash of the *ortho*-deuteriums shown in figure 4.1. However, the presented refinements suggests that a possibly increased orientational flexibility of the deuterium atoms allows the deuteriums to move so as to alleviate this steric clash. Thereby allowing the rotation of the central phenyl ring and the energetically favourable 'flat' configuration to become available to some PTP molecules in the high-temperature phase.

The high-temperature configurations reported in this study, the unimodal torsion angle distribution that they give and the dynamically disordered phase this suggests, are not entirely consistent with the models of the high-temperature phase proposed by some previous authors. Nor was the diffuse scattering calculated from my configuration, done with code written by A. E. Phillips using equation 1.1, found to match the experimental single crystal diffuse scattering presented by D. J. Goossens *et al.* [75]. Therefore, as the models of previous authors used potentials tuned to give a bimodal distribution of torsion angles, further refinements of the high-temperature phase were performed using a randomly twisted initial configuration with a bimodal distribution of torsion angles.

The initial configurations used for these further refinements, instead of having a unimodal distribution of torsion angles, have a bimodal distribution of torsion angles of value ±20°, shown in figure 4.8(a). These configurations were produced by randomly twisting the central ring of each PTP molecule by ±20° out of the mean molecular plane. These

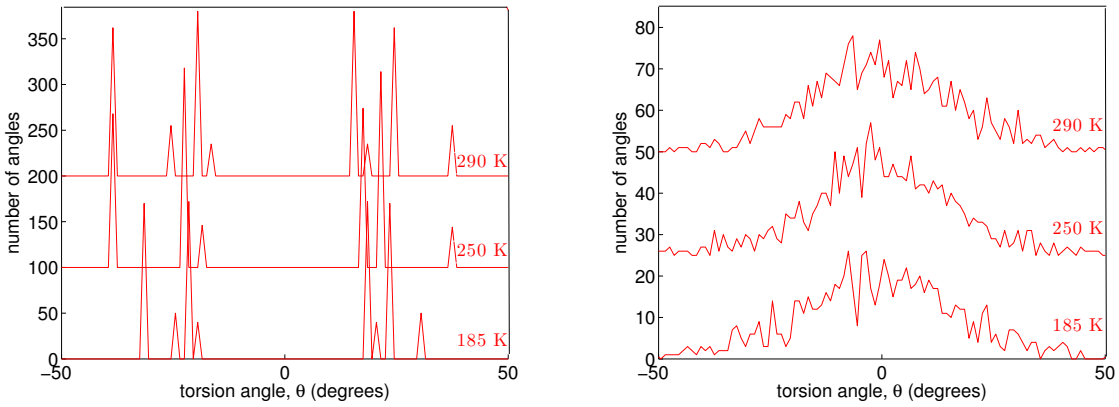

Figure 4.8: Histogram of torsion angles θ_1 and θ_2 in the high-temperature phase using a randomly twisted initial configuration. (a) In the initial configuration and (b) in the refined configuration, in this case torsion angles have only been calculated from one RMC configuration, not as an average of six - hence the higher degree of noise in the data.

initial configurations are similar to those used for refinements of the low-temperature phase but have a random distribution of twists such as that shown by figure 4.7(b), not the ordered structure with twists that alternate along the a and b axes as in the low-temperature phase, shown in figure 4.7(a). Refinements using these randomly twisted initial configurations with a bimodal distribution of torsion angles reproduced a unimodal distribution of torsion angles upon refinement, shown in figure 4.8. This suggests that the rotationally disordered high-temperature phase, with phenyl rings relatively free to rotate, is a genuine configuration that exists in the high-temperature phase. The code written by the author to produce these randomly twisted initial configurations is given in Appendix C.

4.7 Conclusions

The study reported in this chapter has compared the localised structural fluctuations in the high- and low-temperature phases of PTP as deduced from RMC analysis of neutron total scattering. The unimodal distribution of torsion angles in the high-temperature phase suggests a dynamically disordered phase in which rotations of the central phenyl

ring occur, PTP molecules are no longer locked in a relatively rigid twisted state. That it is the averaging of this dynamically disordered configuration that results in the seemingly coplanar molecules in the crystal structure of the high-temperature phase, not a 50:50 superposition of an arrangement of PTP molecules with static twists of both direction. Therefore the transition between the ordered low-temperature phase and the disordered high-temperature phase is not as order-disorder in nature as previously suggested. Instead it exists some way along the continuum between order-disorder and displacive phase transitions and this continuum is on quite a flat energy surface, such that small changes in the experimental or refinement parameters can alter the observed nature of the phase transition.

Chapter 5

Ortho-Terphenyl

5.1 Introduction

A glass is a non-crystalline solid that maintains short-range order but in which long-range order is lacking. Structurally a glass can be seen as similar to an amorphous solid, such as that described in chapter 3, however, the term supercooled liquid emphasises the different origin of a glass. A material's glass transition is the process of solidification of a supercooled liquid into a non-crystalline solid; the avoidance of crystallisation on cooling with a dramatic increase in the structural relaxation time.

The glass-forming abilities of molecular materials have long been studied; however, so far there is very little understanding of the structural aspects of a molecular material that make it a good glass-former. Since the production of the first metallic glass in 1960 [80], the central question of that field has been to understand how to chemically manipulate the properties of amorphous alloys, with glass-forming ability being the most crucial of these properties [81]. More recently, the increasing importance of obtaining amorphous phases for small organic molecules in pharmaceuticals [82] and coatings in electronic applications [83] has drawn attention to the open question of the relationship between molecular structure and glass-forming ability.

Insight into addressing this question can be gleaned from studying paradigmatic glass-formers such as the molecule *ortho*-terphenyl, $C_{18}H_{14}$. OTP consists of relatively small, largely spherical, molecules that interact only weakly via nondirectional van der Waals forces and have only two intramolecular degrees of freedom [84]. Each molecule consists of three phenyl rings, a central ring *ortho* substituted by two outer rings. Due to the steric clash between these outer rings they are twisted out of the plane of the central ring. In the crystal one is twisted by approximately 42° and the other by approximately 62° in the same sense from the plane of the central ring, as illustrated in figure 5.1. The crystal structure is orthorhombic ($P2_12_12_1$, $a = 18.583(3)$ Å, $b = 6.024(1)$ Å, $c = 11.728(2)$ Å)

with four molecules per unit cell [85, 86], as illustrated in figure 5.2.

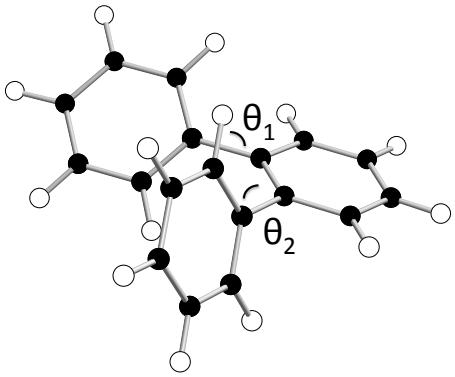

Figure 5.1: Structure of an individual OTP molecule, showing the between ring torsion angles θ_1 and θ_2. C: black; H: white.

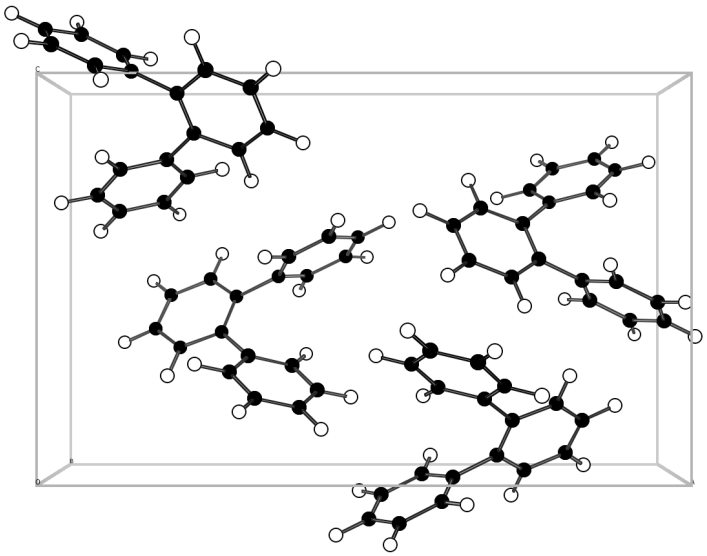

Figure 5.2: The arrangement of four OTP molecules in the crystal structure, viewed along the b axis. C: black; H: white.

Despite having been studied for over 50 years [87], this material remains a topic of active research as a prototypical 'fragile' glass, materials whose characteristic is an extremely non-Arrhenius behaviour of their viscosity [88]. OTP's physical properties

make it convenient to study: it melts at 328 K, with a glass transition at around 246 K, depending on cooling rate, and a critical cooling rate for glass formation lower than 0.1 K min^{-1} [89]. As a model system for a whole class of glasses, the dynamics of OTP across its glass transition have been the subject of extensive study by a range of methods including neutron spectroscopy [90]. However, the coherent structure factor has been less studied, and no PDF has yet been derived from such data. Therefore in this chapter the PDFs derived from a neutron total scattering experiment and subsequent RMC refinement of both the crystalline and glass phases of OTP are presented.

5.2 Experimental

Neutron total scattering data were collected on the GEM diffractometer, as described in section 2.2.3. Perdeuterated OTP was purchased from Qmx Laboratories with a deuteration ratio of 98%. Data suitable for RMC analysis were obtained for crystalline and two glass samples of OTP, a slow cool glass and rapid cool glass, all at temperatures of 16 K.

These glass phases were produced *in situ* using a static He exchange gas cryostat with an attached cartridge heater, by melting the powdered OTP and then cooling it at a prescribed rate. The rapid cool glass was produced at a cooling rate of approximately 20 K min^{-1} and the slow cool glass at a cooling rate of approximately 2 K min^{-1}. The cooling rate of 20 K min^{-1} was chosen as this was the fastest cooling rate achievable using a static He exchange gas cryostat. The cooling rate of 2 K min^{-1} was chosen as it is high enough compared to the critical cooling rate of less than 0.1 K min^{-1} so as to be able to guarantee the avoidance of crystal formation while being slow enough compared to 20 K min^{-1} to produce a glass with a potentially different structure and density. The avoidance of crystallisation when producing the glass samples was confirmed by the lack of Bragg peaks.

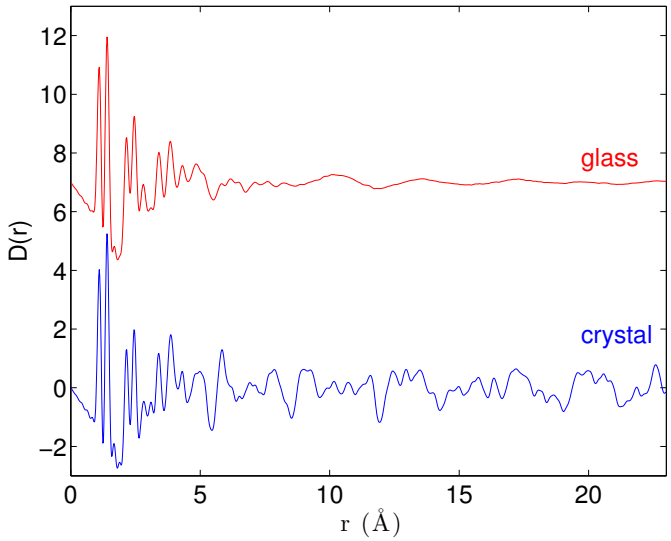

Figure 5.3: PDFs, $D(r)$, for the glass and crystalline phases of OTP. The two phases have very similar local structure below about 5 Å, but differ in the longer-range correlations above this radius; in particular, the glass, as expected, has very few high-r peaks. Crystalline, 16 K: blue; glass, 16 K: red.

5.3 Data Processing

The background was subtracted and the data normalised using the program Gudrun [35] as described in section 2.3.1. A sample of the PDFs produced by Gudrun are shown in figure 5.3 and the key parameters used in Gudrun to produce them are given in table 5.1.

phase	tweak factor	$Q_{\max}$ (Å^{-1})	Q_{T} (Å^{-1})	Lorch parameters	
				Δ (Å)	β
crystalline	2.633	30	3	0.00	NA
slow cool glass	2.415	30	3	0.04	0.5
rapid cool glass	2.449	30	3	0.04	0.5

Table 5.1: Gudrun parameters used to produce diffuse scattering functions, $i(Q)$ and $D(r)$.

The Bragg diffraction profile was also separately extracted for the crystalline phase, and Rietveld refinement performed using GSAS [38] and EXPGUI [39] in order to extract lattice parameters and to obtain the peak shape, background and scale parameters for use in the RMC refinements. The crystal structure of OTP given in G. M. Brown *et*

al. [85], following substitution of the hydrogens for deuteriums, was used as the starting model for this refinement. In this Rietveld refinement constraints were placed on the isotropic atomic displacement parameters of all atoms such that all carbon atoms had the same value and all deuterium atoms has the same value. As the within-ring correlations are of no interest in the presented work, the phenyl rings were treated as rigid bodies during the refinement with only their centre of mass and rotation angles allowed to vary. Additionally the inter-ring C–C bond distance was restrained to 1.45 Å. Example fits, cell parameters and the refinement residuals are given in Appendix A.

5.4 Reverse Monte Carlo

In the experimental PDF of both the crystalline and glass phases of OTP there is a small peak at approximately 1.6 Å, shown in figure 5.4, between the C–C nearest neighbour peak at approximately 1.4 Å and the C–C second nearest neighbour peak at approximately 2.3 Å. As this peak at 1.6 Å is within the low-r region of the PDF that should not contain any peak overlapping, where each individual peak corresponds directly to a well defined intramolecular distance, and as neither C–C or C–D distances could account for it, it could only be due to a D–D distance. However, in the refined crystal structure the smallest D–D distance is 2.3 Å.

During test RMC refinements in which this peak at 1.6 Å was considered to be real, and so left unchanged, it was fit very poorly, as shown in figure 5.4. This fitting was only achieved by distorting the OTP molecule such that some D–D distances in the refinement were reduced to 1.6 Å, which as explained above is considered unphysical. Therefore this small peak at 1.6 Å was not considered to be real and therefore a ripple in the experimental PDF caused by errors in the experimental production of a PDF, whose fitting in an RMC refinement would result in an unphysical configuration.

As described in section 2.3.1 ripples in a materials PDF are produced by the truncation of $i(Q)$ and the noise in the high-Q region of $i(Q)$, and can be reduced by changing $Q_{\max}$ and using a modified Lorch broadening function. These methods were used to reduced the size of the ripple at 1.6 Å but were found to be unable to eliminate it without causing

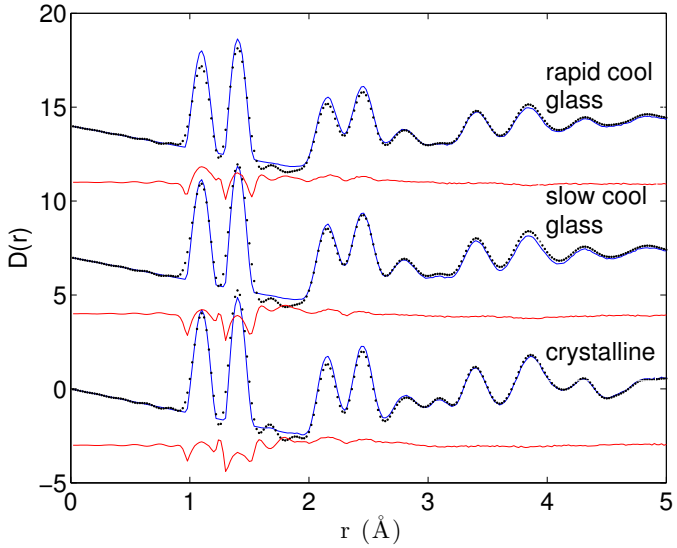

Figure 5.4: Fits to the low-r region ($r \leq 5\,\text{Å}$) of the PDF, $D(r)$, given by test RMC refinements of the three phases of OTP. Experimental data: black dots; RMC fits: blue line; difference: red line.

undue degradation to other regions of the PDF. Hence the experimental PDF was set to zero in the region $1.5\,\text{Å} < r < 2.0\,\text{Å}$.

5.4.1 Initial Configurations

Initial configurations of the crystalline phase of OTP were produced as $3 \times 9 \times 4$ supercells of its refined crystal structures, obtained by Rietveld refinement, using the program RMCcreate [5]. This procedure resulted in an initial configuration for the crystalline phase with side length of approximately 50 Å and containing 13824 atoms.

Considering our previous work on amorphous ZIF (chapter 3) it was assumed that an RMC refinement of the glass phase of OTP using the crystal structure of OTP as an initial configuration would fail to provide an accurate glass structure. Thus a new initial configuration for the glass phase was produced. This was achieved through the use of molecular dynamics (MD) simulations, produced by M. T. Dove, using the program DL_POLY_3 [91]. These MD simulations were initiated by placing 512 individual, randomly rotated, OTP molecules in a simulation box. Individually these molecules were rigid and had the atomic arrangement of an OTP molecule in the crystal structure, as determined by a Rietveld refinement. The interactions between atoms of different molecules were described

by Lennard Jones potentials [92], with no potential applied to D–D interactions. The temperature and pressure of the simulation was then increased such that an appropriate density for the glass phase of OTP was achieved.

The density of the slow cooled glass was experimentally determined by pycnometery, a technique used to measure the density of an irregularly shaped sample, such as the powdered slow cool glass. It works by utilising gas displacement and the volume-pressure relationship described by Boyle's Law. A pycnometer measures the pressure of an inert gas in two volumes. First the pressure in a sample chamber of known volume with the sample of unknown volume in it is measured, and second the pressure once the gas is also allowed to fill a reference chamber of known volume is measured. By applying equation 5.1 the volume of the sample is then determined

$$V_{\mathrm{s}} = V_{\mathrm{c}} + \frac{V_{\mathrm{r}}}{1 - \frac{P_1}{P_2}} \tag{5.1}$$

where V_s is the sample volume, V_c is the volume of the sample chamber without the sample in, V_r is the volume of the reference chamber, P_1 is the first pressure (pressure of the gas in the sample chamber with the sample in) and P_2 is the second pressure (pressure after the gas is also allowed to fill the reference chamber). Taking the average of six pycnometery measurements the density of the slow cooled glass sample was measured as 1.2308 g cm^{-3} with a standard deviation of 0.0014 g cm^{-3}.

The temperature and pressure of the MD simulations were therefore tuned to give a density approximately equal to this (1.1039 g cm^{-3}). The volume of the configuration given by MD simulation was then slightly reduced, while keeping the same size and shape of individual OTP molecules, to give a slow cooled glass initial configuration with the exact density as measured by pycnometery.

However, as it was remelted to give the slow cool glass during the neutron total scattering experiment, the density of the rapid cool glass could not be determined by pycnometery. Initially the rapid cool glass was assumed to have the same density as the slow cool glass, however test RMC refinements showed that this assumed density produced a mismatch between the levels of the experimental and calculated PDFs, shown in figure 5.5. As the rapid cool glass is formed from liquid OTP, a low density state, at a

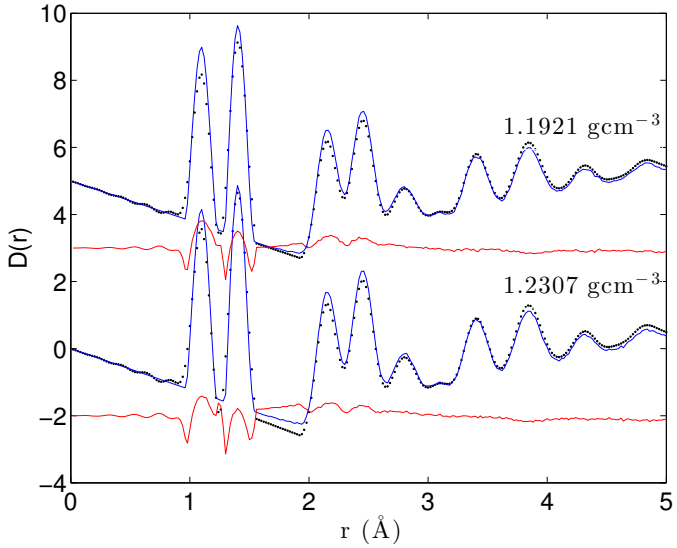

Figure 5.5: Fits to the low-r region ($r \leq 5$ Å) of the PDF, $D(r)$, given by test RMC refinements of the rapid cool OTP glass. Experimental data: black dots; RMC fits: blue line; difference: red line.

much higher cooling rate than the slow cool glass, it may be reasonable to assume that the rapid cool glass has a lower density than the slow cool glass. Therefore new, lower density, initial configurations were produced from the configuration given by MD simulation in the same manner as was done to produce the slow cool glass initial configuration. RMC test refinements showed significantly better agreement between the levels of the experimental and calculated PDFs when a density of 1.1921 g cm^{-3} was used, shown in figure 5.5, so this density was used for initial configurations of the rapid cool glass. The resulting glass configurations were cubic with side length of approximately 55 Å and contained 16384 atoms.

Exact structural details of the initial configurations of both the glass and crystalline phases are given in Appendix B.

5.4.2 Constraints and Restraints

A number of constraints, in the form of minimum distances and restraints, in the form of molecular potentials, were applied to all of the RMC refinements of OTP and are given in tables 5.2 and 5.3. Two distance window constraints were also applied to these refinements, constraining the C–C distance to between 1.0 and 2.0 Å and the C–D distance

to between 0.5 and 1.25 Å.

atom pair	distance (Å)
C C	1.00
C D	0.94
D D	2.20

Table 5.2: Minimum Distance of Approach

Potentials	Atoms	Values
$E = D(1 - \exp(-\alpha(r_{ij} - r_0)))^2]$	C–D	$D = 2.472$ eV $\alpha = 2.55$ Å^{-1} $r_0 = 1.1$ Å
	C–C	$D = 3.148$ eV $\alpha = 2.55$ Å^{-1} $r_0 = 1.4$ Å
$E = \frac{K}{2}(\cos(\theta_{ijk}) - \cos(\theta_0))^2$	$\widehat{\text{CCC}}$	$K = 9.478$ eV $\theta_0 = 120.0°$
	$\widehat{\text{CCD}}$	$K = 6.117$ eV $\theta_0 = 120.0°$
$E = P\omega$	CCCCCC	$P = 5000.0$

Table 5.3: Summary of the potentials used in the RMC refinement, bond and angle potentials are adapted from the MM3 potentials [42] as described in the RMCProfile manual [43].

5.5 Analysis

In these RMC refinements it was found that the value of the function χ^2_{RMC} decreased towards a converged value after approximately 40 million generated atomic moves, over 3000 moves per atom. For each of the three phases, crystalline, slow and rapid cool glass, six independent RMC refinements were performed to give improved statistical accuracy to extracted histograms, averages and standard deviations. Examples of the final fits to the $D(r)$, $i(Q)$ functions and, where applicable, Bragg data are shown in figure 5.6.

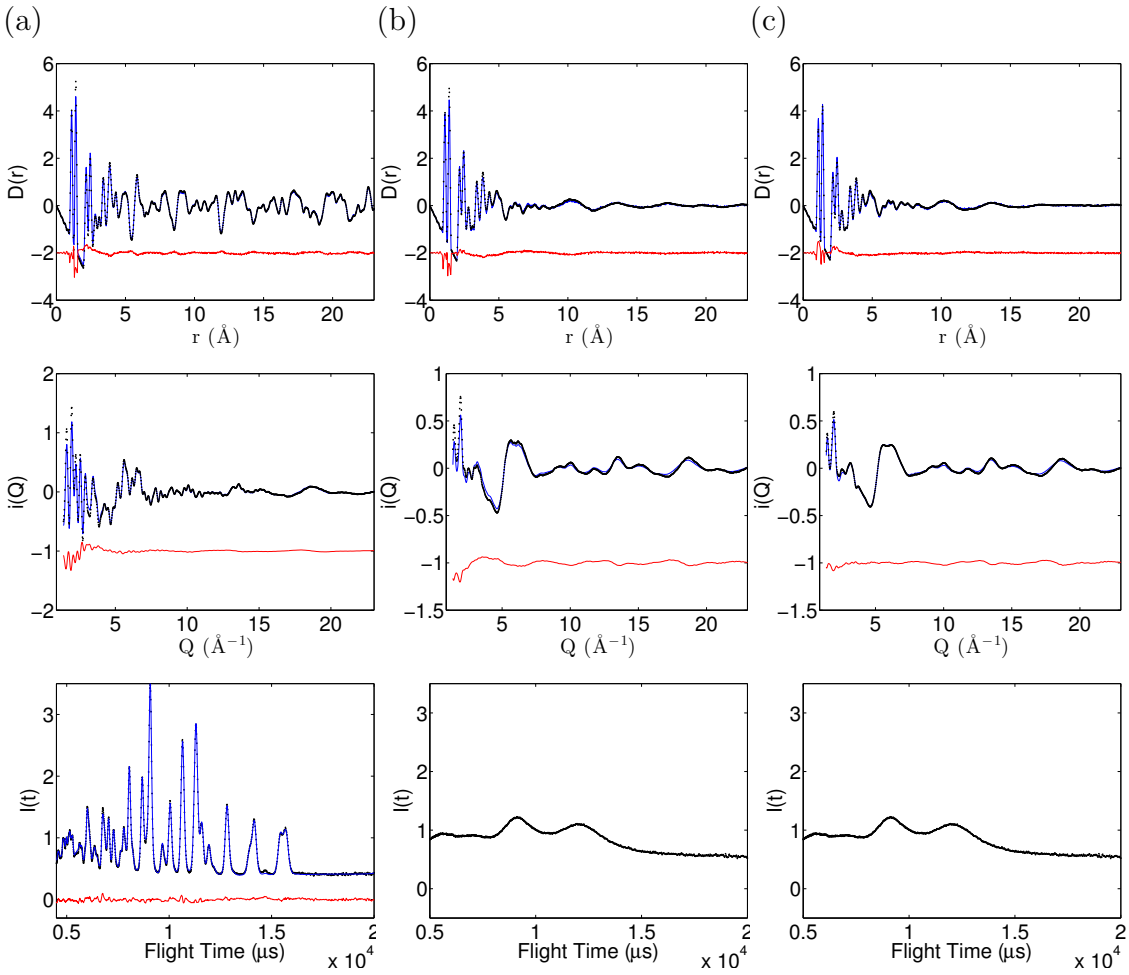

Figure 5.6: Converged fits to the $D(r)$ and $i(Q)$ functions and, where applicable, the Bragg $I(t)$ ($2\theta = 35°$) function, (a) crystalline OTP, (b) slow cooled glass OTP, (c) rapid cool glass OTP. Experimental data: black dots; RMC fits: blue line; difference: red line.

The basic analysis described in section 2.5 calculates all the bond distances and basic three atom angles. To investigate the torsional flexibility of the connectivity between the phenyl rings, the torsion angles between these rings were calculated, θ_1 and θ_2 in figure 5.1. To investigate the arrangement of OTP molecules in the crystal or glass, the distances between and orientation of these molecules were calculated. The distances between OTP molecules was investigated by calculating a molecular distribution function reflecting the distances between the centre of mass of each OTP molecule, their orientation was investigated by calculating the vector between this centre of mass and the centre of mass of the two *mono*-substituted rings. This vector was calculated for all molecules and then collapsed onto a single origin to give a real-space stereographic projection of the

molecular orientations within an OTP crystal or glass. The codes written by the author to produce these bond lengths, angles, molecular distribution functions and orientation vectors are given in Appendix C.

5.6 Results and Discussion

Phase	C–D (Å)		$\widehat{\text{CCD}}(^\circ)$		C–C(Å)		$\widehat{\text{CCC}}(^\circ)$		ω (10^{-4}Å^2)	
	mean	st dev	mean	st dev	mean	st dev	mean	st dev	mean	st dev
crystalline	1.1	0.051	119	1.9	1.4	0.044	120	1.2	7.7	6.3
slow cool glass	1.1	0.053	119	1.8	1.4	0.078	120	1.1	7.6	6.2
rapid cool glass	1.1	0.056	119	1.8	1.4	0.079	120	1.1	7.3	6.1

Table 5.4: Mean and standard deviations of the five within ring structural parameters for all refined phases, in each case averaged over six RMC refinements.

The mean values and standard deviations of the five restrained parameters relating to the structure of individual phenyl rings, the C–C and C–D bond lengths, the $\widehat{\text{CCC}}$ and $\widehat{\text{CCD}}$ angles as well as the deviation from planarity, are given in table 5.4. The phenyl rings of an OTP molecule are rigid units, as can be seen from the very similar low-r peaks in the experimental PDFs of both phases, shown in figure 5.3. Therefore both the low- and high-temperature phases should display similar distributions of all bond lengths and angles in the refined structure (identical to within atomic thermal motion). This is broadly borne out in the refined parameter distributions; the bond lengths and angles are more or less constant in both mean and standard deviation across both refined phases. The reproduction of this experimentally observed local structure in the refined structure, with little variation in table 5.4, shows the utility of the potentials applied to the presented refinements.

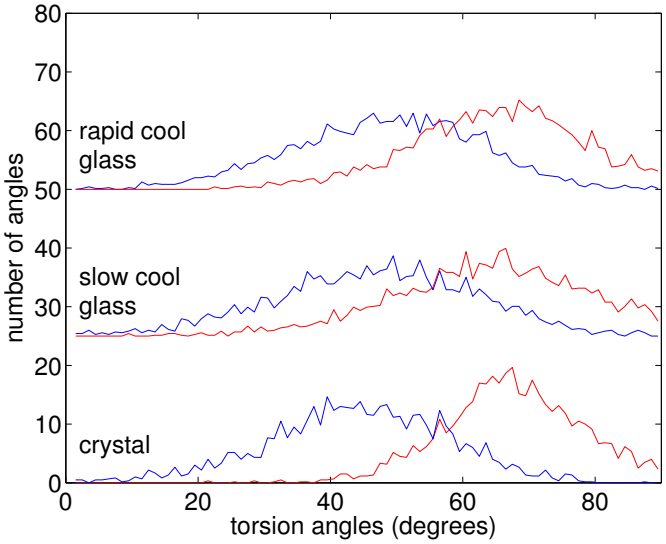

Figure 5.7: Histogram of torsion angles θ_1 and θ_2. θ_1; blue line, θ_2; red line.

Phase	$\theta_1(^\circ)$		$\theta_2(^\circ)$	
	mean	st dev	mean	st dev
crystalline	44.4	13.5	67.6	10.3
slow cool glass	46.8	15.4	63.4	14.4
rapid cool glass	48.4	14.2	64.7	12.8

Table 5.5: Mean and standard deviations of the two torsion angles in all three phases, in each case averaged over six RMC refinements.

A histogram of the two torsion angles, θ_1 and θ_2, for the crystalline and glass phases is shown in figure 5.7 with the corresponding mean values and standard deviations given in table 5.5. There are only small differences seen in the mean values of these angles between the crystal and glass phases showing that these internal degrees of freedom seem to play no role in the glass transition of OTP [84]. However there is a systematic increase in the standard deviation of both θ_1 and θ_2 between the crystal and glass phase showing that, despite these angles having similar mean values between the two phases, there is a slightly greater torsional flexibility in the glass phase.

The distribution function of OTP molecules in the glass and crystalline phases is shown in figure 5.8. These distribution functions are analogues to the PDF; however instead of a

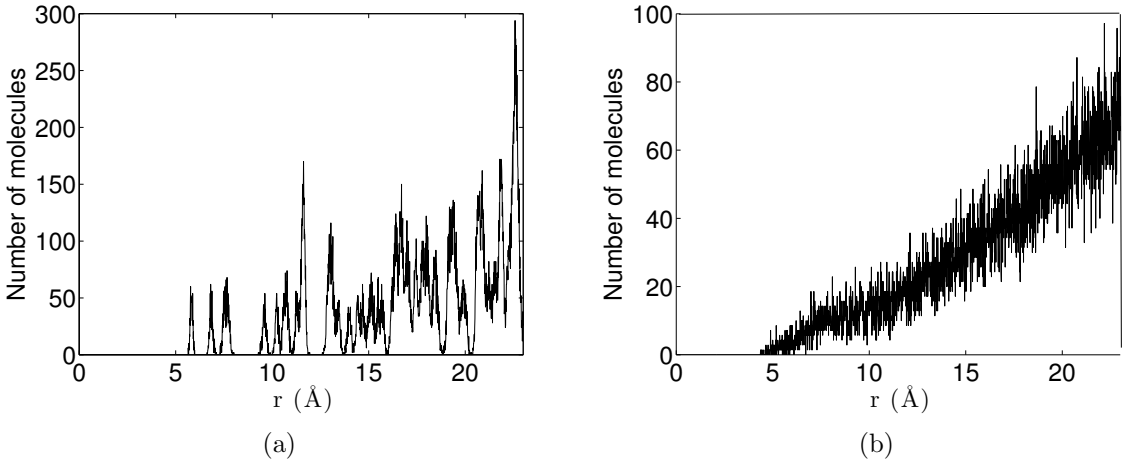

Figure 5.8: Plots of the molecular distribution function of OTP molecules in the region $r \leq 24\,\text{Å}$, as this is half the radius of the refined structural models. (a) Crystal, (b) Glass.

histogram of inter-atomic separations they are a histogram of inter-molecular separations. Therefore, in the same way as a set of sharp peaks in an atomic PDF corresponds to an ordered arrangement of atoms on that length scale, a set of sharp peaks in figure 5.8 corresponds to an ordered arrangement of molecules on that length scale. Hence, it is clear from figure 5.8(b) that there is no order, on any length scale, in the arrangement of OTP molecules in the glass while the sharp peaks in figure 5.8(a) confirm the well known long-range order of molecules in a crystal. This is in sharp contrast to the almost unchanged structure of the individual OTP molecules, as demonstrated by tables 5.4 and 5.5, and clearly demonstrates, by real-space structural refinement, the preservation of short-range order and loss of long-range order through a glass transition.

As well as there being no order to the inter-molecular separations in a glass, there should be no order to the orientations of molecules in a glass. These orientations, calculated as described above, are plotted for molecules in both the glass and crystal in figure 5.9. The mean and standard deviation of the angles between the corresponding orientation vectors of the slow and rapid cool glass was found to be 4.3° and 2.2° respectively, therefore it was assumed that there was no significant difference between the orientation of molecules in either the slow or rapid cool glass. Hence, for clarity, only the orientation vectors of the slow cool glass are plotted in figure 5.9.

The molecular orientations shown in figure 5.9 show four distinct orientations of

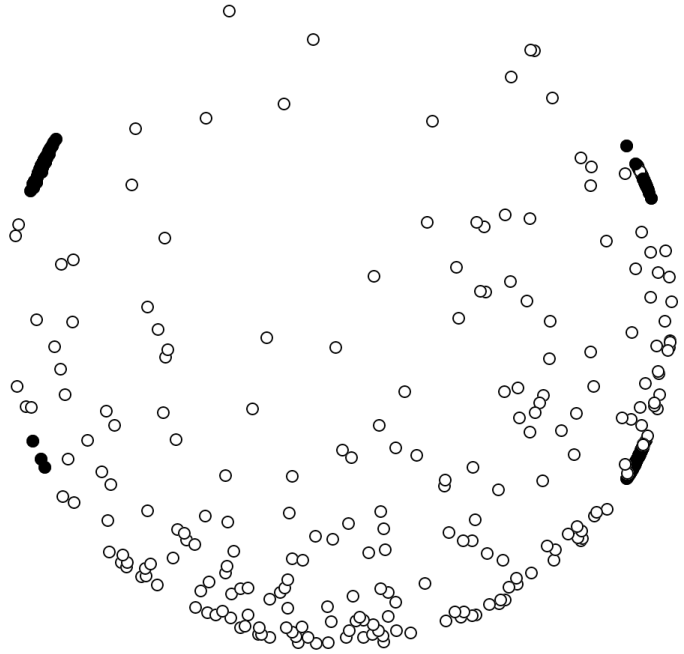

Figure 5.9: Real-space stereographic projection of the orientation of OTP molecules, viewed along the c axis. Crystal: black; glass: white.

OTP molecules in the crystalline phase. These four orientations correspond to the four molecules in the unit cell of OTP. In contrast the molecular orientations in the glass phase, as predicted, show a disordered distribution.

Of the 511 glass phase molecular orientations shown in figure 5.9 approximately 400 have a negative contribution to the orientation vector along one direction, about 80% of molecules in the glass phase 'point' along one direction. This shows a non-isotropic distribution in the orientation of OTP molecules in the glass phase. The distribution of molecular orientations in the glass phase is expected to be isotropic, and so the origin of the observed non-isotropic distribution was investigated; is this distribution given by the MD simulations described in section 5.4.1 or by the RMC refinements? The mean and standard deviation of the angles between the corresponding orientation vectors of the MD simulation and the RMC refinement of the slow cool glass were found to be 3.6° and 1.9° respectively. From this angle it can be seen that the orientation of the OTP molecules in the glass phase are not significantly changed during RMC refinement and that the anomalous non-isotropic distribution of molecular orientations shown in figure

5.9 has its origin in the MD simulation.

5.7 Conclusions

The study reported in this chapter has compared the magnitude of the localised structural fluctuations in both the glass and crystalline phases of OTP as deduced from RMC analysis of neutron total scattering. These refined structural models show the preservation of short-range order and complete loss of long-range order across the glass transition. As can be seen in the glass and crystalline phases PDF's, and emphasised in the molecular distribution function in figure 5.8, order is only preserved to a radius of about 5 Å - the radius of one OTP molecule.

The orientation of OTP molecules in the glass phase appears to be unchanged by the presented RMC refinements and are determined entirely by the MD simulations, with RMC only refining the internal torsional flexibility of an OTP molecule. This suggests that RMC is either not capable of the cooperative atomic motion this orientational refinement would require or that there is no driving force for orientational refinement contained within the experimental data used.

Chapter 6

Adamantane

6.1 Introduction

The crystal structures adopted by symmetric organic molecules due to the weak, non-directional, van der Waals interactions that bind them together in the solid state remain poorly understood. In adamantane, $C_{10}H_{16}$, these weak intermolecular interactions result in a phase transition between an ordered low-temperature phase and a disordered high-temperature phase in which molecules exist in different orientational states.

Adamantane is the simplest of the diamonoid structures [93, 94], consisting of four connected cyclohexane rings in the 'armchair' configuration, resulting in a highly symmetric cage-like molecule that is both rigid and virtually stress-free, figure 6.1. At room temperature adamantane has a face-centred cubic crystal structure ($Fm\bar{3}m$, $a = 9.426\,\text{Å}$, $Z = 4$), with a disordered arrangement of molecules in two orientation, as illustrated in figure 6.2(b). These two orientations are given by a 90° rotation of an adamantane molecule such that the eight methine carbons of the two molecules are positioned at the eight corners of a cube [95, 96]. At 208 K adamantane goes through a first-order structural phase transition [97, 98] to an ordered body-centred tetragonal crystal structure ($P\bar{4}2_1c$, $a = 6.614\,\text{Å}$, $c = 8.875\,\text{Å}$, $Z = 2$), in which the molecules freeze into an ordered arrangement [95, 99], as illustrated in figure 6.2(a). In this low-temperature ordered phase the two molecules have the same orientation except for a 9° tilt about the c axis. As one might expect from a phase transition with a significant decrease in volume, this can also be induced by increased pressure [100–103].

As the phase transition in adamantane is primarily due to the rotation of individual molecules, the phase transition can not be easily studied crystallographically. However, information relating to the rotation of individual molecules may be contained within adamantane's PDF. Therefore in this chapter the PDFs derived from a neutron total scattering experiment and subsequent RMC refinement of both phases of adamantane are

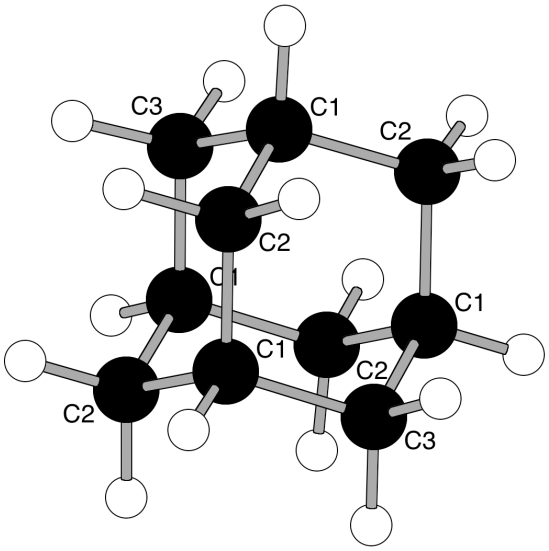

Figure 6.1: Structure of an adamantane molecule, with four methine carbons linked by six methylene bridge carbons, hydrogen labels are omitted for clarity. C: black; H: white.

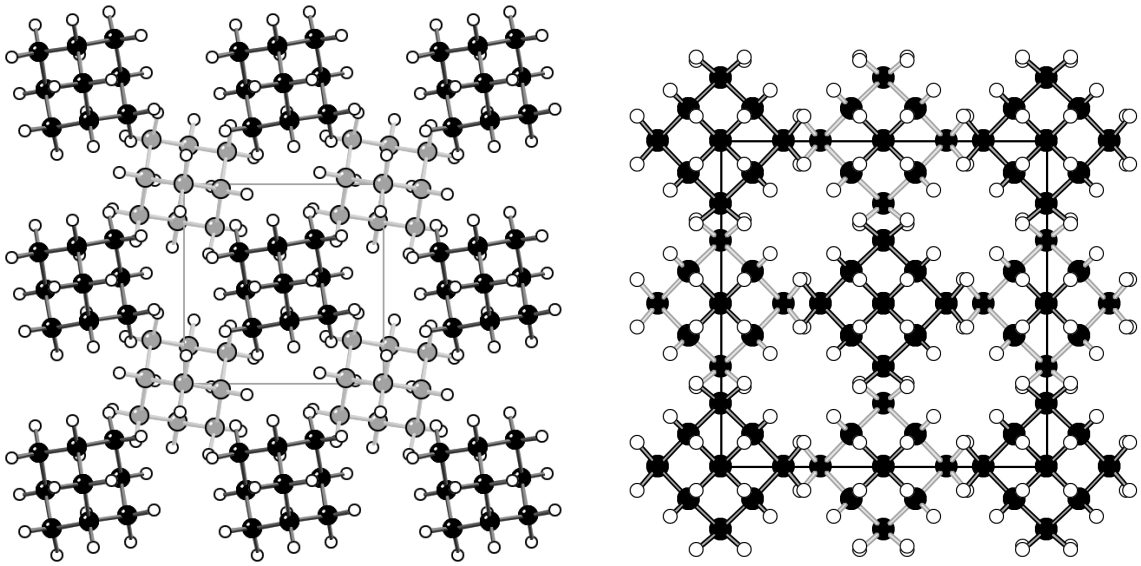

(a) (b)

Figure 6.2: Crystal structure of adamantane viewed along the c axis, (a) in its low-temperature ordered phase, (b) in its high-temperature disordered phase. C: black; H: white.

presented.

6.2 Experimental

Neutron total scattering data were collected at various temperatures on the POLARIS diffractometer, as described in section 2.2.3. Perdeuterated adamantane was purchased from Qmx Laboratories with a deuteration ratio of 98%. Data suitable for RMC refinements were obtained at temperatures of 100, 198, 218 and 258 K.

6.3 Data Processing

The background was subtracted and the data normalised using the program Gudrun [35] as described in section 2.3.1. A sample of the PDFs produced by Gudrun are shown in figure 6.3 and the key parameters used in Gudrun to produce them are given in table 6.1.

temperatures (K)	tweak factor	Q_{max} (Å^{-1})	Q_{T} (Å^{-1})	Lorch parameters	
				Δ (Å)	β
100	2.988	30	3	0.000	NA
198	2.938	30	3	0.015	0.5
218	2.868	30	3	0.030	0.5
258	2.842	30	3	0.030	0.5

Table 6.1: Gudrun parameters used to produce diffuse scattering functions, $i(Q)$ and $D(r)$.

The Bragg diffraction profile was also separately extracted, and Rietveld refinement performed for the low-temperature ordered phase using GSAS [38] and EXPGUI [39] in order to extract lattice parameters and to obtain the peak shape, background and scale parameters for use in the RMC refinements. The structure of the low-temperature ordered phase of adamantane given in J. Donohue *et al.* [99], following substitution of the hydrogens for deuteriums, was used as the starting model for these refinements. In these Rietveld refinements constraints were placed on the isotropic atomic displacement parameters of all atoms such that all carbon atoms have the same value and all deuterium atoms have the same value. The C–D bond distances were restrained to 1.1 Å. Despite the presence of rigid individual molecules, considering the very high symmetry of the low-

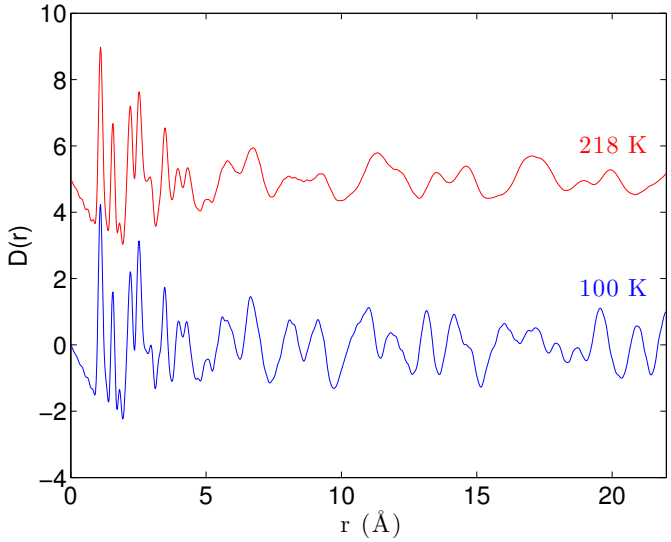

Figure 6.3: PDFs, $D(r)$, for the high- and low-temperature phases of adamantane. The two phases have very similar local structure below about 5 Å, but differ in the longer-range correlations above this radius. Blue: 100 K; red: 218 K.

temperature phase of adamantane ($P\bar{4}2_1c$) resulting in only seven sets of independent atomic coordinates to be refined, the use of rigid body constraints was not found to be necessary.

Due to the disordered arrangement of adamantane molecules of different rotational orientations in the high-temperature phase, Rietveld refinement of this phase without fractional occupancies was not possible. As a disordered initial configuration was used for RMC refinements of the high-temperature phase of adamantane, a Rietveld refined crystal structure with fractional occupancies would be of little use in the production of initial configurations. Therefore Le Bail fits were performed on this phase using GSAS [38] and EXPGUI [39] in order to extract lattice parameters and to obtain the peak shape and background for use in the RMC refinements. An accurate scale parameter is not given by a Le Bail fit and so the value used in the RMC refinements was calculated by a comparison of the integral of the Bragg profile given by RMC with the integral of that given by the Le Bail fit. Example fits, lattice parameters, cell volumes and the refinement residuals of both the Rietveld refinement and Le Bail profile extraction are given in Appendix A.

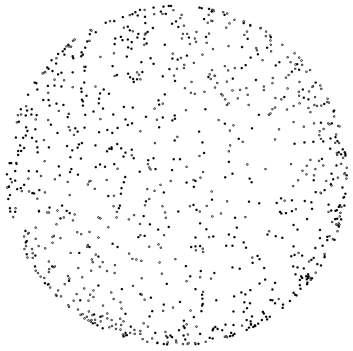

Figure 6.4: Real-space stereographic projection of the molecular orientations in the randomly rotated adamantane molecules, as used in RMC refinement of the disordered high-temperature phase. Molecular orientations: black.

6.4 Reverse Monte Carlo

6.4.1 Initial Configurations

Initial configurations of the low-temperature ordered phase of adamantane were produced for each temperature as $8 \times 8 \times 6$ supercells of their refined crystal structures, obtained by Rietveld refinement, using the program RMCcreate [5]. This procedure resulted in initial configurations of the low-temperature phase with side length of approximately 50 Å, containing 19968 atoms.

Initial configurations of the high-temperature disordered phase of adamantane were produced by placing an individual randomly rotated adamantane molecule, the motif, on an array of lattice points reflecting the phase's face-centered cubic symmetry. An array of 500 lattice points were produced for each temperature as $5 \times 5 \times 5$ supercells of the symmetry equivalent points in the $Fm\bar{3}m$ unit cell, with lattice parameters given by a LeBail fit. The randomly rotated adamantane molecules, or motifs, were produced by rotating the 26 atoms of an individual adamantane molecule, given by a prior Rietveld refinement, about the molecule's centre of mass such that the orientations of the molecules were randomly distributed on the surface of a sphere, as illustrated in figure 6.4. The resulting orientationly disordered configurations were cubic with side length of approximately 50 Å and contained 13000 atoms.

Exact structural details of the initial configurations are given in Appendix B and the code written by the author to produce the high-temperature disordered configurations is given in Appendix C.

6.4.2 Constraints and Restraints

A number of constraints, in the form of minimum distances, and restraints, in the form of molecular potentials, were applied to all of the adamantane RMC refinements and are given below and in tables 6.2 and 6.3. Two distance window constraints were also applied to these refinements, constraining the C–C distance to between 1.0 and 2.0 Å and the C–D distance to between 0.5 and 1.5 Å.

atom pair	distance (Å)
C C	1.00
C D	0.90
D D	1.50

Table 6.2: Minimum Distance of Approach

Potentials	Atoms	Values
$E = D[(1 - \exp(-\alpha(r_{ij} - r_0)))^2]$	C–D	$D = 2.275$ eV $\alpha = 2.55$ Å^{-1} $r_0 = 1.11$ Å
	C–C	$D = 2.155$ eV $\alpha = 2.55$ Å^{-1} $r_0 = 1.52$ Å
$E = \frac{K}{2}(\cos(\theta_{ijk}) - \cos(\theta_0))^2$	$\widehat{\text{CCC}}$	$K = 8.364$ eV $\theta_0 = 109.5°$
	$\widehat{\text{CCD}}$	$K = 7.364$ eV $\theta_0 = 110.1°$

Table 6.3: Summary of the potentials used in the RMC refinement, adapted from the MM3 potentials [42] as described in the RMCProfile manual [43].

6.5 Analysis

In these RMC refinements it was found that the value of the function χ^2_{RMC} decreased towards a converged minimum value after approximately 80 million generated atomic moves, over 6000 moves per atom for the low-temperature phase and approximately 150 generated million atomic moves, over 18000 moves per atom for the high-temperature phase. At this point the refinements were considered to have reached an equilibrium and so RMC was terminated. For each of these two phases six independent RMC refinements were performed to give improved statistical accuracy to extracted histograms, averages and standard deviations. Examples of the final fits to the $D(r)$, $i(Q)$ functions and Bragg data are shown in figure 6.5.

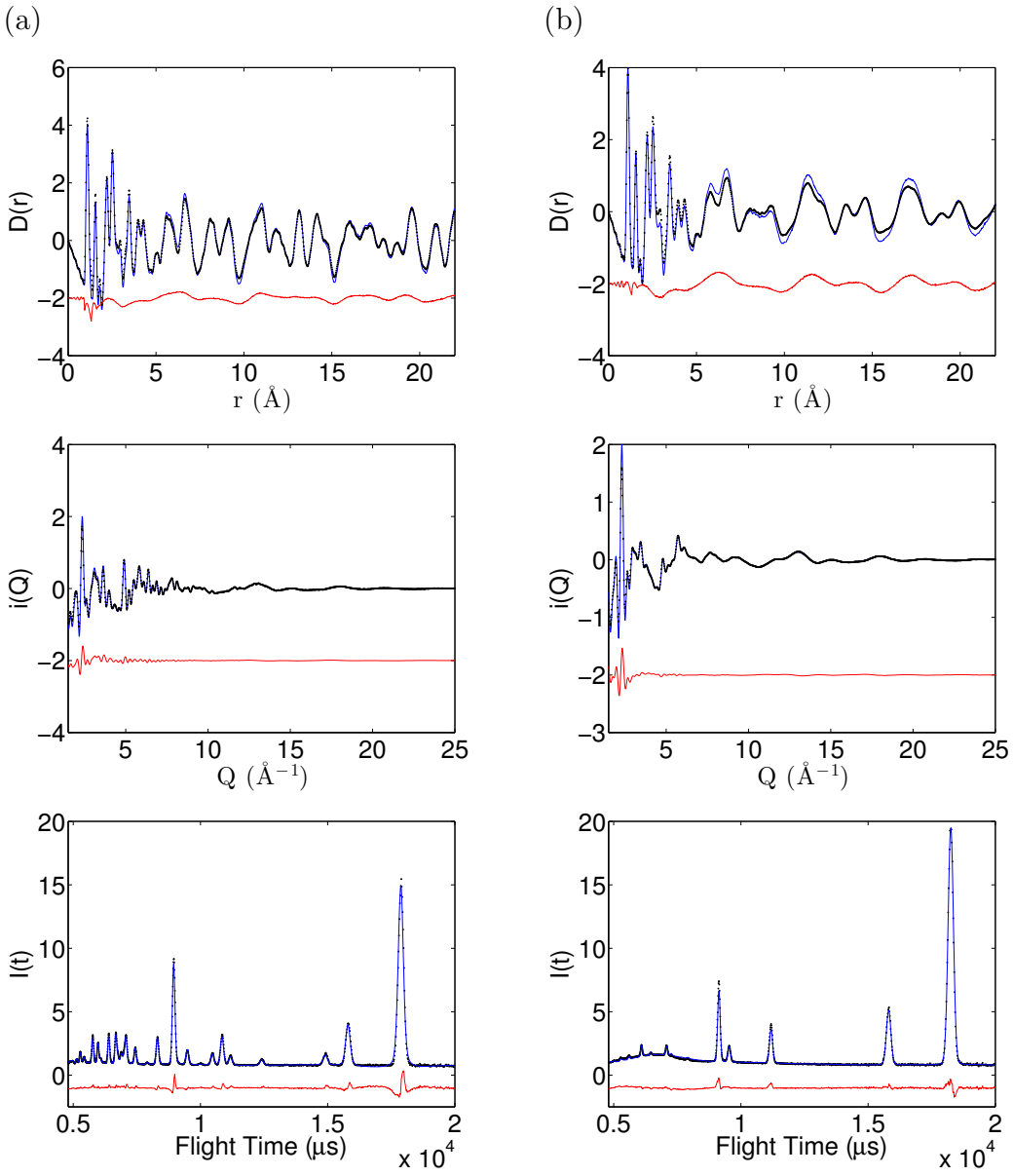

Figure 6.5: Converged fits to the $D(r)$, $i(Q)$ and $I(t)$ ($2\theta = 52°$) functions, (a) Adamantane 100 K, (b) Adamantane 218 K. Experimental data: black dots; RMC fits: blue line; difference: red line.

The basic analysis described in section 2.5 calculates all the bond distances and basic three atom angles. Individual adamantane molecules are assumed to be largely rigid and so to asses this, as well as the basic bond lengths and angles, the angles given by the tetrahedron centred on the centre of mass of an adamantane molecule and pointed at the four methane carbons (C1 in figure 6.1) were calculated.

To investigate the orientation of adamantane molecules in the ordered and disordered phases, the orientation of these molecules were calculated. The orientation of an individual

T (K)	C–D (Å)		$\widehat{\text{CCD}}$(°)		C–C(Å)		$\widehat{\text{CCC}}$(°)		tetrahedral (°)	
	mean	st dev	mean	st dev	mean	st dev	mean	st dev	mean	st dev
100	1.1	0.06	109.6	4.1	1.5	0.05	109.4	2.2	109.5	1.5
198	1.1	0.06	109.7	3.6	1.5	0.05	109.4	2.2	109.5	1.4
218	1.1	0.07	109.2	6.8	1.5	0.06	109.3	3.7	109.5	1.7
258	1.1	0.07	109.2	6.0	1.5	0.06	109.3	3.6	109.5	1.6

Table 6.4: Mean and standard deviations of the five within cluster structural parameters for all refined configurations, in each case averaged over six RMC refinements.

adamantane molecule was assessed by calculating the four vectors between the centre of mass of the molecule and the four methine carbons. These vectors were calculated for all molecules and collapsed onto a single origin to give a real-space stereographic projection of the molecular orientations within an adamantane crystal. The code written by the author to produce these bond lengths, angles and orientation vectors is given in Appendix C.

6.6 Results and Discussion

The mean values and standard deviations of the four restrained parameters relating to the structure of individual adamantane molecules, the C–C and C–D bond lengths as well as the $\widehat{\text{CCC}}$ and $\widehat{\text{CCD}}$ angles, are given in table 6.4. The individual adamantane molecules are rigid units, as can be seen from the very similar low-r peaks in the experimental PDFs of both phases, shown in figure 6.3. Therefore both the low- and high-temperature phases should display similar distributions of all bond lengths and angles in the refined structure (identical to within atomic thermal motion). This is broadly borne out in the refined parameter distributions; the bond lengths and angles are more or less constant in both mean and standard deviation across both refined phases. The reproduction of this experimentally observed local structure in the refined structure, with little variation in table 6.4, shows the utility of the potentials applied to the presented refinements.

To further test the extent to which the rigidity of individual adamantane molecules is preserved in the RMC refinements, the tetrahedral angles between the vectors connecting the four methine carbons and the centre of mass of the molecule were calculated. Its mean and standard deviation is given in table 6.4. That the ideal tetrahedral angle of 109.5° is preserved with a low and relatively constant standard deviation shows that the

(a) (b)

Figure 6.6: Real-space stereographic projection of the molecular orientations in the high-temperature disordered phase of adamantane, viewed along the c axis. (a) In the RMC initial configuration, (b) in the RMC refined configuration. Orientation I: blue; orientation II: red.

tetrahedral structure of an adamantane molecule is maintained during RMC refinement.

The orientations of adamantane molecules, calculated as described above, are plotted for the high-temperature phase, 218 K, in figure 6.6. As described in section 6.4.1 the initial configurations of the high-temperature phase of adamantane were produced with each adamantane molecule randomly rotated; hence the isotropic distribution of molecular orientations shown in figure 6.6(a). However, as shown in figure 6.6(b), two distinct orientations of adamantane molecules emerge during refinement of the high-temperature phase (orientations I and II). These two orientations are given by a 90° rotation of an adamantane molecule, such that the eight methine carbons of the two molecules are positioned at the eight corners of a cube. These two molecular orientations can be inferred from the structure that is given by a Rietveld refinement using fractional occupancies, as described in C. E. Nordman *et al.* [95].

The emergence of these two distinct orientations from an initial configuration with random orientations, while maintaing the molecular structure of individual adamantane molecules, can only be accomplished by the correlated motion of all the constitute atoms of an adamantane molecule. The large amount of atomic motion, required by the described molecular rotations, explains the very high number of atomic moves generated before the

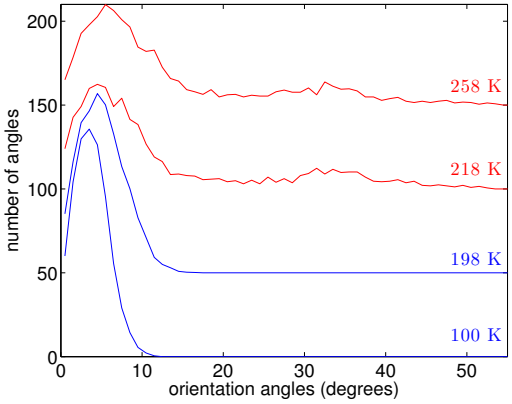

Figure 6.7: Histogram of the rotation angles of individual adamantane molecules within an adamantane crystal. Low-temperature phase: blue; high-temperature phase: red.

high-temperature refinements reached equilibrium (see section 6.5).

Four rotation angles per molecule, between the vectors from the centre of mass of an adamantane molecule to the corresponding methine carbons in the refined RMC configuration and those in the ideal orientations were calculated. These rotation angles measure the rotation required to map an adamantane molecule in the refined RMC configuration onto the corresponding ideally orientated adamantane molecule, measuring the orientation of an individual adamantane molecule relative to the ideal, a histogram of these angles is shown in figure 6.7. The mean of this rotation angle is 28° in the random initial configurations of the high-temperature phase and is more than halved through refinement to 12.5° and 13.1° in the 218 K and 258 K refinements respectively, averaged over six RMC refinements. This reduction indicates molecular rotations, showing a strong preference for adamantane molecules in the high-temperature phase to rotate such that they adopt either of the two orientations.

A similar set of rotational analysis was performed on refinements of the low-temperature phase of adamantane, shown in the histogram given in figure 6.7. In this case, as there is an ordered crystal structure in the initial configuration of this phase, the rotation angles, relative to the ideal orientations, are 0° in the initial configurations. Upon refinement the mean of these rotation angles were 4.2° and 5.4° in the 100 K and 198 K refinements respectively, averaged over six RMC refinements. These refined values show that there is no preference for adamantane molecules in the low-temperature phase to rotate from the

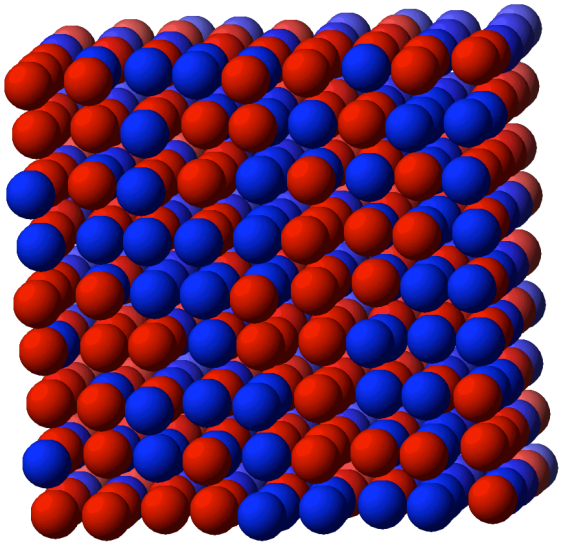

Figure 6.8: Arrangement of adamantane molecules in the high-temperature disordered phase, viewed along the c axis. Orientation I: blue; orientation II: red.

ordered structure given by a conventional Rietveld refinement.

However, whether an adamantane molecule in the high-temperature phase rotates from a random orientation to either of the two orientations observed appears to be random, with no preference for one rotation over the other and no preference towards the formation of clusters of molecules in the same orientation. This rotational freedom results in the disordered arrangement of adamantane molecules shown in figure 6.8; molecular arrangements in which no significant clusters of adamantane molecules in the same orientation were observed.

6.7 Conclusions

The study reported in this chapter has examined the localised structural fluctuations in the low- and high-temperature phases of adamantane as deduced from reverse Monte Carlo analysis of neutron total scattering. In the high-temperature phase adamantane molecules have been shown to rotate such that they exist in one of two orientations and that the resulting crystal structure consists of a disordered arrangement of these two orientations with seemingly no preference for the formation of clusters of molecules in the

same rotational state. That the correlated atomic motion required by these molecular rotations are captured by an RMC refinement is evidence for the potential utility in the application of RMC refinements to the study of disordered molecular materials. The refinement of the orientations of adamantane molecules by RMC show that there must be a strong driving force for orientational refinement within the experimental data used by RMC.

Chapter 7

Adamantanecarboxylic acid

7.1 Introduction

Studies using a wide variety of experimental techniques have shown that the order-disorder phase transition described in chapter 6 often persists in derivatives of adamantane [105–110]. However, since these derivatives will be more polar and less spherical than the parent molecule, they generally rotate less freely, resulting in a higher transition temperature. In 2-chloroadamantane two transitions are detected at 242 and 227 K [106] with a transition at 231 K in 1-fluoroadamantane [107]. If the substituent is capable of intermolecular hydrogen bonding then the molecular rotation required will be further restricted, 1-adamantanol has a transition temperature of 359 K [108]. However in adamantanamine hydrochloride a transition occurs at 124 K with an entropy change of 2.51 J K^{-1} [109] and at 251 K with an entropy change of 8.96 J K^{-1} in adamantanecarboxylic acid [110]. In both these compounds the transition temperatures and entropies of transition are too low for the full order-disorder transition seen in the parent compound. In these compounds the disorder in the high-temperature phase has been interpreted in terms of rotation of the adamantyl groups alone.

In both its high- and low-temperature phases, adamantanecarboxylic acid has a triclinic unit cell, space group $P\bar{1}$, with two molecules per unit cell that exist as a dimer, shown in figure 7.1. The low-temperature phase ($a = 6.452(3)$ Å, $b = 6.681(2)$ Å, $c = 11.510(3)$ Å, $\alpha = 80.84(2)°$, $\beta = 87.22(3)°$, $\gamma = 74.11(3)°$) is ordered while the high-temperature phase ($a = 6.503(2)$ Å, $b = 6.849(2)$ Å, $c = 11.620(4)$ Å, $\alpha = 77.11(2)°$, $\beta = 85.77(2)°$, $\gamma = 76.34(2)°$) is disordered. In the high-temperature phase the adamantyl groups of different dimers occupy two orientations, in an approximate 40:60 proportion, at about 14° to one another with the two carboxylate groups occupying two orientations at about 170° to one another. The hydrogen bonds between carbonyl groups prevent rotation of the adamantanecarboxylic acid dimer about the two axes perpendicular to the

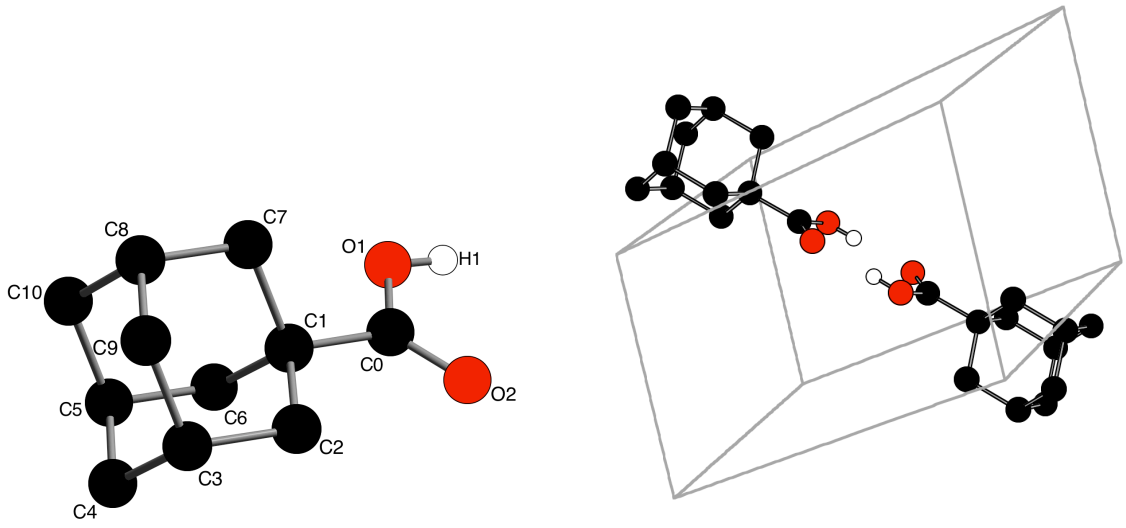

(a) (b)

Figure 7.1: Structure of adamantanecarboxylic acid, (a) as an individual molecule, (b) as a dimer, hydrogens, except for (OH), are omitted for clarity. C: black; O: red; H: white.

axis containing the carboxylate [111], thus restricting rotation such that the dimer can only rotate about its molecular axis.

This complete prevention of rotation about two axes and the torsional flexibility between the adamantyl and carbonyl groups offers an interesting contrast to adamantane. Combined with the potential distortion in the hydrogen bonds between carbonyl groups a large degree of local structural fluctuation may be anticipated in adamantanecarboxylic acid. Therefore in this chapter the PDFs derived from a neutron total scattering experiment and subsequent RMC refinement of both phases of adamantanecarboxylic acid are presented.

7.2 Experimental

Neutron total scattering data were collected at various temperatures on the POLARIS diffractometer, as described in section 2.2.3. Perdeuterated adamantanecarboxylic acid was purchased from Qmx Laboratories with a deuteration ratio of 98%, however the OH was undeuterated. Data suitable for RMC refinements were obtained at temperatures of

150, 240, 270 and 300 K.

7.3 Data Processing

The background was subtracted and the data normalised using the program Gudrun [35] as described in section 2.3.1. A sample of the PDFs produced by Gudrun are shown in figure 7.2 and the key parameters used in Gudrun to produce them are given in table 7.1. The large increase in the value of the tweak factor used in Gudrun for the processing of data at 300 K compared to that used when processing data at 270 K is explained by the change in the sample environment; a cryostat to a low-temperature furnace. At all temperatures the tweak factors are considerably larger than the anticipated values, therefore, since the tweak factor is used as an adjustment parameter in Gudrun, there is an unknown error in the Gudrun processing of adamantanecarboxylic acid.

temperatures (K)	tweak factor	Q_{max} (Å^{-1})	Q_{T} (Å^{-1})	Lorch parameters	
				Δ (Å)	β
150	5.21961726	30	5	0.025	0.5
240	4.82303476	30	5	0.030	0.5
270	4.94930876	30	5	0.030	0.5
300	7.32811559	30	5	0.035	0.5

Table 7.1: Gudrun parameters used to produce diffuse scattering functions, $i(Q)$ and $D(r)$.

The Bragg diffraction profile was also separately extracted, and Rietveld refinement performed for the low-temperature ordered phase using GSAS [38] and EXPGUI [39] in order to extract lattice parameters and to obtain the peak shape, background and scale parameters for use in the RMC refinements. The structure of the low-temperature ordered phase of adamantanecarboxylic acid given in F. Belanger-Gariepy *et al.* [111], following substitution of the hydrogens for deuteriums [except for (OH)], was used as the starting model for these refinements. In these Rietveld refinements constraints were placed on the isotropic atomic displacement parameters of all atoms such that all carbon atoms have the same value and all deuterium atoms have the same value. As refinement of the hydrogen positions resulted in an unstable refinement and that the carbonyl group, including the

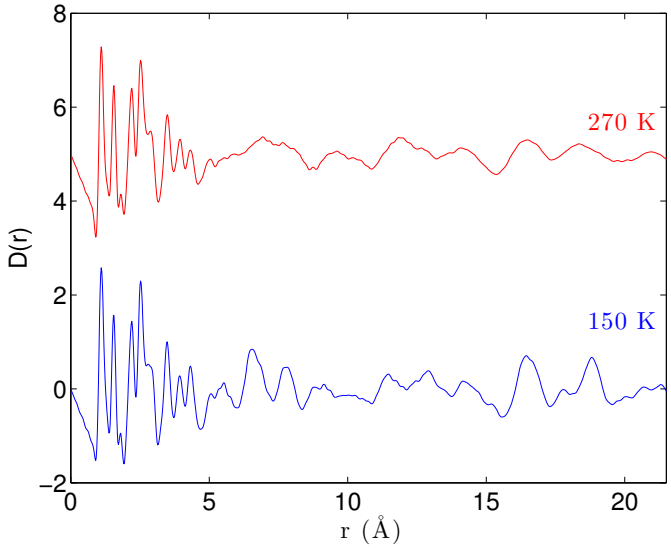

Figure 7.2: PDFs, $D(r)$, for the high- and low-temperature phases of adamantanecarboxylic acid. The two phases have very similar local structure below about 5 Å, but differ in the longer-range correlations above this radius. 150 K: blue; 270 K: red.

adamantly-carbonyl C–C bond, was assumed to be a rigid unit, the carbonyl groups were treated as rigid bodies during the refinement with only their centre of mass and rotation angles allowed to vary. Additionally the C–D bond distances were restrained to 1.1 Å.

Due to the disordered arrangement of adamantanecarboxylic acid molecules of different rotational orientations in the high-temperature phase, Rietveld refinement of this phase without fractional occupancies was not possible. As a disordered initial configuration was used for RMC refinements of the high-temperature phase of adamantanecarboxylic acid, a Rietveld refined crystal structure with fractional occupancies would be of little use in the production of initial configurations. Therefore Le Bail fits were performed on this phase using GSAS [38] and EXPGUI [39] in order to extract lattice parameters and to obtain the peak shape and background for use in the RMC refinements. An accurate scale parameter is not given by a Le Bail fit and so the value used in the RMC refinements was calculated by a comparison of the integral of the Bragg profile given by RMC with the integral of that given by the Le Bail fit. Example fits, lattice parameters, cell volumes and the refinement residuals of both the Rietveld refinement and Le Bail profile extraction are given in Appendix A.

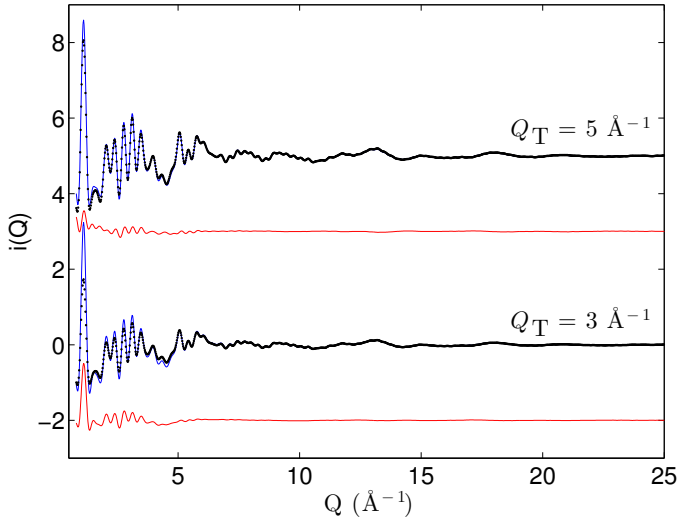

Figure 7.3: The total scattering function, $i(Q)$, given by test RMC refinements of adamantanecarboxylic acid, using data processed using Q_{T} of either 3 or 5 Å^{-1}. Experimental data: black dots; RMC fits: blue line; difference: red line.

7.4 Reverse Monte Carlo

During test RMC refinements it was found that the large low-Q peak in the total scattering function, $i(Q)$, at approximately 1 Å^{-1}, was fit very poorly, as shown in figure 7.3. The intensity of this peak in the experimental data was much lower than the intensity calculated from the refined structure. One possible cause for this could be that the Q dependent background subtracted from the total scattering function by Gudrun, see section 2.3.1, is too large; that the diffuse scattering from adamantanecarboxylic acid is weaker than assumed by Gudrun and so the Q dependent background Gudrun subtracts includes required diffuse scattering intensity. Therefore this background needs to be reduced which is accomplished by an increase in the top hat function in Gudrun. Hence Q_{T} was increased from 3 to 5 Å^{-1} and a new RMC test run, keeping all other parameters the same, was performed. Fits produced using this new top hat function showed a significant improvement in the fit observed in the low-Q region of the total scattering function, as shown in figure 7.3.

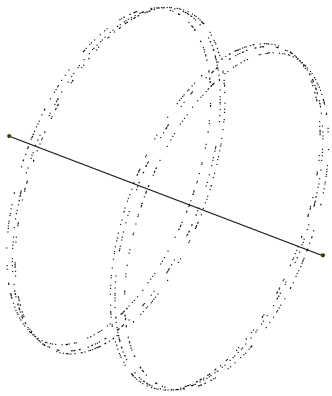

Figure 7.4: Real-space stereographic projection of the molecular orientations in the randomly rotated adamantanecarboxylic acid dimers, as used in RMC refinement of the disordered high-temperature phase. Molecular orientations: black; molecular axis: grey line.

7.4.1 Initial Configurations

Initial configurations of the low-temperature ordered phase of adamantanecarboxylic acid were produced for each temperature as $7 \times 7 \times 4$ supercells of their refined crystal structures, obtained by Rietveld refinement, using the program RMCcreate [5]. This procedure resulted in initial configurations of the low-temperature phase with side length of approximately 50 Å, containing 11368 atoms.

Initial configurations of the high-temperature disordered phase of adamantanecarboxylic acid were produced by placing an individual adamantanecarboxylic acid dimer rotated about its molecular axis, the motif, on an array of lattice points reflecting the phase's body-centered cubic symmetry. An array of 196 lattice points were produced for each temperature as $7 \times 7 \times 4$ supercells of the symmetry equivalent points in the high-temperature $P\bar{1}$ unit cell, with lattice parameters given by a LeBail fit. The randomly rotated adamantanecarboxylic acid dimer, the motifs, were produced by rotating the 58 atoms of an individual adamantanecarboxylic acid dimer about the molecular axis such that the orientations of the dimer, as measured perpendicular to the molecular axis, were randomly distributed on the edge of a circle, as illustrated in figure 7.4. The resulting orientationally disordered configurations were approximately cubic with side length of 50 Å and contained 11368 atoms.

Exact structural details of the initial configurations are given in Appendix B and the

code written by the author to produce the high-temperature disordered configurations is given in Appendix C.

7.4.2 Constraints and Restraints

A number of constraints, in the form of minimum distances, and restraints, in the form of molecular potentials, were applied to all of the adamantanecarboxylic acid RMC refinements and are given below and in tables 7.2 and 7.3. Two distance-windows were applied to these refinements, constraining the C–C distance to between 1.0 and 2.0 Å and the C–D distance to between 0.5 and 1.5 Å.

atom pair	distance (Å)
D D	1.50
D H	2.50
D C	0.90
D O	1.50
H H	1.50
H C	1.20
H O	0.80
C C	1.20
C O	1.00
O O	2.00

Table 7.2: Minimum Distance of Approach

Adamantanecarboxylic acid dimers are restricted to only rotate about their molecular axis, as described above. Additionally it is energetically favourable for the hydrogen bonds that produce these dimers to remain in the plane of the two carbonyl groups that contribute to these dimers. The planarity constraint described in table 7.3 was therefore applied to the 10 constituent atoms of these two carbonyl groups so as to represent the energetic favourability for the planarity of the two carbonyl groups across a dimer. This planarity constraint also has the effect of restricting the molecular rotation in adamantanecarboxylic acid to rotation only about the molecular axis.

Potentials	Atoms	Values
$E = D[(1 - \exp(-\alpha(r_{ij} - r_0)))^2]$	C–D	$D = 2.275$ eV $\alpha = 2.55$ Å^{-1} $r_0 = 1.11$ Å
	C–C	$D = 2.155$ eV $\alpha = 2.55$ Å^{-1} $r_0 = 1.52$ Å
	C–O	$D = 2.88$ eV $\alpha = 2.55$ Å^{-1} $r_0 = 1.35$ Å
	C=O	$D = 4.703$ eV $\alpha = 2.55$ Å^{-1} $r_0 = 1.21$ Å
$E = \frac{K}{2}(\cos(\theta_{ijk}) - \cos(\theta_0))^2$	$\widehat{\text{CCC}}$	$K = 8.364$ eV $\theta_0 = 109.5°$
	$\widehat{\text{CCD}}$	$K = 7.364$ eV $\theta_0 = 110.1°$
	$\widehat{\text{OCO}}$	$K = 21.222$ eV $\theta_0 = 121.5°$
$E = P\omega$	CCOOHHOOCC	$P = 5000.0$

Table 7.3: Summary of the potentials used in the RMC refinement, bond and angle potentials are adapted from the MM3 potentials [42] as described in the RMCProfile manual [43].

7.5 Analysis

In these RMC refinements it was found that the value of the function χ^2_{RMC} decreased towards a converged minimum value after approximately 100 million generated atomic moves, over 8000 moves per atom. At this point the refinements were considered to have reached an equilibrium and so RMC was terminated. For each of these two phases six independent RMC refinements were performed to give improved statistical accuracy to extracted histograms, averages and standard deviations. Examples of the final fits to the $D(r)$, $i(Q)$ functions and Bragg data are shown in figure 7.5.

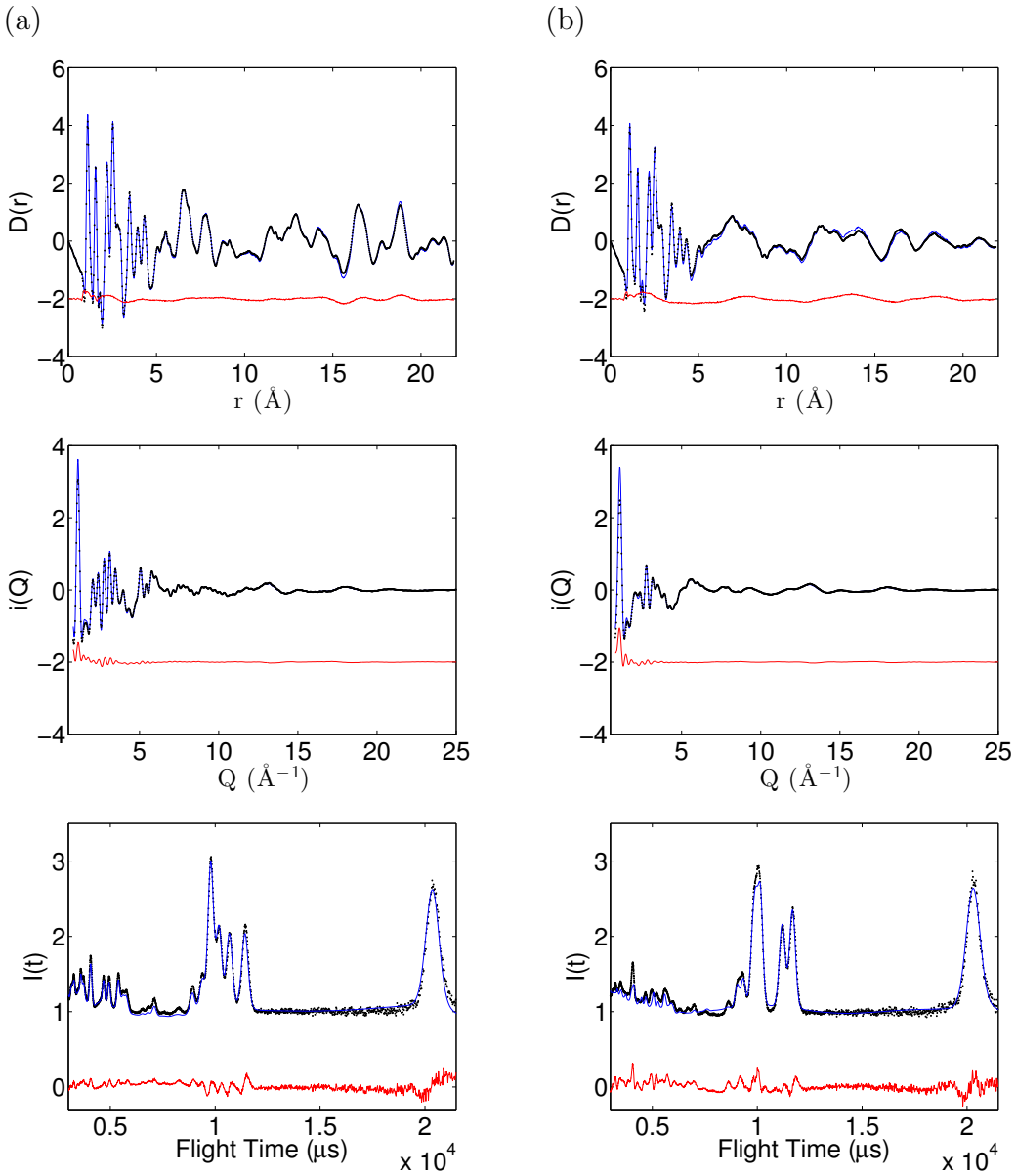

Figure 7.5: Converged fits to the $D(r)$, $i(Q)$ and $I(t)$ ($2\theta = 34°$) functions, (a) Adamantanecarboxylic acid 250 K, (b) Adamantanecarboxylic acid 270 K. Experimental data: black dots; RMC fits: blue line; difference: red line.

The basic analysis described in section 2.5 calculates all the bond distances and basic three atom angles. Individual adamantyl groups are assumed to be largely rigid and so to asses this, as well as the basic bond lengths and angles, the angles given by the tetrahedron centred on the centre of mass of an adamantyl group and pointed at the three methane carbons (C3, C5 and C8 in figure 7.1(a)) and the acid connected carbon (C1 in figure 7.1(a)) were calculated.

T (K)	C–D (Å)		$\widehat{\text{CCD}}$(°)		C–C(Å)		$\widehat{\text{CCC}}$(°)		tetrahedral (°)	
	mean	st dev	mean	st dev	mean	st dev	mean	st dev	mean	st dev
150	1.1	0.063	110.0	4.3	1.53	0.047	109.4	2.6	109.5	1.6
240	1.1	0.069	110.1	4.6	1.53	0.049	109.4	2.8	109.5	1.8
270	1.1	0.078	109.5	6.2	1.53	0.059	109.3	4.6	109.5	2.5
300	1.1	0.062	109.8	7.5	1.52	0.066	109.3	5.3	109.5	3.0

Table 7.4: Mean and standard deviations of the five structural parameters within the adamantyl group for all refined temperatures, in each case averaged over six RMC refinements.

To investigate the orientation of adamantanecarboxylic acid dimers in the ordered and disordered phases, the orientation of the two adamantyl groups within each dimer were calculated. The orientation of an individual adamantyl group was assessed by calculating the four vectors between the centre of mass of the adamantyl group and the three methine carbons and the acid connected carbon. These vectors were calculated for all adamantyl groups and collapsed onto a single origin to give a real-space stereographic projection of the molecular orientations within an adamantanecarboxylic acid crystal. The code written by the author to produce these bond lengths, angles and orientation vectors is given in Appendix C.

7.6 Results and Discussion

The mean values and standard deviations of the four restrained parameters relating to the structure of individual adamantyl groups, the C–C and C–D bond lengths as well as the $\widehat{\text{CCC}}$ and $\widehat{\text{CCD}}$ angles, are given in table 7.4. The individual adamantyl groups are rigid units, as can be seen from the very similar low-r peaks in the experimental PDFs of both phases, shown in figure 7.2. Therefore both the low- and high-temperature phases should display similar distributions of all bond lengths and angles in the refined structure (identical to within atomic thermal motion). This is broadly borne out in the refined parameter distributions; the bond lengths and angles are more or less constant in both mean and standard deviation across both refined phases. The reproduction of this experimentally observed local structure in the refined structure, with little variation in table 7.4, shows the utility of the potentials applied to the adamantyl groups in the presented refinements.

T (K)	C–O (Å)		C=O (Å)		$\widehat{OCO}$(°)		O–H(Å)		ω (10^{-4}Å^2)	
	mean	st dev	mean	st dev	mean	st dev	mean	st dev	mean	st dev
150	1.32	0.18	1.24	0.22	122.4	2.8	1.0	0.27	22	14
240	1.33	0.15	1.24	0.18	121.9	2.7	1.0	0.25	23	13
270	1.36	0.25	1.24	0.27	120.3	2.9	1.1	0.35	19	11
300	1.31	0.25	1.22	0.26	120.9	3.5	1.1	0.39	30	19

Table 7.5: Mean and standard deviations of the five structural parameters within the carbonyl groups for all refined temperatures, in each case averaged over six RMC refinements.

To further test the extent to which the rigidity of individual adamantyl groups is preserved in the RMC refinements, the tetrahedral angles between the vectors from the three methine carbons and acid connected carbon to the centre of mass of the adamantyl groups were calculated. Its mean and standard deviation is given in table 7.4. That the ideal tetrahedral angle of 109.5° is preserved with a low and relatively constant standard deviation shows that the tetrahedral structure within an adamantyl group is maintained during RMC refinement.

The mean values and standard deviations of the four restrained parameters relating to the structure of individual carbonyl groups, the C–O and C=O bond lengths, the $\widehat{OCO}$ angles and the deviation from planarity, ω, as well as one unrestrained parameter, the O–H bond lengths, are given in table 7.5. As for the adamantyl group, the relatively stable values of these structural parameters across both phases show that the structural rigidity of the carbonyl groups is preserved and thus the utility of the potentials applied to the carbonyl groups in the presented refinements. However, in the high-temperature phase there is an increase in the mean and standard deviation of the O–H bond lengths, this may be interpreted as increased fluctuations of the hydrogen bonding in this phase. It must be noted, however, that due to the anomalously large values of the tweak factor, shown in table 7.1, combined with the problems associated with hydrogen in neutron scattering, see section 2.2, the hydrogen position is likely to be the most poorly defined parameter in these refinements.

The orientations of adamantanecarboxylic acid molecules, calculated as described above, are plotted for the high-temperature phase, 270 K, in figure 7.6. As described in section 7.4.1 the initial configurations of the high-temperature phase of adamantanecarboxylic acid were produced with each adamantanecarboxylic acid dimer randomly rotated

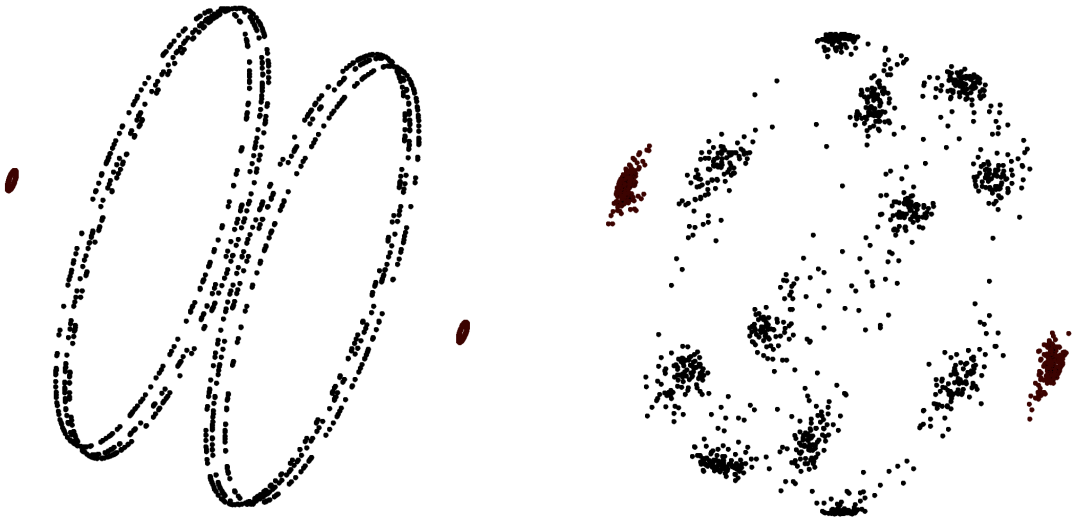

(a) (b)

Figure 7.6: Real-space stereographic projection of the molecular orientations in the high-temperature disordered phase of adamantanecarboxylic acid, viewed along the c axis. (a) In the RMC initial configuration, (b) in the RMC refined configuration. Methine carbon: black; acid connected carbon: red.

about its molecular axis; hence the isotropic distribution of orientations perpendicular to the molecular axis shown in figure 7.6(a). However, as shown in figure 7.6(b), two distinct orientations of the adamantanecarboxylic acid dimer emerge during refinement of the high-temperature phase. These two orientations are given by a small rotation of the adamantyl groups about the molecular axis of the dimer, such that the six methine carbons of the two adamantyl groups are positioned in six areas on the edge of a circle. These two molecular orientations can be inferred from the structure that is given by a Rietveld refinement using fractional occupancies, as described in F. Belanger-Gariepy *et al.* [111].

The emergence of these two distinct orientations from an initial configuration with random orientations, while maintaing the molecular structure of an individual adamantanecarboxylic acid dimer, can only be accomplished by the correlated motion of all the constitute atoms of an adamantanecarboxylic acid dimer. The large amount of atomic motion, required by the described molecular rotations, explains the very high number of atomic moves generated before the refinements reached equilibrium (see section 7.5).

Three rotation angles per molecule, measured about the molecular axis, were calculated. These are the angles between the vectors from the centre of mass of the three

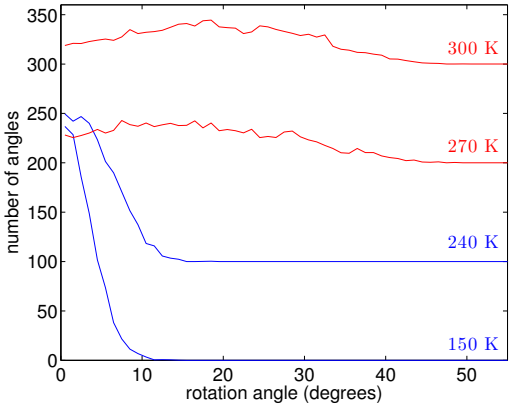

Figure 7.7: Histogram of the rotation angles of individual adamantanecarboxylic acid dimers within an adamantanecarboxylic acid crystal. Low-temperature phase: blue; high-temperature phase: red.

methine carbons to the corresponding methine carbons in the refined RMC configuration and those in the initial configurations. These rotation angles measure the rotation required, about the molecular axis, to map an adamantanecarboxylic acid molecule in the refined RMC configuration onto the corresponding adamantanecarboxylic acid molecule in the initial configuration, a histogram of these angles is shown in figure 7.7.

Figure 7.7 shows large spreads and high mean values in the rotation angles for the two high-temperature phase refinements, 17.8° and 19.6° in the 270 K and 300 K refinements respectively, averaged over six RMC refinements. This indicates molecular rotations, showing a strong preference for adamantanecarboxylic acid dimers in the high-temperature phase to rotate away from the randomly rotated initial configurations, and as shown in figure 7.6 these rotations are towards two molecular orientations. By contrast there is a sharp distribution and low mean values in the rotation angles for the two low-temperature phase refinements, 3.0° and 4.5° in the 150 K and 240 K refinements respectively, averaged over six RMC refinements. These values show that there is no preference for adamantanecarboxylic acid dimers in the low-temperature phase to rotate from the ordered initial configurations, configurations that have the structure given by a conventional Rietveld refinement.

7.7 Conclusions

The study reported in this chapter has examined the localised structural fluctuations in the low- and high-temperature phases of adamantanecarboxylic acid as deduced from reverse Monte Carlo analysis of neutron total scattering. In the high-temperature phase adamantanecarboxylic dimers have been shown to rotate such that they exist in one of two orientations. That the correlated atomic motion required by these molecular rotations are captured by an RMC refinement is further evidence for the potential utility in the application of RMC refinements to the study of disordered molecular materials.

The orientational refinement of the adamantanecarboxylic acid dimers only involves molecular rotations about the molecular axis, not about all three axes as in adamantane. This restricted rotation in adamantanecarboxylic acid is a natural consequence of its dimmer structure, however that these restricted rotations are refined by RMC shows the potential utility in the use of planarity potentials beyond the constraint of planar ring structures. The orientational refinement of adamantanecarboxylic acid molecules about one axis by RMC also shows that there is a strong driving force for this restricted orientational refinement within the experimental data used by RMC.

Chapter 8

Conclusions and Further Work

8.1 Conclusions

Planarity potentials, introduced in chapter 2, have been successfully applied to the RMC refinements of PTP and OTP, presented in chapters 4 and 5, such that the phenyl rings in these materials are kept largely planar during a data-driven atomistic refinement. It has also been shown, through their use in the restraint of carboxylic acid groups during RMC refinements of adamantanecarboxylic acid, presented in chapter 7, that planarity potentials may be applied more generally than just being used to restrain phenyl rings - as they were originally developed to do. These results demonstrate that through the use of planarity restraints, RMC refinements of molecular materials that contain planar groups, with other appropriate intramolecular potentials are capable of producing results consistent with previous experimental and theoretical work. This offers a new method of elucidating the intermolecular correlations of molecular systems that contain planar groups; thereby revealing new structural details of these materials.

RMC refinement of adamantane and adamantanecarboxylic acid, presented in chapters 6 and 7, show molecular rotations. These refinements were performed using the standard RMC methodology, involving the refinement of individual atomic positions; molecular orientations were not themselves refined. Therefore, that molecular rotations were shown in the refinements of adamantane and adamantanecarboxylic acid demonstrates the potential utility in applying the standard RMC methodology to the investigation of orientationally disordered molecular materials.

However, RMC refinements of OTP, presented in chapter 5, do not show any molecular rotations; molecular orientations are not refined. In the glass phase of OTP there is a non-isotropic distribution of molecular orientations in the initial configuration and so orientational refinement is expected. Therefore, as orientational refinement is seen in the RMC of both adamantane and adamantanecarboxylic acid, and expected but not

seen in OTP glass, the question as to the primary differences between the refinements is raised. The reason molecular orientations are not refined in OTP glass could be due to the relative 'featurelessness' of the OTP glass data; the lack of prominent features in the high-r region of the OTP glass PDF compared to the high-r region of the adamantane and adamantanecarboxylic acid PDFs. Therefore, although the standard RMC methodology has utility in the investigation of orientationally disordered molecular materials, it is anticipated that this will only be the case for materials with significant high-r PDF data.

That is not to say that there is no utility in RMC refinements of amorphous molecular materials. aZIF is an amorphous molecular material the RMC refinement of which, presented in chapter 3, appears to reveal the primary mode of flexibility in aZIF. However this flexibility is connected to fluctuations in the position of individual zinc atoms or the small number of atoms in an imidazolate ring, not the cooperative motion of large numbers of atoms required by molecular orientational refinements.

RMC refinements of the high-temperature phase of PTP, presented in chapter 4, produce a unimodal distribution of torsion angles from a bimodal distribution. Whereas, using the same basic RMC methodology, refinements of the high-temperature phase of adamantane and adamantanecarboxylic acid, presented in chapters 6 and 7, produce a bimodal distribution of molecular orientations from a random distribution. It is of note that the RMC refinements presented in this thesis refine these two distributions; away from and towards a bimodal distribution, relating to a displacive and order-disorder phase transition respectively.

8.2 Further Work

As written by the author, planarity potentials, introduced in chapter 2, do not have standard energy units; unlike the bond and angle energy values, D and K in equations 2.29 and 2.30, the plane energy value, P in equation 2.31, is not given in units of eV. Instead the value of P has arbitrary units and its value is determined by considering test refinement of the structure under investigation. These energy values are no more than weighting factors for the given potential and so as long as they are internally consistent their exact units do

not affect the refinements. However, for the wider adoption of planarity potentials within the RMC community, a standard set of values for planarity potentials with units of eV would be beneficial.

Similarly, as written by the author, planarity potentials require a significant amount of coding prior to their use in an RMC refinement and it would be beneficial for the wider adoption of planarity potentials within the RMC community to eliminate this requirement. A planarity file that lists all the planes of atoms to be restrained, analogous to the bond or triplet files for bond or angle potentials [43], must be written. Unlike bond or triplet files the production of a planarity file is not an automated process handled by RMCcreate [5], but they have to be written, by hand, by the user - requiring the coding of an ancillary program prior to refinement. The ancillary programs that do this for PTP, OTP and adamantanecarboxylic acid are given in Appendix C.

ZIF-4, the metal-organic framework material investigated in chapter 3, contains imidazolate rings for which, like the phenyl rings in PTP and OTP, it is energetically favourable to stay planar. This material, and by extension the wider family of ZIF materials, are therefore prime candidates for further investigation through RMC refinement using planarity potentials. Planar atomic structures are very common in a wide range of materials and, as demonstrated by their use in adamantanecarboxylic acid, planarity potentials may be easily applied to any group of atoms. It is therefore anticipated that planarity potentials may be useful for many future structural studies.

Bibliography

[1] J. G. Bednorz and K. A. Müller (1986) Possible high T_c superconductivity in the Ba–La–Cu–O system. *Zeitschrift für Physik B Condensed Matter*, **64**, 189-193

[2] M. K. Wu, J. R. Ashburn, C. J. Torng, P. H. Hor, R. L. Meng, L. Gao, Z. J. Huang, Y. Q. Wang and C. W. Chu (1987) Superconductivity at 93 K in a new mixed-phase Y–Ba–Cu–O compound system at ambient pressure. *Phys. Rev. Lett.*, **58**, 908-910

[3] P. W. Anderson (1987) The resonating valence bond state in La_2CuO_4 and superconductivity. *Science*, **235**, 1196-1198

[4] P. Monthoux, A. V. Balatsky and D. Pines (1991) Toward a theory of high-temperature superconductivity in the antiferromagnetically correlated cuprate oxides. *Phys. Rev. Lett.*, **67**, 3448-3451

[5] M. T. Dove and G. Rigg (2013) RMCgui: A new interface for the workflow associated with running Reverse Monte Carlo simulations. *J. Phys.: Condensed Matter*, **25**, 454222

[6] M. T. Dove (2003) *Structure and Dynamics: An Atomic View of Materials*, Oxford University Press

[7] M. T. Dove (2002) An introduction to the use of neutron scattering methods in mineral sciences. *Eur. J. Mineral.*, **14**, 203-224

[8] C. Giacovazzo (2002) *Fundamentals of Crystallography*, Oxford University Press, Second Edition

[9] C. A. Young and A. L. Goodwin (2011) Applications of pair distribution function methods to contemporary problems in materials chemistry. *J. Mater. Chem.*, **21**, 6464

[10] D. A. Keen, W. Hayes and R. L. Mcgreevy (1990) Structural disorder in AgBr on the approach to melting. *J. Phys.: Condensed Matter*, **2**, 2773-2786

[11] M. T. Dove, D. A. Keen, A. C. Hannon and I. P. Swainson (1997) Direct measurement of the Si–O bond length and orientational disorder in the high-temperature phase of cristobalite. *Phys. Chem. Minerals*, **24**, 311-317

[12] M. G. Tucker, M. T. Dove and D. A. Keen (2000) Simultaneous analysis of changes in long-range and short-range structural order at the displacive phase transition in quartz. *J. Phys.: Condensed Matter*, **12**, L723-L730

[13] M. T. Dove, M. G. Tucker and D. A. Keen (2002) Neutron total scattering method: simultaneous determination of long-range and short-range order in disordered materials.*Eur. J. Mineral.*, 2002, **14**, 331-348

[14] A. L. Goodwin, M. G. Tucker, E. R. Cope, M. T. Dove and D. A. Keen (2005) Model-independent extraction of dynamical information from powder diffraction data. *Phys. Rev. B*, **72**, 214304

[15] J. S. O. Evans (1999) Negative thermal expansion materials. *Dalton Trans.*, 3317-3326

[16] G. D. Barrera, J. A. O. Bruno, T. H. K. Barron and N. L. Allan (2005) Negative thermal expansion. *J. Phys.: Condensed Matter*, **17**, R217-R252

[17] A. J. Fletcher, K. M. Thomas and M. J. Rosseinsky (2005) Flexibility in metal-organic framework materials: Impact on sorption properties. *J. Solid State Chem.*, **178**, 2491-2510

[18] S. T. Bramwell and M. J. P. Gingas (2001) Spin ice state in frustrated magnetic pyrochlore materials. *Science*, **294**, 1495-1501

[19] A. P. Ramirez, A. Hayashi, R. J. Cava, R. Siddharthan and B. S. Shastry (1999) Zero-point entropy in 'spin ice'. *Nature*, **399**, 333-335

[20] S. J. L. Billinge and I. Levin (2007) The problem with determining atomic structure at the nanoscale. *Science*, **316**, 1698

[21] Th. Proffen and S. J. L. Billinge (1999) PDFFIT, a program for full profile structural refinement of the atomic pair distribution function. *J. Appl. Cryst.*, **32**, 303

[22] C L Farrow, P Juhas, J W Liu, D Bryndin, E S Bozin, J Bloch, Th Proffen and S J L Billinge (2007) PDFfit2 and PDFgui: computer programs for studying nanostructure in crystals. *J. Phys.: Condensed Matter*, **19**, 335219

[23] Th. Proffen, R. G. DiFrancesco, S. J. L. Billinge, E. L. Brosha and G. H. Kwei (1999) Measurement of the local Jahn-Teller distortion in $LaMnO_3$.006. *Phys. Rev. B*, **60**,

[24] R L McGreevy and L Pusztai (1988) Reverse Monte Carlo simulation: a new technique for the determination of disordered structures. *Mol Simul*, **1**, 359-367

[25] R. L. McGreevy (1995) RMC - progress, problems and prospects. *Nucl. Instrum. Meth. A*, **354**, 1-16

[26] R. L. McGreevy (2001) Reverse Monte Carlo modelling. *J Phys: Condensed Matter*, **13**, R877-R913

[27] N. Metropolis, A. W. Rosenbluth, M. N. Rosenbluth, A. H. Teller, and E. Teller (1953) Equation of state calculations by fast computing machines. *J. Chem. Phys.*, **21**

[28] Special Feature section (1992) *Neutron News*, **3**, 3

[29] ISIS, Rutherford Appleton Laboratory (2015) How ISIS Works. *http://www.isis.stfc.ac.uk/about/how-isis-works6313.html*

[30] A. C. Hannon (2005) Results on disordered materials from the general materials diffractometer. *Nucl. Instrum. Methods Phys. Res.*, **A551**, 81

[31] ISIS, Rutherford Appleton Laboratory (2015) Gem. *http://www.isis.stfc.ac.uk/instruments/gem/*

[32] ISIS, Rutherford Appleton Laboratory (2015) Polaris. *http://www.isis.stfc.ac.uk/instruments/polaris/*

[33] D. A. Keen (2001) A comparison of various commonly used correlation functions for describing total scattering. *J. Appl. Cryst.*, **34**, 172-177

[34] V. M. Nield and D. A. Keen (2006) *Diffuse Neutron Scattering from Crystalline Materials*, Oxford University Press

[35] A. K. Soper (2011) GudrunN and GudrunX: Programs for correcting raw neutron and X-ray diffraction data to differential scattering cross section, *Tech Rep*, **RAL-TR-2011-013**, Rutherford Appleton Laboratory, Didcot, UK. available at `http://disordmat.moonfruit.com/`

[36] A. K. Soper (2009) Inelasticity corrections for time-of-flight and fixed wavelength neutron diffraction experiments. *Mol. Phys.*, **107**, 1667-1684

[37] E. Lorch (1969) Neutron diffraction by germania silica and radiation-damaged silica glasses. *J. Phys. C: Solid State Phys.*, **2**, 229-237

[38] A. C. Larson and R. B. Von Dreele (1994) General Structure Analysis System (GSAS) *Los Alamos National Laboratory Report LAUR 86-748*

[39] B. H. Toby (2001) EXPGUI, a graphical user interface for GSAS *J .Appl. Cryst.*, **34**, 210–213

[40] H. M. Rietveld (1969) A profile refinement method for nuclear and magnetic structures. *J. Appl. Cryst.*, **2**, 64

[41] M. G. Tucker, D. A. Keen, M. T. Dove, A. L. Goodwin and Q. Hui (2007) RMCProfile: reverse Monte Carlo for polycrystalline materials. *J Phys: Condensed Matter*, **19**, 335218

[42] N. L. Allinger, Y. H. Yuh, and J. H. Lii (1989) Molecular mechanics. The MM3 force field for hydrocarbons. 1. *J. Am. Chem. Soc.*, **111**, 8551–8566.

[43] M. G. Tucker, M. T. Dove, A. L. Goodwin and D. A. Keen (2012) RMCProfile user manual, code version 6.5.0. *http://www.rmcprofile.org/Manuals*

[44] Geometric Tools, LLC (2015) Least Squares Fitting of Data. *http://www.geometrictools.com/Documentation/LeastSquaresFitting.pdf*

[45] C. N. R. Rao, A. K. Cheetham and A. Thirumurugan (2008) Hybrid inorganic-organic materials: a new family in condensed matter physics. *J Phys: Condensed Matter*, **20**, 083202

[46] G. Férey (2009) Some suggested perspectives for multifunctional hybrid porous solids. *Dalton Trans.*, **23**, 4400

[47] H-C Zhou, J. R. Long and O. M. Yaghi (2012) Introduction to metal-organic frameworks. *Chem. Rev.*, **112**, 673-674

[48] N. Stock and S. Biswas (2012) Synthesis of metal-organic frameworks (MOFs): routes to various MOF topologies, morphologies, and composites. *Chem. Rev.*, **112**, 933-969

[49] K. Sumida, D. L. Rogow, J. A. Mason, T. M. McDonald, E. D. Bloch, Z. R. Herm, T-H Bae and J. R. Long (2012) Carbon dioxide capture in metal-organic frameworks. *Chem. Rev.*, **112**, 724-781

[50] M. P. Suh, H. J. Park, T. K. Prasad, and D-W Lim (2012) Hydrogen storage in metal-organic frameworks. *Chem. Rev.*, **112**, 782-835

[51] L. J. Murray, M. Dinca and J. R. Long (2009) Hydrogen storage in metal-organic frameworks. *Chem. Soc. Rev.*, **38**, 1294-1314

[52] J-R Li, J. Sculley, and H-C Zhou (2012) Metal-organic frameworks for separations. *Chem. Rev.*, **112**, 869-932

[53] J-R Li, R. J. Kuppler and H-C Zhou (2009) Selective gas adsorption and separation in metal-organic frameworks. *Chem. Soc. Rev.*, **38**, 1477-1504

[54] M. Yoon, R. Srirambalaji, and K. Kim (2012) Homochiral metal-organic frameworks for asymmetric heterogeneous catalysis. *Chem. Rev.*, **112**, 1196-1231

[55] J. Lee, O. K. Farha, J. Roberts, K. A. Scheidt, S. T. Nguyen and J. T. Hupp (2009) Metal-organic framework materials as catalysts. *Chem. Soc. Rev.*, **38**, 1450-1459

[56] M. Kurmoo (2009) Magnetic metal-organic frameworks. *Chem. Soc. Rev.*, **38**, 1353-1379

[57] M. D. Allendorf, C. A. Bauer, R. K. Bhaktaa and R. J. T. Houka (2009) Luminescent metal-organic frameworks. *Chem. Soc. Rev.*, **38**, 1330-1352

[58] Y. Cui, Y. Yue, G. Qian and B. Chen (2012) Luminescent functional metal-organic frameworks. *Chem. Rev.*, **112**, 1126-1162

[59] A. Phan, C. J. Doonan, F. J. Uribe-Romo, C. B. Knobler, M. O'Keeffe and O. M. Yaghi (2010) Synthesis, structure, and carbon dioxide capture properties of zeolitic imidazolate frameworks. *Accounts of Chemical Research*, **43**, 58-67

[60] K. S. Park, Z. Ni, A. P. Cote, J. Y. Choi, R. Huang, F. J. Uribe-Romo, H. K. Chae, M. O'Keeffe, and O. M. Yaghi (2006) Exceptional chemical and thermal stability of zeolitic imidazolate frameworks. *Proc. Natl. Acad. Sci. U.S.A.*, **103**, 10186-10191

[61] R. Banerjee, A. Phan, B. Wang, C. Knobler, H. Furukawa, M. O'Keeffe and O. M. Yaghi (2008) High-throughput synthesis of zeolitic imidazolate frameworks and application to CO_2 capture *Science*, **319**, 939

[62] T. D. Bennett, P. Simoncic, S. A. Moggach, F. Gozzo, P. Macchi, D. A. Keen, J-C Tan and A. K. Cheetham (2011) Reversible pressure-induced amorphization of a zeolitic imidazolate framework (ZIF-4). *Chem. Comm.*, **47**, 7983-7985

[63] K. D. Hammonds, M. T. Dove, A. P. Giddy, V. Heine and B. Winkler (1996) Rigid unit phonon modes and structural phase transitions in framework silicates. *American Mineralogist*, **81**, 1057–1079

[64] A. L. Goodwin (2006) Rigid unit modes and intrinsic flexibility in linearly bridged framework structures. *Phys. Rev.*, **B74**, 134302

[65] S. K. Park, Z. Ni, A. P. Côté, J. Y. Choi, R. D. Huang, F. J. Uribe-Romo, H. K. Chae, M. O'Keeffe, O. M. Yaghi (2006) Exceptional chemical and thermal stability of zeolitic imidazolate frameworks. *Proc. Natl. Acad. Sci. U.S.A.* **103**, 10186

[66] T. D. Bennett, A. L. Goodwin, M. T. Dove, D. A. Keen, M. G. Tucker, E. R. Barney, A. K. Soper, E. G. Bithell, J-C Tan and A. K. Cheetham (2010) Structure and properties of an amorphous metal-organic framework. *Phys. Rev. Lett.* **104**, 115503

[67] R. Lehnert and F. Seel (1980) Preparation and crystal structure of the Manganese (II) and Zinc (II) derivative of imidazole. *Z. Anorg. Allg. Chem.* **464**, 187

[68] D. W. Lewis, A. R. Ruiz-Salvador, A. Gomez, L. M. Rodriguez-Albelo, F. X. Coudert, B. Slater, A. K. Cheetham and C. Mellot-Draznieks (2009) Zeolitic imidazole frameworks: structural and energetics trends compared with their zeolite analogues. *Cryst. Eng. Comm.* **11**, 2272

[69] M. G. Tucker, D. A. Keen, M. T. Dove, and K. Trachenko (2005) Refinement of the Si–O–Si bond angle distribution in vitreous silica. *J. Phys.: Condensed Matter*, **17**, 57–575.

[70] P. Bordat and R. Brown (1999) A molecular model of *para*-terphenyl and its disorder-order transition. *Chemical Physics*, **246**, 323-334

[71] J. L. Baudour (1991) Potential barrier heights in crystalline polyphenyls and in gaseous biphenyl determined uniquely from diffraction data. *Acta Cryst. sect. B*,**47**, 935-949

[72] H. M. Rietveld, E. N. Maslen and C. J. B. Clews (1970) An X-ray and neutron diffraction refinement of the structure of *para*-terphenyl. *Acta Cryst. sect. B*,**26**, 693

[73] J. L. Baudour, H. Cailleau and W. B. Yelon (1977) Double-Well potential in the disordered phase of *para*-terphenyl from neutron (200 K) and X-ray (room-temperature) diffraction data. *Acta Cryst. sect. B*,**33**, 1733

[74] J. L. Baudour, Y. Delugeard H. Cailleau (1976) Structural transition in polyphenyls: I. crystal structure of the low temperature phase of *para*-terphenyl at 113 K. *Acta Cryst. sect. B*,**32**, 150

[75] D. J. Goossens, and M. J. Gutmann (2009) Revealing how interactions lead to ordering in *para*-terphenyl. *Phys. Rev. Let.*, **102**, 015505

[76] D. J. Goossens (2010) Approaches to modeling diffuse scattering from molecular crystals: *para*-terphenyl ($C_{18}H_{14}$). *Physical metallurgy and material science*, **41**, 1119-1129

[77] A. Baranyal and T. R. Welberry (1992) Molecular dynamics simulation study of solid polyphenyls: structure determined by the interplay between intra- and intermolecular forces. *Materials Physics*,**73**, 867-879

[78] B. Schatschneider and E. L. Chronister (2011) Molecular simulation of the pressure-induced crystallographic phase transition of *para*-terphenyl. *J. Phys. Chem*,**115**, 407-413

[79] M. T. Dove (1997) Theory of displacive phase transitions in minerals. *American Mineralogist*, **82**, 213-244

[80] W. Klement, R. H. Willens, and P. Duwez (1960) Non-crystalline structure in solidified gold-silicon alloys. *Nature*, **187**, 869

[81] C. Suryanarayana, I. Seki, and A. Inoue (2009) A critical analysis of the glass-forming ability of alloys. *J. of Non-Crystalline Solids*, **355**, 355-360

[82] L. Yu (2001) Amorphous pharmaceutical solids: preparation, characterization and stabilization. *Advanced Drug Delivery Reviews*, **48**, 27-42

[83] C. D. Dimitrakopoulos and D. J. Mascaro (2001) Organic thin-film transistors: a review of recent advances. *IBM J. Res. & Dev.*, **45**, 11-26

[84] A. Tolle, H. Schober, J. Wuttke, F. Fujara (1997) Coherent dynamic structure factor of *ortho*-terphenyl around the mode coupling crossover temperature T_c. *Phys. Rev. E*, **56**, 809

[85] G. M. Brown and H. A. Levy (1979) *Ortho*-terphenyl by neutron diffraction. *Acta Cryst. sect. B*, **35**, 785-788

[86] S. Aikawa, Y. Maruyama, Y. Ohashi and Y. Sasada (1978) 1,2-Diphenylbenzene (*ortho*-erphenyl). *Acta Cryst. sect. B*, **34**, 2901-2904

[87] J. N. Andrews and A. R. Ubbelohde (1955) Melting and crystal structure: the melting parameters of some polyphenyls. *Proc. R. Soc. Lond. A*, **228**

[88] R. J. Greet and D. Turnbull (1967) Glass transition in *ortho*-terphenyl. *J. Chem. Phys.*, **46**, 1243

[89] W. Ping, D. Paraska, R. Baker, P. Harrowell and C. A. Angell (2011) Molecular engineering of the glass transition: glass-forming ability across a homologous series of cyclic stilbenes. *J. Phys. Chem. B*, **115**, 4696-4702

[90] A. Tolle (2001) Neutron scattering studies of the model glass former *ortho*-terphenyl. *Rep. Prog. Phys.*, **64**, 1473-1532

[91] I. T. Todorov, W. Smith, K. Trachenko, M. T. Dove (2006) DL_POLY_3: new dimensions in molecular dynamics simulations via massive parallelism. *J. Mater. Chem.*, **16**, 1911-1918

[92] D. E. Williams (2001) Improved intermolecular force field for molecules containing H, C, N, and O atoms, with application to nucleoside and peptide crystal. *J. Comput. Chem.*, **22**, 1154-1166

[93] R. C. Fort, Jr. and P. von R. Schleyer (1964) Adamantane: consequences of the dimondoid structure. *Chem. Rev.*, **64**, 277-300

[94] G. Ali Mansoori (2007) Dimondoid molecules. *Advances in Chemical Physics*, **136**, 207-258

[95] C. E. Nordman and D. L. SchmItkons (1965) Phase transition and crystal structures of adamantane. *Acta Cryst.*, **18**, 764-767

[96] J. P. Amoureux and M. Bee (1980) A cubic harmonic analysis of the plastic crystal structures of adamantane, $C_{10}H_{16}$, and adamantanone, $C_{10}H_{14}O$, at room temperature. *Acta Cryst. sect. B*, **36**, 2636-2646

[97] S-S Chang and E. F. Westrum (1960) Heat capacites and thermodynamic properties of globular molecules, I. adamantane and hexamethylenetetramine. *J. Phys. Chem.*, **64**, 1547

[98] D. W. McCall and D. C. Douglass (1960) Nuclear magnetic resonance in solid adamantane. *J. Chem. Phys*, **33**, 777

[99] J. Donohue and S. H. Goodman (1967) The crystal structure of adamantane: an example of a false minimum in least squares. *Acta Cryst.*, **22**, 352

[100] V. Vijayakumar, A. B. Garg, B. K. Godwal and S. K. Sikka (2001) Pressure induced phase transitions and equation of state of adamantane. *J. Phys.: Condensed Matter*, **13**, 1961-1972

[101] V. Vijayakumar, A. B. Garg, B. K. Godwal and S. K. Sikka (2000) High-pressure phase transitions in adamantane. *Chemical Physics Letters*, **330**, 275-280

[102] T. Ixo (1973) Pressure-induced phase transition in adamantane. *Acta Cryst. sect. B*, **29**, 364

[103] S. M. Breitling, A. D. Jones and R. H. Boyd (1971) Compressive behaviour of some globular hydrocarbons and their effective intermolecular interaction potentials. *J. Chem. Phys.*, **54**, 3959

[104] G Ciccotti, E. Memeo, M. Ferrario and M. Meyer (1987) Structural transition on cooling of plastic adamantane: a molecular-dynamics study. *Phys Rev Let.*, **59**, 22

[105] T. Clark, T. Mc. O. Knox, H. Mackle and M. A. McKervey (1977) Order-Disorder transitions in substituted adamantanes. *J. Chem. Soc. Faraday Trans. 1*, **73**, 1224

[106] R. M. Paroli, N. T. Kawai, I. S. Butler and D. F. R. Gilson (1988) Phase transitions in adamantane derivatives: 2-chloroadamantane. *Can. J. Chem.*, **66**, 1973

[107] N. T. Kawai, D. F. R. Gilson and I. S. Butler (1991) Phase transitions in adamantane derivatives: 1-fluoroadamantane. *Can. J. Chem.*, **69**, 1758

[108] P. D. Harvey, D. F. R. Gilson and I. S. Butler (1987) Phase transitions and molecular motions in adamantane derivatives : 1 -adamantanol. *Can. J. Chem.*, **65**, 1757

[109] P. D. Harvey, D. F. R. Gilson and I. S. Butler (1987) A study of the phase transition and molecular motion in adamantanamine hydrochloride. *J. Phys. Chem.*, **91**, 1267-1270

[110] P. D. Harvey, D. F. R. Gilson and I. S. Butler (1986) Phase Transitions in adamantane derivatives: adamantanecarboxylic acid. *J. Phys. Chem*, **90**, 139-139

[111] F. Belanger-Gariepy, F. Brisse, P. D. Harvey, D. F. R. Gilson and I. S. Butler (1990) The crystal and molecular structures of adamantanecarboxylic acid at 173 and 280 K. *Can. J. Chem.*, **68**, 1163

[112] E. V. Shevchenko, D. V. Talapin, A. L. Rogach, A. Kornowski, M. Haase and H. Weller (2002) Colloidal synthesis and self-assembly of $CoPt_3$ nanocrystals. *J. Am. Chem. Soc.*, **124**, 11480-11485

Appendix A - GSAS

ZIF

Phase	temperatures (K)	crystallographic axis					
		a (Å)	σ	b (Å)	σ	c (Å)	σ
ZIF-zni	298	23.450	0.0288	23.450	0.0288	12.379	0.0267
ZIF-zni	406	23.486	0.0164	23.486	0.0164	12.369	0.0131
ZIF-zni	540	23.541	0.0161	23.541	0.0161	12.366	0.0111
ZIF-zni	673	23.604	0.0151	23.604	0.0151	12.363	0.0092
ZIF-4	478	15.559	0.0005	15.696	0.0005	18.031	0.0010

Table A.1: Unit cell dimensions given by the GSAS refinements of the crystalline phases of $Zn(Im)_2$, ZIF-zni and ZIF-4.

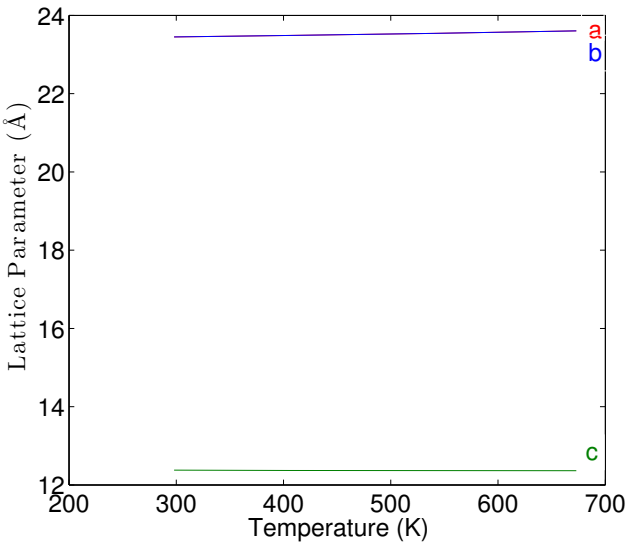

Figure A.1: Thermal variation of the lattice parameters of ZIF-zni. Red: a axis; blue: b axis; green: c axis.

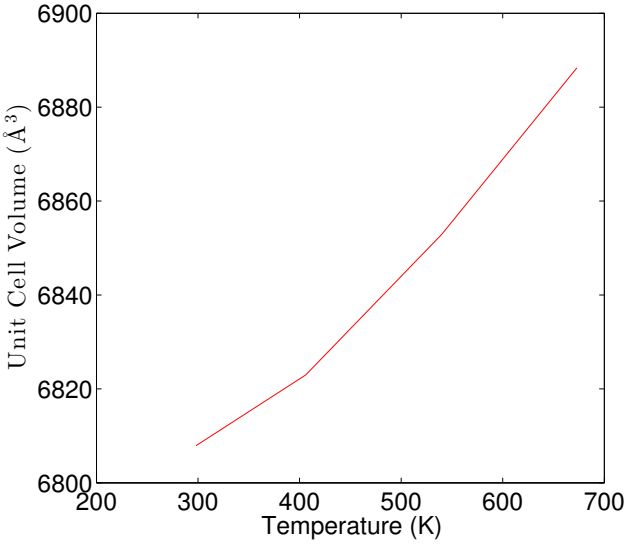

Figure A.2: Thermal variation of the unit cell volume of ZIF-zni.

Phase	temperatures (K)	Rwp	Rp	χ^2	var
ZIF-zni	298	0.1363	0.0899	12.99	150
ZIF-zni	406	0.0891	0.0639	4.976	140
ZIF-zni	540	0.0825	0.0537	2.700	150
ZIF-zni	673	0.0965	0.0561	3.445	144
ZIF-4	478	0.0361	0.0302	0.680	93

Table A.2: Rietveld refinement residuals for the crystalline phases of $Zn(Im)_2$.

ZIF-zni

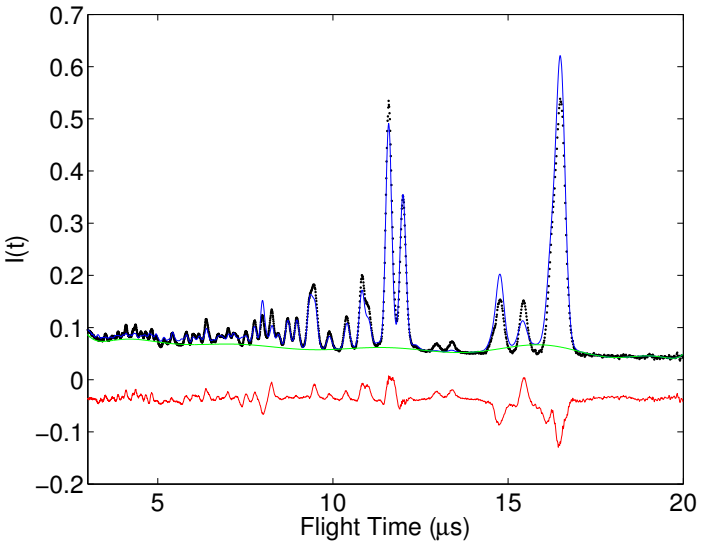

Figure A.3: GSAS fit for ZIF-zni at 298 K, background fit with a 10 term Chebyshev polynomial ($2\theta = 35°$). Experimental data: black dots; GSAS fits: blue line; background: green line; difference: red line.

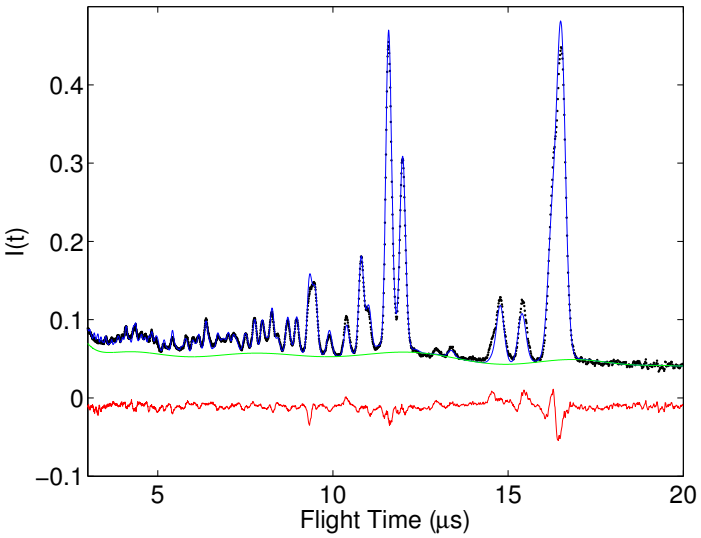

Figure A.4: GSAS fit for ZIF-zni at 406 K, background fit with a 10 term Chebyshev polynomial ($2\theta = 35°$). Experimental data: black dots; GSAS fits: blue line; background: green line; difference: red line.

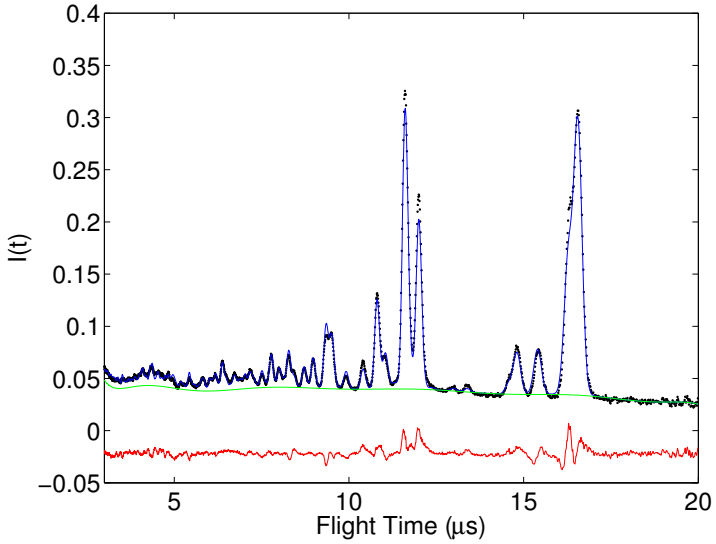

Figure A.5: GSAS fit for ZIF-zni at 540 K, background fit with a 10 term Chebyshev polynomial ($2\theta = 35°$). Experimental data: black dots; GSAS fits: blue line; background: green line; difference: red line.

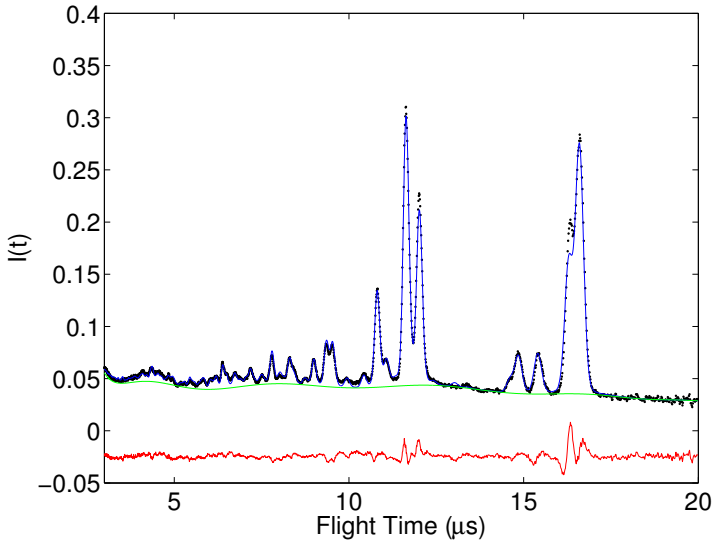

Figure A.6: GSAS fit for ZIF-zni at 673 K, background fit with a 10 term Chebyshev polynomial ($2\theta = 35°$). Experimental data: black dots; GSAS fits: blue line; background: green line; difference: red line.

ZIF-4

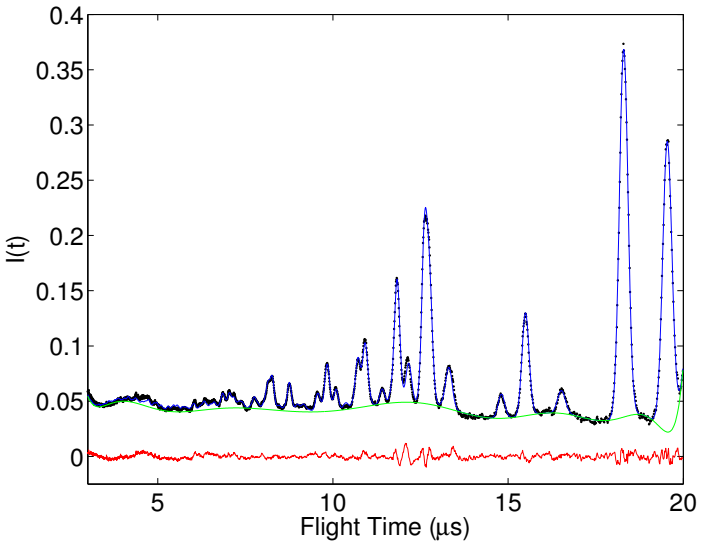

Figure A.7: GSAS fit for ZIF-4 at 478 K, background fit with a 16 term Chebyshev polynomial ($2\theta = 35°$). Experimental data: black dots; GSAS fits: blue line; background: green line; difference: red line.

PTP

temperatures (K)	crystallographic axis					
	a (Å)	σ	b (Å)	σ	c (Å)	σ
10	15.901	0.0004	11.033	0.0003	13.544	0.0005
65	15.942	0.0003	11.050	0.0004	13.553	0.0005
125	16.012	0.0004	11.083	0.0003	13.569	0.0005
150	16.035	0.0004	11.102	0.0003	13.575	0.0005
165	16.041	0.0004	11.116	0.0003	13.579	0.0005
185	8.0160	0.0002	5.5720	0.0002	13.588	0.0006
250	8.0460	0.0002	5.5950	0.0002	13.596	0.0007
290	8.0840	0.0004	5.6095	0.0003	13.611	0.0008

Table A.3: Unit cell dimensions given by the GSAS refinements of the crystalline phases of PTP.

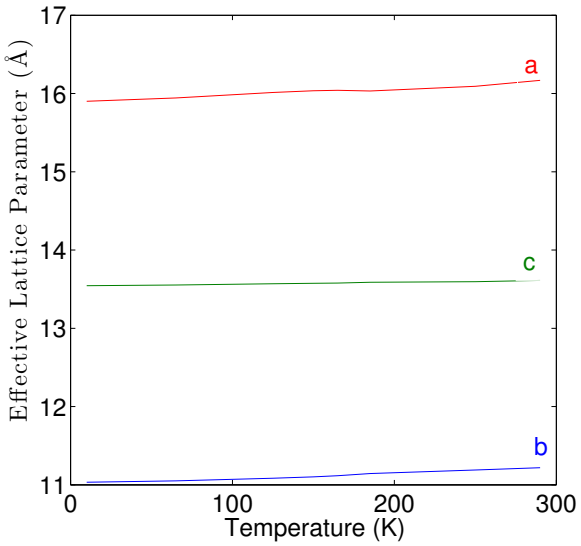

Figure A.8: Thermal variation of the effective lattice parameters of PTP, $a_{\text{monoclinic}} \simeq \frac{1}{2}a_{\text{triclinic}}$, $b_{\text{monoclinic}} \simeq \frac{1}{2}b_{\text{triclinic}}$. Red: a axis; blue: b axis; green: c axis.

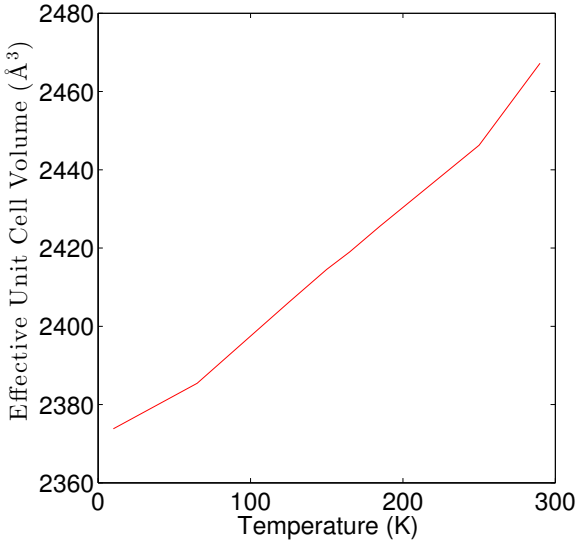

Figure A.9: Thermal variation of the effective unit cell volume of PTP, $V_{\text{monoclinic}} \simeq \frac{1}{4} V_{\text{triclinic}}$.

temperatures (K)	angles					
	α (°)	σ	β (°)	σ	γ (°)	σ
10	89.646	0.003	92.463	0.003	90.016	0.004
65	89.662	0.003	92.424	0.003	90.011	0.004
125	89.703	0.004	92.341	0.003	90.011	0.005
150	89.743	0.004	92.313	0.003	90.020	0.005
165	89.793	0.005	92.306	0.003	90.016	0.007
185	90.000	0.000	92.310	0.004	90.000	0.000
250	90.000	0.000	92.236	0.004	90.000	0.000
290	90.000	0.000	92.130	0.005	90.000	0.000

Table A.4: Unit cell angles given by the GSAS refinements of the crystalline phases of PTP.

temperatures (K)	Rwp	Rp	χ^2	var
10	0.0628	0.0651	1.4140	76
65	0.0593	0.0593	0.3944	76
125	0.0586	0.0542	0.3695	76
150	0.0535	0.0513	0.3090	76
165	0.0548	0.0534	0.3176	76
185	0.0791	0.0644	0.3807	63
250	0.0603	0.0579	0.3646	80
290	0.0750	0.0616	123.10	68

Table A.5: Rietveld refinement residuals for PTP.

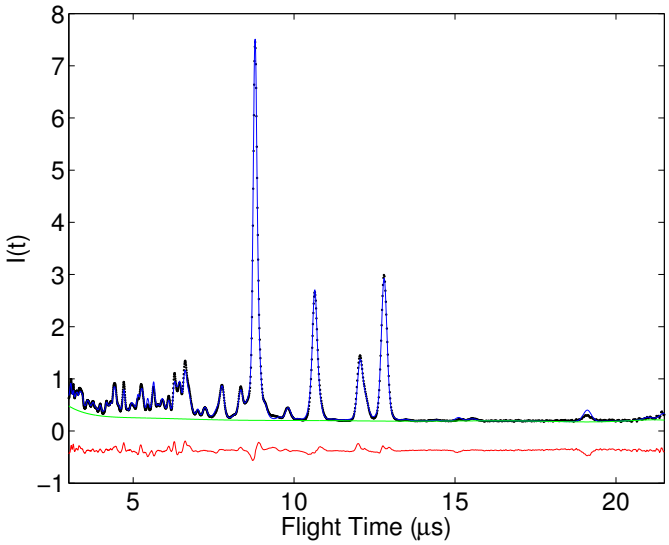

Figure A.10: GSAS fit for PTP at 10 K, background fit with a 10 term Chebyshev polynomial ($2\theta = 35°$). Experimental data: black dots; GSAS fits: blue line; background: green line; difference: red line.

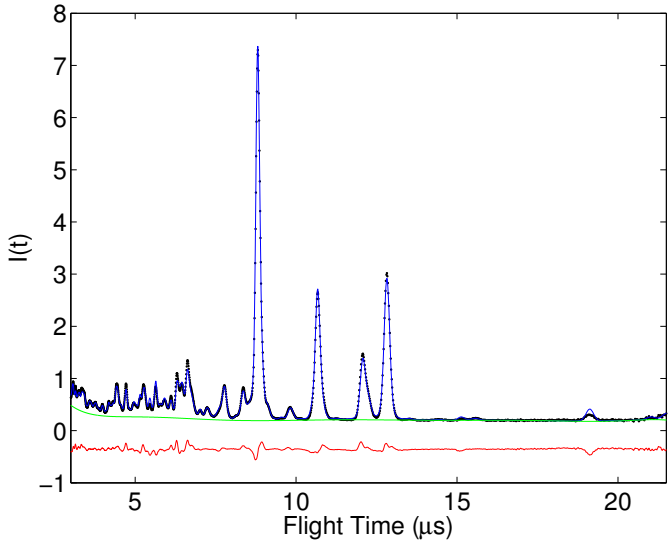

Figure A.11: GSAS fit for PTP at 65 K, background fit with a 10 term Chebyshev polynomial ($2\theta = 35°$). Experimental data: black dots; GSAS fits: blue line; background: green line; difference: red line.

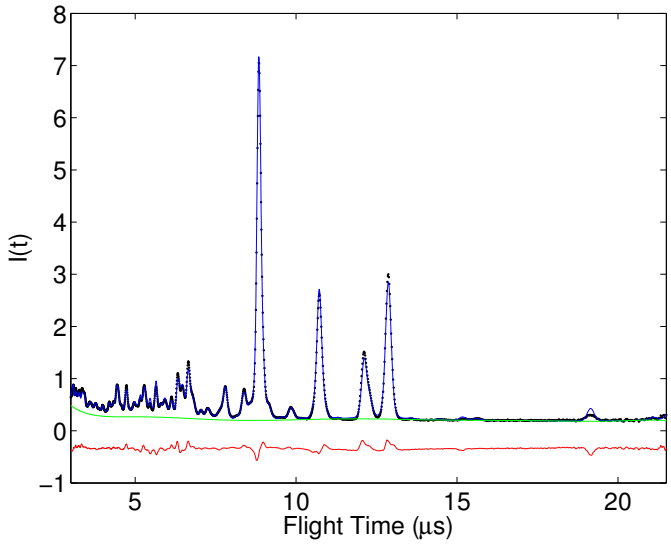

Figure A.12: GSAS fit for PTP at 125 K, background fit with a 10 term Chebyshev polynomial ($2\theta = 35°$). Experimental data: black dots; GSAS fits: blue line; background: green line; difference: red line.

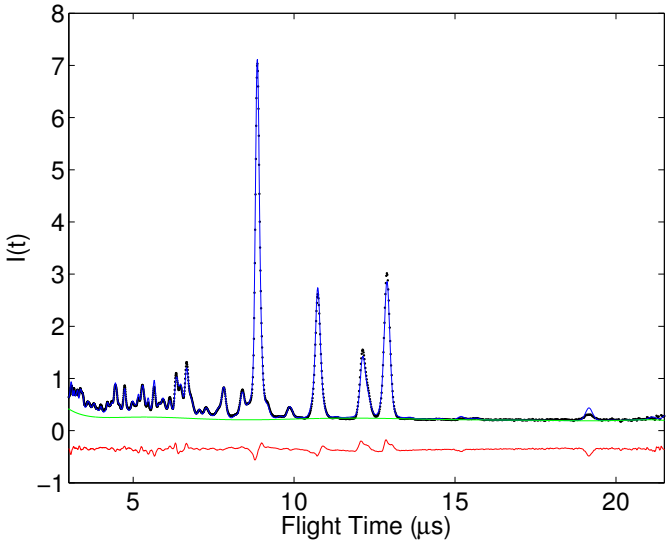

Figure A.13: GSAS fit for PTP at 150 K, background fit with a 10 term Chebyshev polynomial ($2\theta = 35°$). Experimental data: black dots; GSAS fits: blue line; background: green line; difference: red line.

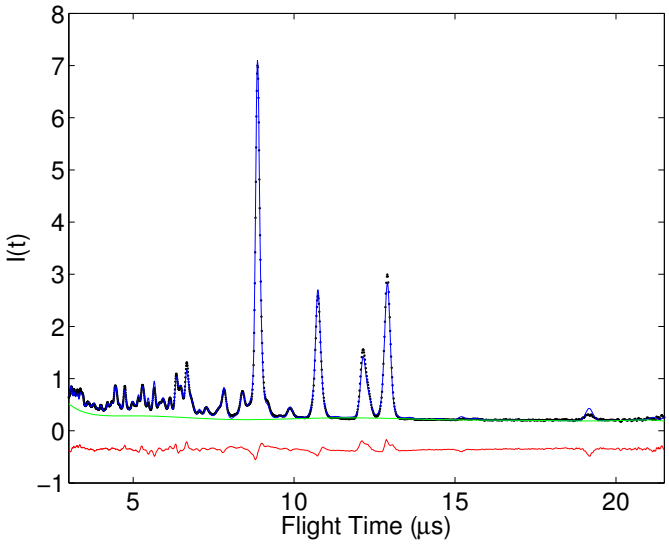

Figure A.14: GSAS fit for PTP at 165 K, background fit with a 10 term Chebyshev polynomial ($2\theta = 35°$). Experimental data: black dots; GSAS fits: blue line; background: green line; difference: red line.

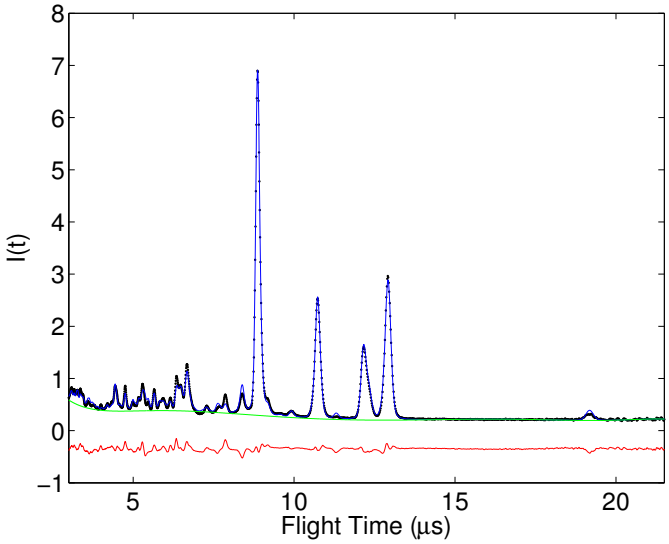

Figure A.15: GSAS fit for PTP at 185 K, background fit with a 10 term Chebyshev polynomial ($2\theta = 35°$). Experimental data: black dots; GSAS fits: blue line; background: green line; difference: red line.

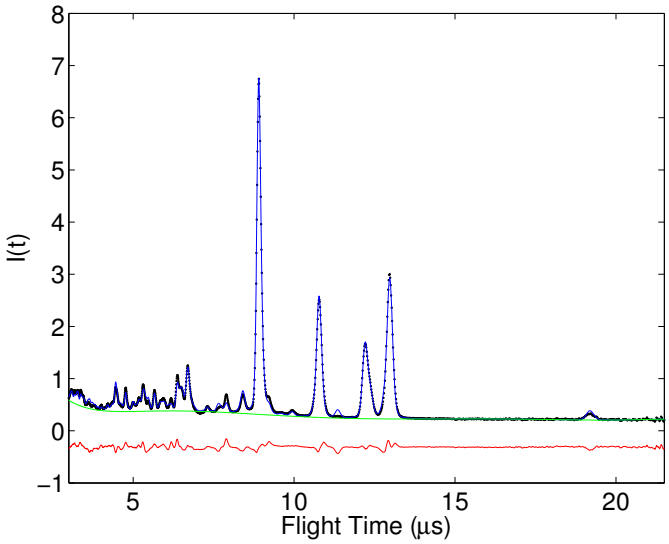

Figure A.16: GSAS fit for PTP at 250 K, background fit with a 10 term Chebyshev polynomial ($2\theta = 35°$). Experimental data: black dots; GSAS fits: blue line; background: green line; difference: red line.

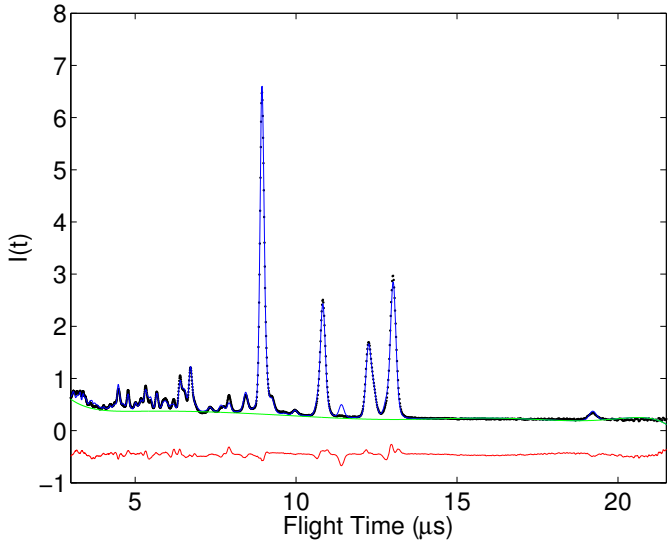

Figure A.17: GSAS fit for PTP at 290 K, background fit with a 10 term Chebyshev polynomial ($2\theta = 35°$). Experimental data: black dots; GSAS fits: blue line; background: green line; difference: red line.

OTP

temperatures (K)	crystallographic axis					
	a (Å)	σ	b (Å)	σ	c (Å)	σ
16	18.547	0.001	5.8174	0.0003	11.540	0.0006

Table A.6: Lattice dimensions given by the GSAS refinement of the crystalline phase of OTP.

temperatures (K)	Rwp	Rp	χ^2	var
16	0.0429	0.0367	0.2681	103

Table A.7: Rietveld refinement residuals for OTP.

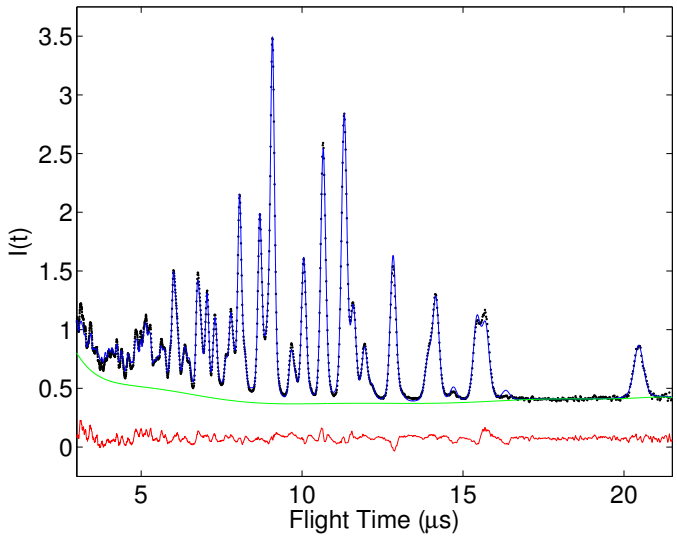

Figure A.18: GSAS fit for crystalline OTP, background fit with a 10 term Chebyshev polynomial ($2\theta = 35°$). Experimental data: black dots; GSAS fits: blue line; background: green line; difference: red line.

Adamantane

temperatures (K)	crystallographic axis					
	a (Å)	σ	b (Å)	σ	c (Å)	σ
100	6.620	0.00020	6.620	0.00020	8.831	0.00030
198	6.654	0.00020	6.654	0.00020	8.946	0.00030
218	9.359	0.00005	9.359	0.00005	9.359	0.00005
258	9.399	0.00005	9.399	0.00005	9.399	0.00005

Table A.8: Unit cell dimensions given by the GSAS refinements of the crystalline phase of adamantane.

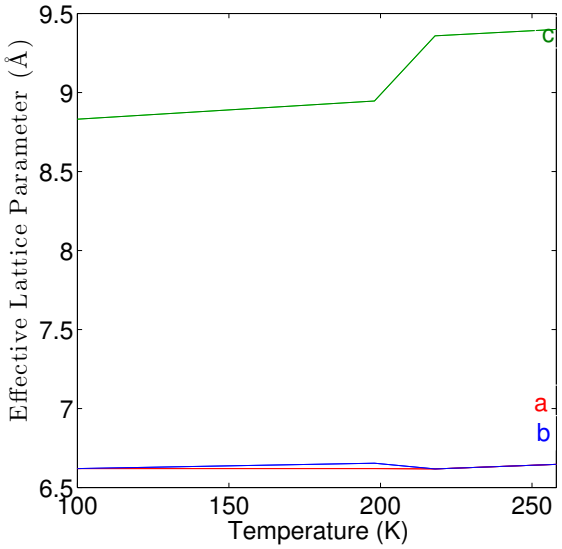

Figure A.19: Thermal variation of the effective lattice parameters of adamantane, $a_{\text{tetragonal}} \simeq \frac{1}{\sqrt{2}} a_{\text{cubic}}$, $b_{\text{tetragonal}} \simeq \frac{1}{\sqrt{2}} b_{\text{cubic}}$. Red: a axis; blue: b axis; green: c axis.

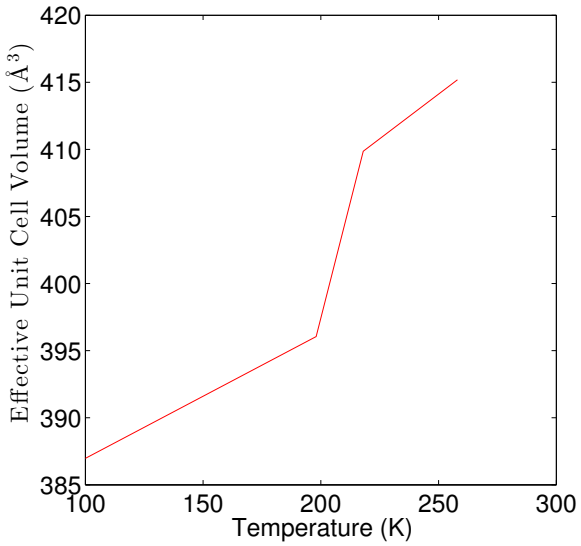

Figure A.20: Thermal variation of the effective unit cell volume of adamantane, $V_{\text{tetragonal}} \simeq \frac{1}{2}V_{\text{cubic}}$.

temperatures (K)	Rwp	Rp	χ^2	var
100	0.0330	0.0284	0.2934	102
198	0.0309	0.0299	0.2925	102
218	0.0524	0.0290	0.9779	6
258	0.0516	0.0302	1.0050	6

Table A.9: Rietveld/Le Bail refinement residuals for adamantane.

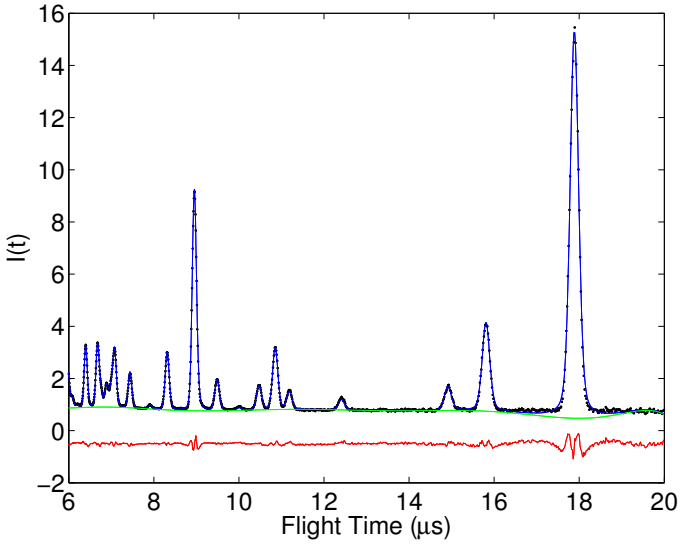

Figure A.21: GSAS fit for adamantane at 100 K, background fit with a 10 term Chebyshev polynomial ($2\theta = 52°$). Experimental data: black dots; GSAS fits: blue line; background: green line; difference: red line.

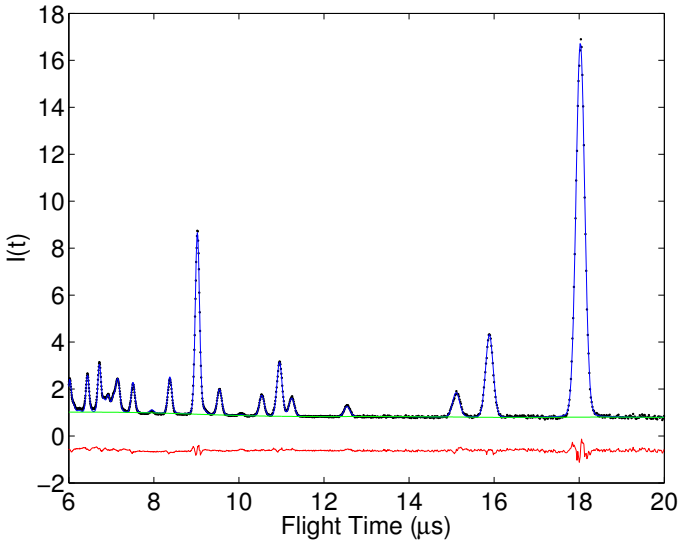

Figure A.22: GSAS fit for adamantane at 198 K, background fit with a 10 term Chebyshev polynomial ($2\theta = 52°$). Experimental data: black dots; GSAS fits: blue line; background: green line; difference: red line.

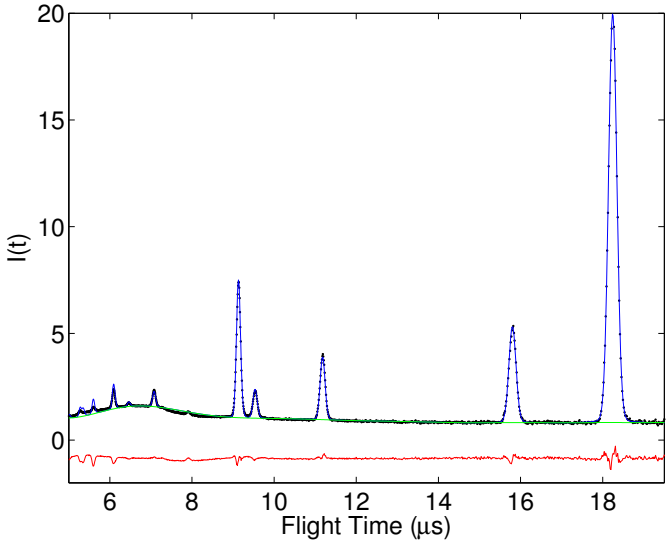

Figure A.23: GSAS fit for adamantane at 218 K, background fit with a 10 term Chebyshev polynomial ($2\theta = 52°$). Experimental data: black dots; GSAS fits: blue line; background; green line; difference: red line.

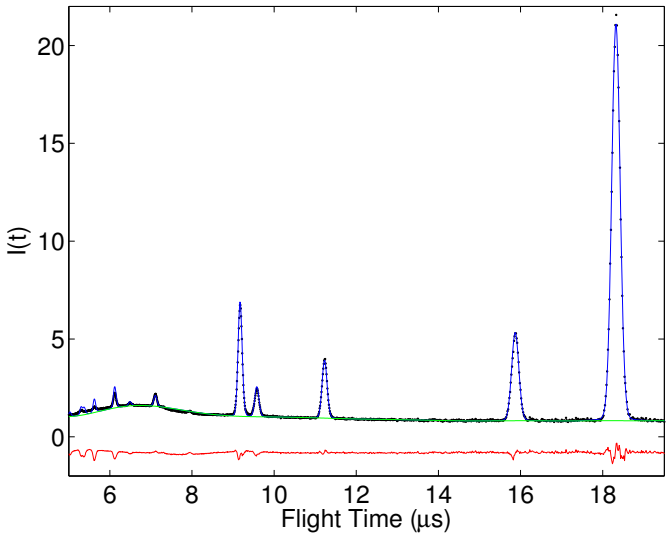

Figure A.24: GSAS fit for adamantane at 258 K, background fit with a 10 term Chebyshev polynomial ($2\theta = 52°$). Experimental data: black dots; GSAS fits: blue line; background: green line; difference: red line.

Adamantanecarboxylic acid

temperatures (K)	crystallographic axis					
	a (Å)	σ	b (Å)	σ	c (Å)	σ
150	6.484	0.0019	6.715	0.0020	11.548	0.0012
240	6.522	0.0019	6.772	0.0022	11.628	0.0012
270	6.494	0.0015	6.841	0.0019	11.634	0.0014
300	6.479	0.0018	6.868	0.0018	11.646	0.0014

Table A.10: Unit cell dimensions given by the GSAS refinements of the crystalline phase of adamantanecarboxylic acid.

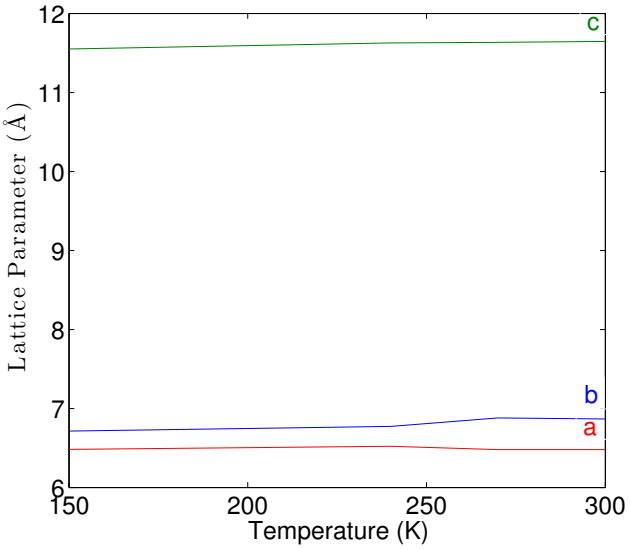

Figure A.25: Thermal variation of the lattice parameters of adamantanecarboxylic acid. Red: a axis; blue: b axis; green: c axis.

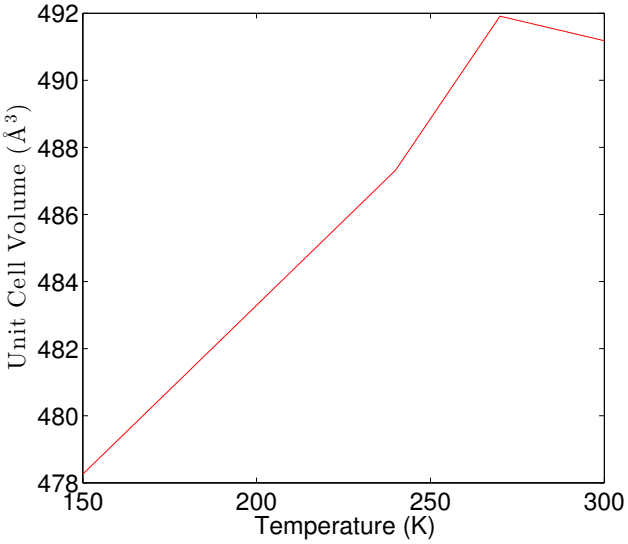

Figure A.26: Thermal variation of the unit cell volume of adamantanecarboxylic acid.

temperatures (K)	angles					
	α (°)	σ	β (°)	σ	γ (°)	σ
150	80.833	0.028	87.131	0.057	74.481	0.054
240	80.006	0.024	86.782	0.042	74.456	0.051
270	77.502	0.026	85.944	0.029	76.285	0.029
300	77.332	0.027	85.822	0.020	76.335	0.053

Table A.11: Unit cell angles given by the GSAS refinements of the crystalline phases of adamantanecarboxylic acid.

temperatures (K)	Rwp	Rp	χ^2	var
150	0.0277	0.0183	0.2981	34
240	0.0270	0.0179	0.2962	34
270	0.0302	0.0185	0.3662	11
300	0.0445	0.0318	0.2958	11

Table A.12: Rietveld/Le Bail refinement residuals for adamantanecarboxylic acid.

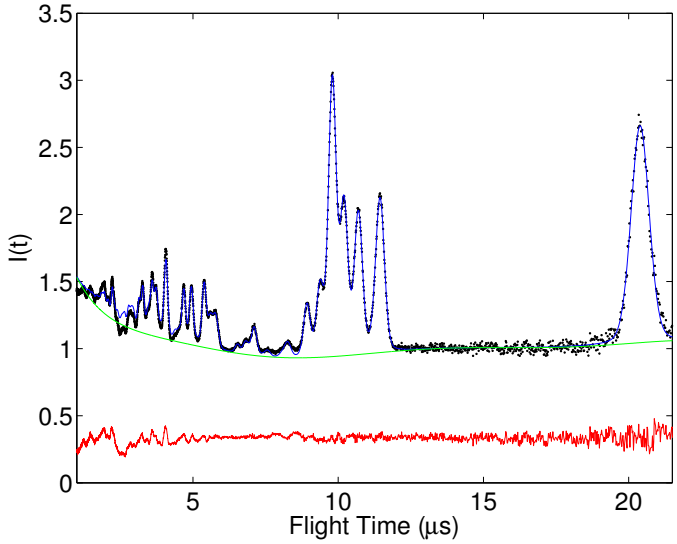

Figure A.27: GSAS fit for adamantanecarboxylic acid at 150 K, background fit with a 10 term Chebyshev polynomial ($2\theta = 26°$). Experimental data: black dots; GSAS fits: blue line; background: green line; difference: red line.

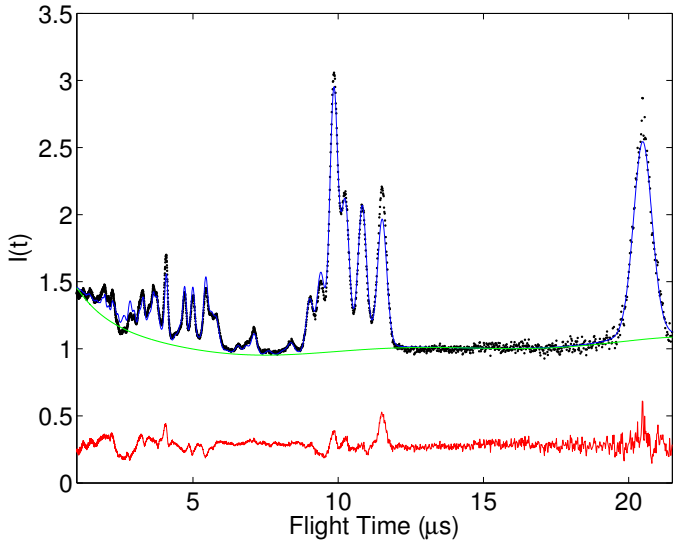

Figure A.28: GSAS fit for adamantanecarboxylic acid at 240 K, background fit with a 10 term Chebyshev polynomial ($2\theta = 26°$). Experimental data: black dots; GSAS fits: blue line; background: green line; difference: red line.

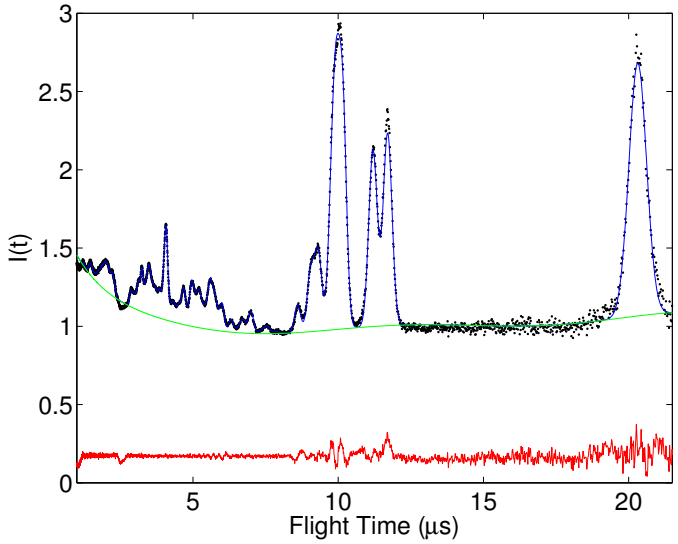

Figure A.29: GSAS fit for adamantanecarboxylic acid at 260 K, background fit with a 10 term Chebyshev polynomial ($2\theta = 26°$). Experimental data: black dots; GSAS fits: blue line; background: green line; difference: red line.

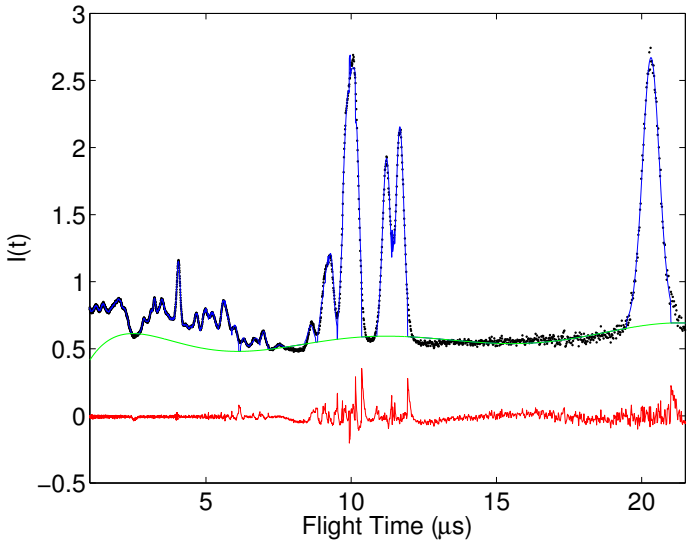

Figure A.30: GSAS fit for adamantanecarboxylic acid at 300 K, background fit with a 10 term Chebyshev polynomial ($2\theta = 26°$). Experimental data: black dots; GSAS fits: blue line; background: green line; difference: red line.

Appendix B - RMC

ZIF

Initial Configuration

phase	temperatures (K)	supercell dimensions and angles					
		a (Å)	b (Å)	c (Å)	$\alpha(^\circ)$	$\beta(^\circ)$	$\gamma(^\circ)$
ZIF-4	478	46.9020	47.4099	54.4800	90.0	90.0	90.0
ZIF-zni	298	47.2868	47.2868	49.8920	90.0	90.0	90.0
ZIF-zni	406	46.9690	46.9690	49.5124	90.0	90.0	90.0
ZIF-zni	540	47.4072	47.4072	49.7500	90.0	90.0	90.0
ZIF-zni	673	47.2018	47.2018	49.4788	90.0	90.0	90.0
aZIF	298	53.9510	53.9510	53.9510	90.0	90.0	90.0
aZIF	573	53.9510	53.9510	53.9510	90.0	90.0	90.0

Table B.1: Dimensions and Angles in the ZIF-4 and ZIF-zni and aZIF Supercells

phase	temperatures (K)	number of atoms				
		total	Zn	N	C	D
ZIF-4	478	7344	432	1728	2592	2592
ZIF-zni	298	8704	512	2048	3072	3072
ZIF-zni	406	8704	512	2048	3072	3072
ZIF-zni	540	8704	512	2048	3072	3072
ZIF-zni	673	8704	512	2048	3072	3072
aZIF	298	8704	512	2048	3072	3072
aZIF	573	8704	512	2048	3072	3072

Table B.2: Number of atoms in the ZIF-4, ZIF-zni and aZIF Supercells

Parameters

atom i	atom j	neutron coefficients, $c_i b_i c_j b_j$ ($10^{-28} m^2$)
Ed	Ed	0.04450
Ed	C	0.09896
Ed	N	0.09292
Ed	Zn	0.01410
C	C	0.05502
C	N	0.10332
C	Zn	0.01567
N	N	0.04850
N	Zn	0.01472
Zn	Zn	0.00112

Table B.3: Neutron Coefficients, c_i = the concentration of atom i, for example $c_{Zn} = \frac{1}{17}$, b_i = the neutron scattering length of atom i, for example $b_{Zn} = 0.568\ 10^{-14} m$.

atom	distance (Å)
Zn	0.015
N	0.050
C	0.050
Ed	0.100

Table B.4: Maximum Move

phase	temperature (K)	number density (atoms Å^{-3})
ZIF-4	478	0.060623
ZIF-zin	298	0.078020
ZIF-zin	406	0.079686
ZIF-zin	540	0.077846
ZIF-zin	673	0.078956
aZIF	298	0.055427
aZIF	573	0.055427

Table B.5: Number Density

PTP

Initial Configuration

temperatures (K)	supercell dimensions and angles					
	a (Å)	b (Å)	c (Å)	$\alpha(^\circ)$	$\beta(^\circ)$	$\gamma(^\circ)$
10	47.702401	55.16340	54.1768	89.6459	92.4627	90.031215
65	47.826901	55.25070	54.2136	89.6619	92.4243	90.025301
125	48.037501	55.41720	54.2756	89.7030	92.3412	90.023132
150	48.105302	55.50775	54.2996	89.7430	92.3131	90.030372
165	48.123001	55.57770	54.3160	89.7930	92.3059	90.024320
185	48.094440	50.14818	54.3524	90.0000	92.3100	90.000000
250	48.278040	50.35095	54.3840	90.0000	92.2359	90.000000
290	48.504000	50.48577	54.4444	90.0000	92.1300	90.000000

Table B.6: Dimensions and Angles in the PTP Supercell

temperatures (K)	number of atoms		
	total	C	D
10	15360	8640	6730
65	15360	8640	6730
125	15360	8640	6730
150	15360	8640	6730
165	15360	8640	6730
185	13824	7776	6048
250	13824	7776	6048
290	13824	7776	6048

Table B.7: Number of atoms in the PTP Supercell

Parameters

atom i	atom j	neutron coefficients, $\mathrm{c}_i\mathrm{b}_i\mathrm{c}_j\mathrm{b}_j$ ($10^{-28}m^2$)
C	C	0.13975
C	D	0.21821
D	D	0.08518

Table B.8: Neutron Coefficients, c_i = the concentration of atom i, for example $\mathrm{c}_C = \frac{18}{32}$, b_i = the neutron scattering length of atom i, for example $\mathrm{b}_C = 0.6646\ 10^{-14}m$.

atom	distance (Å)
C	0.050
D	0.100

Table B.9: Maximum Move

temperature (K)	number density (atoms $\mathrm{Å}^{-3}$)
10	0.107844
65	0.107317
125	0.106397
150	0.106025
165	0.105819
185	0.105540
250	0.104649
290	0.103761

Table B.10: Number Density

OTP

Initial Configuration

phase	temperatures (K)	supercell dimensions and angles					
		a (Å)	b (Å)	c (Å)	$\alpha(^\circ)$	$\beta(^\circ)$	$\gamma(^\circ)$
crystalline	16	55.6398	52.35678	46.15848	90.0	90.0	90.0
slow cool glass	16	55.2700	55.27000	55.27000	90.0	90.0	90.0
rapid cool glass	16	55.8600	55.86000	55.86000	90.0	90.0	90.0

Table B.11: Dimensions and Angles of the OTP Supercell

phase	temperatures (K)	number of atoms		
		total	C	D
crystalline	16	13824	7776	6048
slow cool glass	16	16384	9216	7168
rapid cool glass	16	16384	9216	7168

Table B.12: Number of atoms in the OTP Supercell

Parameters

atom i	atom j	neutron coefficients, $\mathrm{c}_i\mathrm{b}_i\mathrm{c}_j\mathrm{b}_j$ ($10^{-28}m^2$)
C	C	0.13975
C	D	0.21821
D	D	0.08518

Table B.13: Neutron Coefficients, c_i = the concentration of atom i, for example $\mathrm{c}_C = \frac{18}{32}$, b_i = the neutron scattering length of atom i, for example $\mathrm{b}_C = 0.6646\ 10^{-14}m$.

atom	distance (Å)
C	0.050
D	0.100

Table B.14: Maximum Move

phase	number density (atoms $\mathrm{Å}^{-3}$)
crystalline	0.102807
slow cool glass	0.097040
rapid cool glass	0.093998

Table B.15: Number Density

Adamantane

Initial Configuration

temperatures (K)	supercell dimensions and angles					
	a (Å)	b (Å)	c (Å)	$\alpha(^\circ)$	$\beta(^\circ)$	$\gamma(^\circ)$
100	52.957520	52.957520	52.984620	90.0	90.0	90.0
198	53.229120	53.229120	53.676540	90.0	90.0	90.0
218	46.850453	46.850453	46.850453	90.0	90.0	90.0
258	47.042946	47.042946	47.042946	90.0	90.0	90.0

Table B.16: Dimensions and Angles in adamantane Supercells

temperatures (K)	number of atoms		
	total	C	D
100	19968	7680	12288
198	19968	7680	12288
218	13000	5000	8000
258	13000	5000	8000

Table B.17: Number of atoms in adamantane Supercells

Parameters

atom i	atom j	neutron coefficients, $\mathrm{c}_i\mathrm{b}_i\mathrm{c}_j\mathrm{b}_j$ ($10^{-28}m^2$)
C	C	0.06534
C	D	0.20987
D	D	0.16853

Table B.18: Neutron Coefficients, c_i = the concentration of atom i, for example $\mathrm{c}_C = \frac{10}{26}$, b_i = the neutron scattering length of atom i, for example $\mathrm{b}_C = 0.6646\ 10^{-14}m$.

atom	distance (Å)
C	0.050
D	0.100

Table B.19: Maximum Move

temperature (K)	number density (atoms $\mathrm{Å}^{-3}$)
100	0.134378
198	0.131296
218	0.126416
258	0.124870

Table B.20: Number Density

Adamantanecarboxylic acid

Initial Configuration

temperatures (K)	supercell dimensions and angles					
	a (Å)	b (Å)	c (Å)	$\alpha(^\circ)$	$\beta(^\circ)$	$\gamma(^\circ)$
150	45.3789	46.9994	46.2020	80.805	87.130	74.51
240	45.6512	47.4159	46.5104	80.031	86.060	74.43
270	45.3621	48.1649	46.5356	77.510	85.942	76.28
300	45.3448	48.0753	46.5824	77.340	85.827	76.33

Table B.21: Dimensions and Angles in adamantanecarboxylic acid Supercells

temperatures (K)	number of atoms				
	total	C	D	O	H
150	11368	4312	5880	784	392
240	11368	4312	5880	784	392
270	11368	4312	5880	784	392
300	11368	4312	5880	784	392

Table B.22: Number of atoms in the low-temperature phase of adamantanecarboxylic acid Supercells

Parameters

atom i	atom j	neutron coefficients, $c_i b_i c_j b_j$ ($10^{-28} m^2$)
D	D	0.11906
D	H	-0.00890
D	C	0.17397
D	O	0.02762
H	H	0.00017
H	C	-0.00650
H	O	-0.00103
C	C	0.06355
C	O	0.02018
O	O	0.00160

Table B.23: Neutron Coefficients, c_i = the concentration of atom i, for example $c_C = \frac{11}{29}$, b_i = the neutron scattering length of atom i, for example $b_C = 0.6646\ 10^{-14} m$.

atom	distance (Å)
D	0.100
H	0.100
C	0.050
O	0.050

Table B.24: Maximum Move

temperature (K)	number density (atoms Å^{-3})
150	0.121276
240	0.119020
270	0.117907
300	0.118082

Table B.25: Number Density

Appendix C - Programs and Input Files

The electronic portion of this appendix contains codes for the analysis of the models of all the materials studied in this thesis, codes, where non standard methods were used, for the production of the initial configurations and codes, where applicable, for the writing of planarity files. Also included are the input files required to run these codes. All codes and input files provided are listed, with a brief description, below.

AV-MOVE.f90

Code that produces a set of histograms, averages and standard deviations of the atomic moves between the initial and refined configurations of a material. The input files required to run this code are the initial and refined configuration files, *.rmc6f*, of the relevant material, phase and temperature.

PLANARITY-write-[ptp,otp,ad-acid].f90

Codes that produces the planarity file for the specified material; a planarity file, *.planarity*, has a format analogous to a bonds file, *.bond* [43] with the exact format of a planarity file described in the preamble of the codes *PLANARITY-write-[ptp,otp,ad-acid].f90*. The input files required to run this code are the configuration file, *.rmc6f*, and connectivity file, *.neigh*, of the relevant material, phase and temperature.

PLANARITY-read.f90

Code that produces the histogram, average and standard deviation of the calculated deviation from planarity, ω. The input files required to run this code are the configuration file, *.rmc6f*, and planarity file, *.planarity*, of the relevant material, phase and temperature.

ZIF

Input files

The initial and refined configurations of, in the *.rmc6f* format [43], as well as the connectivity in, as described by the applied distance windows, in the *.neigh* format [43], all three phases of ZIF-4.

ZIF.f90

Code that produces a set of histograms, averages and standard deviations of the Zn–N bond length and the tetrahedral, inter-tetrahedral, planarity and wag angles as well as a scatter graph of planarity versus wag angle in all three phases of ZIF-4. The input files required to run this code are the configuration file, *.rmc6f*, and connectivity file, *.neigh*, of the relevant phase and temperature.

PTP

Input files

The initial and refined configurations of, in the *.rmc6f* format [43], the connectivity in, as described by the applied distance windows, in the *.neigh* format [43], as well as the planarity files of, in the *.planarity* format, all temperatures of PTP.

PTP.f90

Code that produces a set of histograms, averages and standard deviations of the C–C and C–D bond lengths as well as the $\widehat{\mathrm{CCC}}$, $\widehat{\mathrm{CCD}}$ and torsion angles in PTP. This code also gives a plot of all the carbons in the crystal with the two end rings of each PTP molecule highlighted red or blue depending on whether they have a positive or negative torsion angle, given in the *.c3d2* format, as well as the histograms, averages and standard deviations of the deviation from planarity, ω, of individual phenyl rings, grouped by ring type, i.e. middle or end rings of a PTP molecule. The input files required to run this code are the configuration file, *.rmc6f*, and connectivity file, *.neigh*, of the relevant phase and temperature.

PTP-scfgg.f90

Code that produces a randomly twisted initial configuration for the high-temperature phase of PTP where the middle phenyl ring of each PTP molecule has been randomly rotated by approximately 20° in either a positive or negative sense with respect to the molecular plane. The input files required to run this code are the configuration file, *.rmc6f*, and connectivity file, *.neigh*, of the relevant high-temperature phase.

OTP

Input files

The initial and refined configurations of, in the *.rmc6f* format [43], the connectivity in, as described by the applied distance windows, in the *.neigh* format [43], as well as the planarity files of, in the *.planarity* format, the crystalline and glass phases of OTP.

OTP.f90

Code that produces a set of histograms, averages and standard deviations of the C–C and C–D bond lengths as well as the $\widehat{\mathrm{CCC}}$, $\widehat{\mathrm{CCD}}$ and torsion angles in OTP. This code also calculates the orientation vectors of all OTP molecules, collapsed onto a single origin to produce a real space stereographic projection, given in the *.c3d2* format, as well as the histograms, averages and standard deviations of the deviation from planarity, ω, of individual phenyl rings, grouped by ring type, i.e. middle or end rings of a OTP molecule. The input files required to run this code are the configuration file, *.rmc6f*, and connectivity file, *.neigh*, of the relevant phase and temperature.

OTP-mol-vec-change.f90

Code that produces the histograms, averages and standard deviations of the angles between the orientation vectors of the corresponding OTP molecules in different configurations or phases, i.e. MD and RMC configurations or slow and rapid cool glass configurations. The input files required to run this code are the Chem3D Cartesian files of the collapsed orientation vectors, given as an output of *OTP.f90*, modified

as described in the preamble of *OTP-mol-vec-change.f90*, for the two configurations or phases to be compared.

OTP-molpdf.f90

Code that calculates the molecular distribution function of the three phases of OTP. The input files required to run this code are the configuration file, *.rmc6f*, and connectivity file, *.neigh*, of the relevant phase and temperature.

Adamantane

Input files

The initial and refined configurations of, in the *.rmc6f* format [43], as well as the connectivity in, as described by the applied distance windows, in the *.neigh* format [43], all temperatures of adamantane.

Also provided are the high-temperature lattice arrays, in the *.rmc6f* format [43], and the configuration of a single adamantane molecule, in the *.rmc6f* format [43].

AD.f90

Code that produces a set of histograms, averages and standard deviations of the C–C and C–D bond lengths as well as the $\widehat{\mathrm{CCC}}$, $\widehat{\mathrm{CCD}}$ and tetrahedral angles in adamantane. This code also calculates the four orientation vectors of all adamantane molecules, collapsed onto a single origin and in the crystal structure, given in the *.c3d2* format, as well as producing the histogram, average and standard deviation of the angle between the calculated orientation vector and that of the structure described in C. E. Nordman *et al.* [95]. These orientation vectors are highlighted, according to which molecular orientation they correspond to, as described in the preamble of *AD.f90*. The input files required to run this code are the configuration file, *.rmc6f*, and connectivity file, *.neigh*, of the relevant phase and temperature.

AD-scfgg.f90

Code that produces an initial configuration for the high-temperature disordered phase of adamantane. The input files required to run this code are the relevant

high-temperature lattice array file, *.rmc6f*, and the single adamantane molecule configuration file, *.rmc6f*.

Adamantanecarboxylic acid

Input files

The initial and refined configurations of, in the *.rmc6f* format [43], the connectivity in, as described by the applied distance windows, in the *.neigh* format [43], as well as the planarity files of, in the *.planarity* format, all temperatures of adamantanecarboxylic acid.

Also provided are the high-temperature lattice arrays, in the *.rmc6f* format [43], and the configuration of a single adamantanecarboxylic acid dimmer, in the Chem3D Cartesian format with added atomic numbers, *.c3d2n*.

AD-ACID.f90

Code that produces a set of histograms, averages and standard deviations of the C–C, C–D, C–O, C=O and O–H bond lengths as well as the $\widehat{\mathrm{CCC}}$, $\widehat{\mathrm{CCD}}$, $\widehat{\mathrm{OCO}}$ and tetrahedral angles in adamantanecarboxylic acid. This code also calculates the four orientation vectors of all adamantane molecules, collapsed onto a single origin and in the crystal structure, given in the *.c3d2* format. These orientation vectors are highlighted, according to whether they correspond to a vector in or out of the molecular plane, as described in the preamble of *AD-ACID.f90*. The input files required to run this code are the configuration file, *.rmc6f*, and connectivity file, *.neigh*, of the relevant phase and temperature.

AD-ACID-scfgg.f90

Code that produces an initial configuration for the high-temperature disordered phase of adamantanecarboxylic acid. The input files required to run this code are the relevant high-temperature lattice array file, *.rmc6f*, and the adamantanecarboxylic acid dimer configuration file, in the Chem3D Cartesian format with added atomic numbers, *.c3d2n*.